

MODEL-BASED RECONSTRUCTION OF MYOCARDIAL
PERFUSION SPECT AND PET IMAGES

by
Yinfeng Dong

A dissertation submitted to Johns Hopkins University in conformity
with the requirements for the degree of Doctor of Philosophy

Baltimore, Maryland

October, 2016

ABSTRACT

Myocardial perfusion imaging is an important noninvasive tool in the diagnosis and prognosis of coronary artery disease, the leading cause of death in the United States. Electrocardiographically (ECG) gated acquisition allows combined evaluation of perfusion and left ventricular function within a single study. However, the accuracy of perfusion quantification and functional analysis is reduced by a number of image degrading factors. Particularly, partial volume effects (PVE) resulting from finite spatial resolution cause activity spillover between tissue classes and blur region boundaries. High-resolution anatomical images, such as contrast CT or MRI, can be used for partial volume compensation (PVC), but they are generally not available in clinical practice.

The objective of this research is to develop and evaluate a model-based reconstruction method for emission computed tomography applied to myocardial perfusion imaging to improve perfusion quantification and functional assessment without the presence of anatomical images.

The idea is to model the left ventricle (LV) using a geometry model and an activity distribution model instead of modeling them using voxels. The geometry model parameterizes the endocardial and epicardial surfaces using a set of rays originating from the long axis of LV. The rays sample the surfaces cylindrically in the basal and mid-ventricular regions and spherically in the apex. The surfaces are obtained by interpolating the corresponding intersection points with the rays using a cubic-spline function. The activity distribution model divides the myocardium into segments similar to those used in standardized myocardial quantitative analysis. The model assumes uniform activity concentrations in the segments as well as the blood pool and body background. The method estimates the parameters of the geometry and activity models instead of the intensities of all voxels, which greatly reduces the number of unknowns to be estimated.

The goal of model-based reconstruction method was to estimate the parameters that give the best match between the image generated by the model and the measured data. The input image is contaminated by noise, so the metric for the goodness of fit was a statistical criterion based on

the likelihood, i.e., the probability that the image resulted from the given set of model parameters. The image generated by the model includes the effects of resolution and other image degrading factors. A shape constraint was also incorporated into the objective function to regularize the ill-posed reconstruction problem and increase the robustness to perfusion defects and noise. The model parameters were optimized by seeking the maximum of the objective function using a group-wise alternating scheme along with dedicated initial parameter estimation. The hypothesis underlying the work is that resulting geometry parameters produce an accurate segmentation of the LV while the activity parameters are PVE compensated representations of the true activities in the segments.

The proposed method integrates prior knowledge about the targeted object and the imaging system into one framework and allows simultaneous LV segmentation and PVC. In the evaluation with simulated myocardial perfusion SPECT images, it improved accuracy and precision in delineating the myocardium in comparison with typical segmentation methods. In addition, it recovered the myocardial activity more effectively compared to deconvolution-based PVC, which also does not require coregistered anatomical images to define regions of interest.

Advisor: Eric C. Frey, Ph.D.

Reader: Yong Du, Ph.D.

ACKNOWLEDGEMENTS

I would like to express the deepest gratitude to my advisor Dr. Eric C. Frey for his support and encouragement throughout my graduate study. He is not only an excellent researcher, but also a great teacher. Without his incredible patience and expert guidance, the completion of this study could not have been possible.

I am also grateful to Dr. Yong Du. He is always available when I have questions. He inspired me to select the research topic and helped me gain insights into the problems. I enjoyed the time of doing experiments and discussing questions together.

I would like to thank the rest of my committee members, Dr. Trac D. Tran and Dr. Gerard G.L. Meyer, for their insightful comments and dedicated efforts on my dissertation.

I would like to thank Dr. Jingyan Xu. She patiently guided me in my first research project in graduate school. I was impressed by her expertise and devotion to research. She taught me to investigate the unexpected outcome instead of being disappointed in the research.

I also want to thank Dr. Katsuyuki Taguchi for his sincere and valuable suggestions on improving my presentation skills. I really appreciate his efforts in improving the DMIP seminars.

I would like to thank the director of DMIP, Dr. Benjamin M.W. Tsui, for creating an excellent research environment for students. He taught me how to present complex ideas in plain languages.

I would like to thank the administrative coordinator of DMIP, Michele Ingram, for her help. I am also deeply touched by her dedication to work and consideration for others.

I thank my fellow colleagues, Martin Stumpf, Dr. George Fung, Dr. Abhinav Kumar Jha, Dr. Taek-Soo Lee, Dr. Michael Ghaly, Dr. Okkyun Lee, Dr. Andrew Rittenbach, Dr. Esther Vicente, Dr. Tao Feng, Dr. Jizhe Wang, Dr. Fatma ElShahaby, Xin Li, Jianting Yue, Ye Li, and Nate Crookston for their suggestions, help and friendship.

Thanks also go to my friends at JHU. They made the five years I spent in Baltimore more interesting and memorable.

Special thanks go to my wonderful girlfriend Hongying An. Her encouragement and understanding helped me through the most frustrating and overwhelming time in the completion of the dissertation. I am very fortunate to have met her before graduation.

Finally and most importantly, I would like to thank my parents and families in China for their unconditional love and support for my pursuit of Ph.D. in the United States.

TABLE OF CONTENTS

ABSTRACT.....	ii
ACKNOWLEDGEMENTS.....	iv
TABLE OF CONTENTS.....	vi
LIST OF TABLES.....	xi
LIST OF FIGURES.....	xii
LIST OF ACRONYMS.....	xix
1. Introduction.....	1
1.1 Motivation.....	1
1.2 Organization.....	3
2. Background.....	5
2.1 Myocardial Perfusion Imaging.....	5
2.1.1 Basics of SPECT and PET.....	5
2.1.2 Image Degrading Factors.....	7
2.1.3 Stress and Rest Myocardial Perfusion Imaging.....	9
2.1.4 Gated Myocardial Perfusion Imaging.....	10
2.1.5 Dynamic Myocardial Perfusion Imaging.....	11
2.2 Image Reconstruction.....	12
2.2.1 Analytical Image Reconstruction.....	12
2.2.2 Iterative Image Reconstruction.....	13

2.2.3	Regularization and Maximum A Posterior (MAP) Reconstruction	15
2.3	Image Analysis.....	16
2.3.1	Myocardial Perfusion.....	16
2.3.2	Left Ventricular Function.....	19
2.4	Partial Volume Effects	20
2.5	Partial Volume Compensation	21
2.6	Left Ventricle Segmentation	23
3.	Materials and Methods.....	27
3.1	Geometry Model	27
3.2	Activity Distribution Model.....	28
3.3	Imaging System Model	29
3.4	Objective Function.....	31
3.4.1	Data-Fitting in the Projection Domain.....	31
3.4.2	Data-Fitting in the Image Domain: FBP	32
3.4.3	Data-Fitting in the Image Domain: OS-EM.....	33
3.4.4	Regularization	34
3.5	Optimization	36
3.5.1	Global Optimization: MultiStart	36
3.5.2	Efficient Optimization: Group-wise Alternating Scheme.....	37
3.5.3	Initial Parameter Estimation.....	39

3.6	Evaluation	43
3.6.1	2D Simulation	43
3.6.2	3D Simulation	46
3.6.3	Errors of Parameter Estimation.....	49
3.6.4	Efficacy of Left Ventricle Segmentation	50
3.6.5	Efficacy of Mid-Myocardial Surface Estimation	51
3.6.6	Efficacy of Partial Volume Compensation	52
4.	Results and Discussion (2D): Global Optimization	54
4.1	Geometry Model	54
4.2	Activity Distribution Model.....	55
4.3	Resolution Model.....	57
4.4	Noise Model.....	60
4.4.1	FBP reconstruction.....	60
4.4.2	OS-EM Reconstruction	63
4.5	The Thickness Prior	69
4.6	Parameter Estimation	71
4.7	Simplified 1D Model	77
4.8	Discussion	82
5.	Results and Discussion (2D): Efficient Optimization.....	86
5.1	Group-wise Alternating Optimization	86

5.2	Parameter Estimation	92
5.3	Left Ventricle Segmentation	95
5.4	Estimation of the Mid-Myocardial Surface	96
5.5	Efficacy of Partial Volume Compensation	103
5.6	Discussion	106
6.	Results and Discussion (3D).....	108
6.1	Geometry Model Evaluation.....	108
6.2	Slice-by-Slice Fitting	110
6.3	Fully 3D Fitting.....	112
6.4	Myocardial Perfusion Images	115
6.5	Efficacy of LV Segmentation	117
6.6	Efficacy of PVC.....	119
6.7	Discussion	122
7.	Summary and Future Work.....	124
7.1	Summary	124
7.2	Future Work.....	128
7.2.1	Evaluation with More Data.....	128
7.2.2	Implementation in the Projection Domain	129
7.2.3	Regularization Term	131
7.2.4	Process Automation	131

BIBLIOGRAPHY	134
CURRICULUM VITAE	139

LIST OF TABLES

Table 4-1. The average values of endocardial radius, wall thickness, and myocardial activity parameters over radii or segments in Figure 4-4, along with the percentage errors with respect to the phantom fitting reference.	60
Table 4-2. Mean square errors (MSE) of fitting the histograms using lognormal and normal distributions in Figure 4-8.....	65
Table 5-1. Combinations of sampling ranges of endocardial radius, wall thickness, and activity concentrations in the myocardium, blood pool, and background.	87
Table 5-2. RMSEs of estimated endocardial radius, wall thickness and myocardial activity parameters using the MultiStart method and the proposed alternating scheme for the standard and high noise data shown in Figure 5-4.	93
Table 5-3. The averaged root mean square error (μ RMSE) of estimated mid-myocardial radius parameters with reference to the phantom fitting truth.	103

LIST OF FIGURES

Figure 2-1. (a) a transaxial slice; (b) a short-axis slice; (c) a horizontal long-axis slice; (d) a vertical long-axis slice; (e) the polar map.....	17
Figure 3-1. Illustration of the LV geometry model and the activity distribution model. (a) Long-axis view; (b) Short-axis view; (c) An example short-axis model image generated with 8 rays around the axis in the geometry model and 6 myocardial segments in the activity distribution model.	28
Figure 3-2. The iterative fitting process of the model-based reconstruction in the image domain.	39
Figure 3-3. Illustration of generating a 2D initial estimate from a short-axis slice for a predefined initial wall thickness.	40
Figure 3-4. Illustration of generating a 3D initial estimate for a predefined initial wall thickness.	42
Figure 3-5. Illustration of combining slice-by-slice fitting results into initial optimization parameters for fully 3D fitting.	42
Figure 3-6. The procedure of the group-wise alternating optimization scheme.	43
Figure 3-7. Myocardial perfusion SPECT simulation of short-axis slices: (a) the phantom image; (b) noise-free data; (c) standard noise data; (d) high noise data, containing 10% counts of the standard data. Each dataset consists of three images: from left to right, the sinogram and the FBP and OS-EM reconstructions. The negative values were set to zero in the display.	45
Figure 3-8. Circumferential profiles of simulated short-axis images: (a) FBP reconstruction; (b) OS-EM reconstruction.	46
Figure 3-9. Myocardial perfusion SPECT simulation of a 3D transaxial phantom. From top to bottom: the phantom, noise-free data, noisy data. From left to right: a transaxial slice, a short-axis	

slice, a vertical long-axis slice, a horizontal long-axis slice. The negative values were set to zero in the display.....	47
Figure 3-10. Main diagonal profiles of the polar maps corresponding to the phantom, noise-free and two noisy images.....	49
Figure 4-1. Fitting the geometry model to XCAT short-axis myocardium masks with different numbers of radii.....	55
Figure 4-2. Fitting the activity distribution model to the short-axis phantom image using different numbers of myocardial segments. (a) The phantom image; (b)-(d) Optimized model images using 6, 8 and 12 myocardial segments; (e) Resampled myocardial circumferential profiles.....	57
Figure 4-3. Approximated resolution modeling in FBP and OS-EM reconstruction using spatially invariant Gaussian kernels. (a) FBP; (b) OS-EM; (1) Noise-free reconstruction; (2) Gaussian-blurred phantom image; (3) The difference image of (1) and (2); (4) Central horizontal profiles; (5) Central vertical profiles.....	59
Figure 4-4. Estimated (1) endocardial radius, (2) wall thickness, and (3) myocardial segmental activities from (a) FBP and (b) OS-EM noise-free reconstruction with different resolution models.....	60
Figure 4-5. Evaluation of the variance images of FBP reconstruction. (a) Noise-free FBP reconstruction; (b) Theoretically calculated variance image; (c) Numerically calculated variance image based on 10000 noise realizations; (d) Central horizontal profiles; (d) Central vertical profiles.....	61
Figure 4-6. The correlation coefficient matrix of the central column of the FBP reconstructed image: (a) the image, (b) the mesh plot, (c) the antidiagonal profile, and (d) the diagonal profiles.....	62
Figure 4-7. Comparison of estimated (a) endocardial radius, (b) wall thickness, and (c) myocardial segmental activity from the FBP noise-free reconstruction and 50 noise realizations using the approximated noise modeling.....	63

Figure 4-8 Fitting pixel intensity histograms based on 1000 OS-EM noise realizations using lognormal and normal distributions. The pixel is located in (a) the myocardium, (b) defect, (c) blood pool and (d) background, respectively..... 64

Figure 4-9. The correlation coefficient matrix of the central column of the OS-EM reconstructed image: (a) the image, (b) the mesh plot, (c) the antidiagonal profile, and (d) the diagonal profiles. 66

Figure 4-10. The pixel variance versus mean in based on 1000 OS-EM reconstructions at the two noise levels..... 67

Figure 4-11. Comparison of LS and WLS fitting with OS-EM reconstructed images. The references are from LS fitting of the noise-free reconstruction. Left: the variance was assumed to be proportional to the square of the mean. Right: the variance was assumed to be proportional to the mean. The error bars represent the standard deviation over 50 noise realizations..... 68

Figure 4-12. Illustration the relationship between the prior strength and the stability of the solution..... 69

Figure 4-13. Illustration of the effect of the shape prior and its ability to stabilize the solution. .. 70

Figure 4-14. The mean value of the data-fitting term versus the mean value of the shape prior over 50 noise realizations using FBP for different values of the regularization parameter: (a) the standard noise data; (b) the high noise data. 71

Figure 4-15. Estimated (a) endocardial radius, (b) wall thickness and (c) myocardial segmental activity parameters from FBP reconstructed images. The error bar represents the standard deviations over 50 noise realizations. The left and right columns correspond to the standard and high noise data, respectively. 72

Figure 4-16. Comparison of the mean FBP reconstructed image and the mean model images. The top and bottom rows correspond to the low and high noise levels, respectively. 73

Figure 4-17. Scatter plots of the estimated myocardial activity versus the wall thickness of the abnormal segment (#5) and the opposing normal segment (#1) based on 50 noise realizations. The left and right columns correspond to the standard and high noise levels.....	74
Figure 4-18. The mean of estimated myocardial segmental activity parameters versus the mean of wall thickness parameters. The data points based on 50 noise realizations were fitted with a linear function.	76
Figure 4-19. Box plots summarizing the distributions of estimated blood pool activity concentration and the cavity volume.	77
Figure 4-20. A simplified 1D model to simulate the proposed method.....	78
Figure 4-21. Plots of normalized error in the estimated signal width using the 1D model fitting method as a function of signal width. For comparisons, results of a conventional gradient-based method are shown. The (a) mean and (b) standard deviations of the percentage estimation error are plotted against the object width over 1000 noise realizations.....	79
Figure 4-22. A simplified 1D model to illustrate the overestimation of signal size with gradient-based methods when it is comparable to or smaller than the system FWHM.	80
Figure 4-23. The incorporation of a new shape prior that encourages an elliptical distribution of endocardial contour in the short-axis slice.....	85
Figure 5-1. Results from the three proposed optimization schemes, 3Groups-Order123, 3Groups-Order132, and 2Groups-Order12. For each of the optimization ranges described in Table 5-1 the graphs show (a) the resulting values of the objective function and RMSEs of the estimated (b) myocardial segmental activity, (c) endocardial radius, and (d) wall thickness parameters.	89
Figure 5-2. The smallest value of the objective function obtained using the proposed alternating optimization scheme versus the initial wall thickness.	91
Figure 5-3. The mean wall thickness obtained with the proposed alternating scheme versus the initial values.....	92

Figure 5-4. Comparison of values of the estimated (a) endocardial radius, (b) wall thickness and (c) myocardial activity parameters using the MultiStart method and the proposed group-wise alternating optimization scheme. The left and right columns correspond to the standard and high noise data. The error bars represent the standard deviations over 50 noise realizations of the FBP reconstructed short-axis images.	94
Figure 5-5. Evaluation of the estimated geometry model parameters in terms of LV segmentation accuracy. The top row compares the DSCs of 50 noise realizations using different methods. The bottom row shows the segmented myocardium masks of the maximum DSCs, as pointed by the arrows. The left and right columns correspond to the standard and high noise data with FBP reconstruction.	96
Figure 5-6. The means and standard deviations of the estimated endocardial radius, wall thickness and mid-myocardial radius parameters plotted versus the radial position along around the myocardium. These were calculated from 50 FBP reconstructed noise realizations at the standard noise level. The left and right columns correspond to the MultiStart and alternating methods, respectively.	97
Figure 5-7. Means (top row) and standard deviations (bottom row) of the mid-myocardial radius estimates as a function of the radial position. The estimates were obtained using the proposed alternating optimization scheme with different initial thicknesses. The left and right columns correspond to the standard and high noise data, respectively.	99
Figure 5-8. Estimation of the mid-myocardial radius based on 50 FBP reconstructed noise realizations at the standard noise and high noise levels.	101
Figure 5-9. Estimation of the mid-myocardial radius based on 50 OS-EM reconstructed noise realizations at the standard and high noise levels.	102
Figure 5-10. Graphs and images comparing the efficacy of PVC using the proposed method and deconvolution-based and ROI-based PVC methods. The results were based on FBP reconstruction of the (a) standard and (b) high noise data. In each of these two sub-figures, the top	

row shows the segmental mean activities of PVE-compensated images using the true segmented ROIs, where the error bars represent the standard deviations over 50 noise realizations; the bottom row shows the images from the 50th noise realization using different methods, as indicated by the same color of the error bars and the square enclosing the image..... 105

Figure 6-1. Short axis myocardial mask images obtained from fitting the geometry model to the phantom. The top and bottom rows are the phantom truth and the fitting results, respectively. . 109

Figure 6-2. Horizontal long axis myocardial mask images obtained from fitting the geometry model to the phantom. The top and bottom rows are the phantom truth and the fitting results, respectively. 109

Figure 6-3. Standard deviations of the fitted Gaussian resolution kernels based on short-axis slices and the entire image volume. The smallest slice index corresponds to the first apex slice. 111

Figure 6-4. (a) The computation time for one convolution, (b) the MSE with the noise-free reconstruction, and (c) the FWHM of the fitted Gaussian function as a function of the Gaussian kernel size. 113

Figure 6-5. Initial Thickness refers to the thickness of the myocardial wall used to generate a 3D initial estimate in all cases. The subfigures are (a) the value of the objective function after the group-wise alternating optimization that was initialized with parameters estimated from slice-by-slice fitting using the indicated wall thickness, (b) the DSC of myocardium segmentation, and (c) the mean of optimized wall thickness parameters as a function of the initial thickness. 114

Figure 6-6. Example slices from short-axis, vertical long-axis and horizontal long-axis views using different methods..... 116

Figure 6-7. Comparison the DSCs of the segmented myocardium for various segmentation methods as a function of the short-axis slice number (top) and horizontal long-axis slice number (bottom). 118

Figure 6-8. Comparison of the resulting model image to the phantom and FBP reconstruction of an apical slice..... 119

Figure 6-9 . Qualitative and quantitative comparison of the polar maps obtained using different methods: (a) Phantom; (b) Phantom fitting; (c) FBP reconstruction; (d) Deconvolution-based PVC; (e) Slice-by-slice fitting; (f) Fully 3D fitting; (g). The segmental activity concentrations are the means over these segmental ROIs in the polar maps for the methods in (c), (d) and (e)..... 121

LIST OF ACRONYMS

AUC	area under the curve
CAD	coronary artery disease
COM	center of mass
CT	computed tomography
FBP	filtered back projection
FWHM	full width half maximum
ICA	invasive coronary angiography
LOR	line of response
LS	least squares
LV	left ventricle
MAP	maximum <i>a</i> posterior
MBF	myocardial blood flow
ML	maximum likelihood
MPI	myocardial perfusion imaging
MRI	magnetic resonance imaging
OS-EM	ordered subset-expectation maximization
PET	positron emission tomography
PVE	partial volume effects
PVC	partial volume compensation
RMSE	root of mean square error
ROC	receiver operating characteristic
ROI	region of interest
SPECT	single photon emission computed tomography
VOI	volume of interest
WLS	weighted least squares

1. Introduction

1.1 Motivation

Coronary artery disease (CAD) is the most common type of heart disease. It is the leading cause of death for both men and women in the United States. Noninvasive myocardial perfusion imaging, especially single photon emission computed tomography (SPECT), plays a primary role in diagnosis and patient management. Electrocardiographically (ECG) gated acquisition allows a combined evaluation of perfusion and left ventricular function in a single study, the cost-effectiveness of which contributes to the fact that gating is now included in almost all myocardial perfusion SPECT studies (Abidov, Germano et al. 2013). Myocardial perfusion SPECT is recommended for patients with known or suspected CAD prior to invasive coronary angiography (ICA) and revascularization treatment (Montalescot, Sechtem et al. 2013). However, more than half of all patients referred to elective ICA had only insignificant CAD (Patel, Peterson et al. 2010). This unnecessarily wastes valuable medical resources and increases the discomfort of patients.

The diagnostic accuracy of cardiac SPECT is degraded by a number of factors. Due to poor spatial resolution, partial volume effects (PVEs) result in the spillover of estimated activity between adjacent tissues in the perfusion image and thus undermines absolute uptake quantification and confound defect detection. Additionally, PVEs blur the boundaries between anatomical regions and, consequently, reduce the reliability of left ventricle (LV) segmentation and functional assessment. Contrast-enhanced CT or MRI images can be segmented to evaluate cardiac functions. If they are registered to the perfusion image, the resulting regions of interest (ROIs) can provide useful high-resolution boundary information for accurate partial volume compensation (PVC). However, these high-resolution contrast-enhanced anatomical images are generally not available in clinical practice, due to concerns over radiation dose or cost.

To address this issue, the main objective of this research was to develop and evaluate a model-based reconstruction method for nuclear myocardial perfusion images to improve perfusion

quantification and functional analysis without the use of high-resolution contrast-enhanced anatomical images.

The method is comprised of two models. An object model is used to describe the LV geometry and activity distribution in the cardiac image. The geometry modeling is based on the LV shape, which is similar to the shape of a bullet (Cauvin, Boire et al. 1993) or an ellipsoid (Germano, Kiat et al. 1995). The activity distribution modeling is based on standardized segmental analysis (Cerqueira, Weissman et al. 2002), which divides the myocardium into anatomically meaningful regions. It estimates these model parameters instead of voxel values and thus greatly reduces the number of unknowns to be derived. A geometric constraint incorporating additional prior structural information is also introduced to further regularize the ill-posed reconstruction problem and increase robustness to perfusion defects and noise. The second constituent of the method is the model of the image formation process, which models noise and resolution properties of the image resulting from the imaging and reconstruction processes. Using the maximum likelihood (ML) criterion, the model is fitted to the observed data, taking into account the noise statistics, to obtain estimates of the model parameters. The estimated geometry parameters can be used to generate segmented LV regions-of-interest (ROIs) maps and segmental activity estimates that are PVE compensated.

The proposed method integrates prior knowledge about the targeted object and the imaging system into one estimation framework and allows simultaneous LV segmentation and PVC. In comparison with conventional segmentation methods, using additional shape, resolution and noise information is expected to improve accuracy of the delineation of myocardial surfaces. This could provide improved estimates of LV function. In addition, the extra object information might be beneficial to improving deconvolution-based PVC that also does not require ROIs defined from anatomical images.

1.2 Organization

This dissertation is organized into chapters providing an introduction, a description of methods, results and discussion.

Chapter 2 introduces the fundamentals of myocardial perfusion imaging and the related analysis of perfusion and cardiac function with a specific focus on LV segmentation and PVC.

Chapter 3 comprehensively describes the development of the model-based reconstruction method, including the object and the image formation model, the objective function, optimization methods, and evaluation methods.

Chapter 4 focuses on characterizing different aspects of the proposed method and demonstrating its efficacy. For simplicity, this evaluation was performed on short-axis images based on analytically simulated myocardial perfusion SPECT. To make the simulation realistic, the LV geometry was extracted from the XCAT digital human phantom. A perfusion defect was also inserted. The objective function was globally optimized without concern for the computational expense. In addition, a simplified one-dimensional experiment was conducted to reveal some important properties of the model-fitting method.

Chapter 5 evaluates the proposed method based on the two-dimensional simulation described in the previous chapter, but using a more efficient alternating optimization scheme. The scheme was characterized by quantifying its performance on perturbed initial points. The results were interpreted based on various potential applications, including mid-myocardium surface estimation, LV segmentation, and the efficacy of PVC, by comparing to existing methods.

Chapter 6 evaluates the proposed method in the context of a three-dimensional myocardial perfusion SPECT simulation. The reoriented tomographic image was fitted in two-dimension on the basis of multiple short-axis slices using the method described in the previous chapter. The resulting model parameters were used to initialize the fully three-dimensional fitting.

Chapter 7 summarizes the innovations and findings during the development and evaluation of the proposed model-based reconstruction method and discusses important topics that need to be investigated in the future.

2. Background

2.1 Myocardial Perfusion Imaging

Coronary artery disease (CAD) is caused by the accumulation of plaques on the inner walls of the arteries, which run around the outside of the heart and have small branches supplying oxygen-rich blood to the heart muscle (myocardium). The buildup of plaques can narrow and harden the arteries, leading to reduced blood flow.

Radionuclide myocardial perfusion imaging (MPI) has a long history as the primary noninvasive tool for diagnosis and risk stratification of patients with known or suspected CAD. Instead of directly examining the arteries, MP assesses how well blood flows through the heart muscle, i.e., the myocardial perfusion.

2.1.1 Basics of SPECT and PET

Radionuclide MPI is performed using two fundamental tomographic imaging modalities in nuclear medicine: single photon emission computed tomography (SPECT) and positron emission tomography (PET).

In myocardial perfusion SPECT and PET, radiotracers, i.e., radionuclide-labeled pharmaceuticals, are injected intravenously and extracted from the blood to bind with the myocardium. To accurately reflect regional myocardial perfusion, radiotracers should have high myocardial extraction, rapid clearance from the blood, and sufficiently long retention to allow imaging. A number of perfusion radiotracers are available in clinical practice that have these properties to varying degrees. SPECT uses gamma ray emitting tracers such as thallium-201 (^{201}Tl) chloride, technetium-99m ($^{99\text{m}}\text{Tc}$) sestamibi and tetrofosmin, while PET uses positron emitting tracers such as rubidium-82 (^{82}Rb), oxygen-15-water (^{15}O -water), and nitrogen-13-ammonia (^{13}N -ammonia), with fluoride-18 (^{18}F) labeled tracers undergoing clinical trials and awaiting regulatory approval..

SPECT depends on the detection of gamma photons emitted from radioactive decay to determine radionuclide distribution within the patient. The gamma camera is widely used in clinical nuclear medicine applications to record incident gamma photons. A collimator, which is typically made of high-density absorptive materials such as lead or tungsten and consists of an array of holes, is placed in front of the camera to allow photons traveling in certain directions to interact with a large-area scintillation crystal behind it. The crystal converts the photons that pass through the collimator into visible light or scintillation photons. An array of photomultiplier tubes is coupled to the back of the crystal and produces a pulse of electrical charge proportional to the amount of input light. Electronic circuits are used to estimate the location and energy deposition of each gamma photon interaction. SPECT systems typically consist of two gamma cameras that can be oriented with the crystals either near-perpendicular or parallel to each other. The two cameras provide the ability to acquire two projection images of the patient at the same time, allowing for a reduction of acquisition duration by a factor of two. Typically, the detectors are rotated around the body to acquire projection data at multiple views, a requirement for tomographic reconstruction. In gamma camera imaging, including SPECT, the collimator determines the trade-off between the fraction of emitted photons that are detected and spatial resolution. Typically a collimator used in MPI accepts on the order of 2×10^4 photons. The resolution is distance-dependent and is on the order of 8-10 mm at 10 cm from the face of the collimator.

On the other hand, PET involves the coincidence detection of a pair of simultaneously-emitted 511keV gamma-ray photons generated by the annihilation of positrons emitted in positron decay. Gamma cameras can also be used to detect these high-energy photons, but the high energies pose a number of challenges. In PET the detectors are usually arranged in stationary 360° rings around the patient. Two photons detected within a small interval of time with respect to each other, known as the coincidence window, are assumed to originate from the same annihilation event. Thus, the decay is assumed to have occurred along a line connecting the two detection positions known as a line-of-response (LOR). Since PET does not necessitate collimators to provide

directional information, a significantly larger fraction (sensitivity) of emitted photons can be detected than in SPECT by approximately two to three orders (Rahmim and Zaidi 2008). The resolution in PET is limited by the size of the crystals, the geometry of the PET scanner, and factors intrinsic to the decay such as the distance the positron travels between the time it is emitted until it annihilates (known as the positron range), and the fact that the angle of the two positron photons varies slightly from the ideal angle of 180° (known as positron noncollinearity).

2.1.2 Image Degrading Factors

Some physical factors have an impact on the image formation process and, consequently, degrade the reconstructed activity distribution.

Noise is inherent in SPECT and PET imaging due to the statistical nature of radioactive decay, which is well modeled by a Poisson distribution. It corrupts the projection data and adds randomness in the estimated activity concentration. The effect of noise is irreversible, but can be controlled, typically by sacrificing some other image property such as spatial resolution. Increased photon counts can reduce the statistical noise. Thus higher administered activity, longer acquisition time, reduced attenuation of photons inside the patient's body, and higher system sensitivity (the number of detected counts per unit of radioactivity) all result in projection data with a greater number of counts, and thus lower image noise. Thanks to its higher sensitivity and resolution, PET normally has improved signal-to-noise ratio than SPECT.

Another image degrading factor is photon attenuation in the patient body. Some emitted photons interact with tissues and are absorbed or scattered by tissues before escaping the body, a phenomenon known as photon attenuation. Attenuation reduces the number of detected primary (unscattered) photons, resulting in a depth-dependent underestimation of activity. The severity of attenuation depends on the photon energy, the tissue composition, and the path length. Higher energy, smaller density, and shorter path are likely to diminish the effect. Attenuation correction is a necessity for reliable quantification of the activity distribution. It generally requires prior

knowledge of the distribution of attenuation coefficients inside the body, known as the attenuation map. The attenuation map can be derived from coregistered CT images. In SPECT, the path length is dependent on the location of the single photon emission event, and is thus different for every position and projection view. In PET, the path length involves two opposite photons and equals the length of the corresponding LOR, leading to the independence of attenuation on the positron origin along the LOR. Therefore, attenuation correction is more straightforward in PET.

For photon energies of the radionuclides used in MPI (68-80keV for ^{201}Tl , 140keV for $^{99\text{m}}\text{Tc}$, and 511keV for positron emitters), attenuation includes both the photoelectric effect and scattering. The former results in complete absorption of the incident photon, while the latter results in a change of direction (and, for incoherent scatter, energy) of the photon. In both PET and SPECT the measured energy of the detected photons is used to discriminate between scattered and unscattered photons. However, because the energy resolving capability of the detectors is limited, a fraction of the scattered photons will be detected and mistaken for primary photons. The assumed LOR is thus likely to provide misleading location information about the emission origin and consequently distorting the estimated activity distribution. Scatter correction is an important in quantitative imaging and to remove some of the distortions, which can confound interpretation of MPI. Many scatter compensation techniques have been developed and evaluated, and are systematically reviewed (Zaidi and Koral 2004; Hutton, Buvat et al. 2011).

Finite spatial resolution is another critical factor that limits accurate estimation and interpretation of the activity distribution. Spatial resolution refers to the ability to differentiate objects in the spatial domain. It is the major cause of partial volume effects in emission computed tomography (ECT) images, and will be carefully discussed in a subsequent section. In SPECT, the resolution is characterized by the collimator-detector response (CDR), the image of a point source in the air. The CDR is determined by four main factors: (1) the intrinsic response of the detector, which denotes the imprecision in estimating the interaction position of gamma ray in the detector crystal; (2) the geometric response of the collimator, referring to the component of the response

resulting from photons that passed through the collimator holes; (3) the penetration response, resulting from photons that pass through the collimator septa (walls of the collimator holes) without interacting; and (4) the collimator scatter response, resulting from photons that scatter in the collimator septa and are detected. In PET, in addition to detector-related factors, two decay-physics-related factors inherently limit the spatial resolution. One is photon non-collinearity, meaning that the trajectories of the two annihilation photons are not exactly opposite. It stems from the nonzero net momentum of the positron at the time of annihilation. Since the energy at annihilation is a random variable, there is a random spread in the photon directions, resulting in imprecision in the LORs. The other effect is the positron range, which refers to the distance between the positron emission site and its annihilation position.

Generally, PET has superior resolution and sensitivity compared to SPECT and attenuation correction is simpler to implement. Multiple studies have demonstrated its comparable or improved CAD diagnostic accuracy (Marwick, Go et al. 1991; Bateman, Heller et al. 2006; Mc Ardle, Dowsley et al. 2012). However, SPECT is currently the most common MPI technique in clinical applications due to the widespread availability of scanners and lower costs (Di Carli and Hachamovitch 2006).

2.1.3 Stress and Rest Myocardial Perfusion Imaging

Regional myocardial blood flow depends on the driving pressure gradient and the resistance of the arteries. Due to compensatory arterial dilation, mild CAD may occur without reduced blood flow when the patient is at rest (Dilsizian and Narula 2013). In that case, MPI SPECT or PET, which images the underlying physiology, is unable to detect the stenosis in coronary arteries.

Typical MPI imaging protocols involve scanning the patient at rest and stress to produce two sets of perfusion images to assess the effects of stress on blood flow in coronary arteries. During stress, the heart rate will be elevated to its peak. The blood flow in healthy coronary arteries may be doubled or even tripled, making the relative flow reduction in stenosed arteries visible. The

stress can be induced either by exercise on, e.g., a treadmill or with intravenous pharmacological stimulation.

Comparison of stress and rest images allows the differentiation of ischemia from scar: the former corresponds to reversible perfusion defects that only exist in the stress image, while the latter corresponds to irreversible defects that are present in both images.

2.1.4 Gated Myocardial Perfusion Imaging

Conventional MPI does not consider cardiac motion during data acquisition, and the resulting perfusion image represents an average activity distribution of the beating heart. The introduction of electrocardiographically (ECG) gating into MPI can offer substantial additional information with only slightly increased cost. Currently, the majority of all myocardial perfusion SPECT studies are performed with gated acquisition (Williams 2005).

In cardiac gated MPI, data acquisition is guided by ECG signals to obtain multiple projection datasets corresponding to different phases of the cardiac cycle (Mannting and Morgan-Mannting 1993). This is accomplished by binning each detected photon into the appropriate projection dataset based on the temporal position within the cardiac cycle. Within each phase or gating interval, the heart is assumed to be frozen in time and free from cardiac motion. The projections of each particular ECG gating interval are reconstructed to generate a series of “snapshots” of the beating heart. The resulting sequence of 3D images throughout the cardiac cycle can be synthesized as a 4D image that characterizes myocardial perfusion along with the heartbeat. The images can also be analyzed to extract information about myocardial motion, thickening, and phase. Gated MPI can be performed in conjunction with stress and rest test (Dilsizian and Narula 2013).

Within a single study, gated MPI considerably increases diagnostic and prognostic capability by allowing an integrated evaluation of not only myocardial perfusion but also cardiac functions, such as ejection fraction, wall motion, and wall thickening (Paul and Nabi 2004).

Moreover, the heart movement may also facilitate perfusion interpretation. For instance, fixed perfusion defects not moving with the myocardium might represent attenuation or motion artifacts.

The summed projections of all gates are equivalent to the ungated acquisition. This implies that each gated image contains fewer counts than the ungated image. Consequently, ECG gating is not suitable for myocardial perfusion SPECT using ^{201}Tl labeled tracers due to the low counts that would be acquired in each gated frame, which would be likely to produce unusable noisy images.

2.1.5 Dynamic Myocardial Perfusion Imaging

The assessment of myocardial perfusion during stress and rest depends on relative tracer uptake to identify potential defects. One underlying assumption is that highest uptake corresponds to normal myocardium regions. However, these regions may also derive their blood supply from unhealthy coronary arteries, although they may be less severely diseased than those supplying regions with reduced uptake compared to the higher uptake regions. Consequently, using images of relative activity distribution may fail to diagnose the multi-vessel disease with uniformly depressed perfusion (Parkash, Ruddy et al. 2004). The other assumption is that radiotracer uptake is proportional to regional MBF. This is only an approximation for myocardial perfusion tracers except ^{15}O -water, the low counts of which makes it impractical in clinical diagnostic routine. In fact, the tracer uptake deviates from the line of identity and tends to underestimate the blood flow at high flows, which is known as the “roll-off” phenomenon (Dilsizian and Narula 2013). The underestimation may not affect the identification of perfusion defects of high severity, but may compromise the detection of early-stage CAD with mildly reduced blood flow. In order to improve diagnosis accuracy, it is beneficial to evaluate not only relative radiotracer uptake but also the underlying absolute MBF.

Dynamic imaging plays an essential role in the estimation of absolute MBF. It involves the acquisition of a time series of perfusion images to capture the dynamic process of the uptake,

retention, redistribution and wash-out of the injected radiotracer. The dynamic images contain considerably more information about the underlying physiology than static imaging. The subsequent quantitative analysis using kinetic modeling (introduced later) can yield an estimate of absolute regional MBF in units of ml/g/min. The advantages of dynamic imaging over relative perfusion imaging in improving diagnosis have been demonstrated in several studies (Hajjiri, Leavitt et al. 2009; Yoshinaga, Katoh et al. 2011).

Temporal resolution is of great significance for dynamic imaging. It is determined by as how frequently the scanner can generate useable images of the targeted object. Detectors in conventional SPECT are rotated to acquire data at a complete set of projection angles for tomographic reconstruction. In contrast, stationary ring detectors in PET allow essentially continuous list-mode acquisition of photon pairs from any LOR, which provides data from in all projection angle, resulting in better temporal resolution than SPECT. Though sonograms generated from very short durations will be very noisy. Meanwhile, accurate quantification of absolute tracer uptake is a necessity of effective kinetic modeling. PET has higher resolution, higher sensitivity and has traditionally emphasized quantitative reconstruction, which also has contributed to the dominant role of PET in measuring absolute MBF with dynamic imaging.

2.2 Image Reconstruction

Image reconstruction is essentially the inverse process of forward projection and aims at recovering the true radioactivity distribution within the body from acquired projection datasets. Reconstruction algorithms are categorized into analytic and iterative reconstruction methods.

2.2.1 Analytical Image Reconstruction

Filtered backprojection (FBP) is the most commonly used analytical tomographic reconstruction algorithm in clinical practice due to its straightforward implementation and computational

efficiency. It is mathematically derived as an inverse transform of the 2D Radon transform, where the value of each projection bin is modeled as a line integral across the radioactivity distribution. The derivation is based on the Fourier Slice Theorem: For a 2D activity distribution, the Fourier transform of the 1D projection at certain acquisition view corresponds to the 2D Fourier transform of the activity distribution along a line through the origin making an angle with the x-axis equal to the projection angle. Therefore, the 2D Fourier space can be completely recovered from 1D projections acquired at a dense set of projection angles, laying the theoretical foundation for reconstruction.

Despite its widespread applications, FBP lacks the ability to model many physical factors in the image formation process, including photon attenuation and scatter, statistical noise, and collimator-detector response. Therefore, the reconstructed image has limited quantitative accuracy and the images are not an accurate representation of the activity distribution.

2.2.2 Iterative Image Reconstruction

Iterative reconstruction algorithms have the ability to accurately model the photon emission and detection process, leading to, in principle, better image quality, and superior quantitative accuracy. Statistical iterative reconstruction algorithms take into account the random nature of the decay and detection process.

The most commonly used statistical iterative algorithm, maximum likelihood expectation maximization (ML-EM), is based on the assumption of Poisson distribution of counts in the projection bins. This is taken into account by the use of the ML in judging when the projection of the estimated image is a good match to the measured projections. The ML-EM algorithm seeks the image that maximizes the statistical (log) likelihood using the EM algorithm. The objective function is given by:

$$\hat{\mathbf{f}} = \arg \max_{\mathbf{f} \geq 0} \{\log \Pr(\mathbf{g}|\mathbf{f})\}$$

where $\mathbf{f} \in \mathbb{R}^{N \times 1}$ is a vector representing the expected activity distribution in voxels, N is the number of voxels in the reconstructed image, $\mathbf{g} \in \mathbb{R}^{M \times 1}$ is the measured projection data vector, and M is the number of projection bins. The likelihood function is expressed as:

$$\Pr(\mathbf{g}|\mathbf{f}) = \prod_{j=1}^M \frac{\exp(-(\mathbf{H}\mathbf{f})_j)(\mathbf{H}\mathbf{f})_j^{g_j}}{g_j!}$$

where $\mathbf{H} \in \mathbb{R}^{M \times N}$ is the system matrix modeling physical effects in the projection process. Its element h_{ij} represents the probability that an emission event in voxel j of the activity distribution image will be detected in projection bin i .

Like general iterative algorithms, ML-EM starts from an initial estimate of the image. The first step in iteratively updating the estimate is to compute the forward projection of the current image estimate. The resulting estimated projection is then compared to the acquired projection to produce an error term, which is subsequently backprojected into the image domain to refine and update the current image estimate. The update equation is expressed as:

$$f_j^{(n+1)} = \frac{f_j^{(n)}}{\sum_{i=1}^M h_{ij}} \sum_{i=1}^M h_{ij} \frac{g_i}{\sum_{k=1}^N h_{ik} f_k^{(n)}}$$

As the process repeats, higher spatial frequencies are gradually incorporated into the reconstructed image. Since high-frequency information tends to be dominated by noise, image noise tends to increase with iteration (Lalush and Wernick 2004). Usually, the iterative process is terminated before reaching the ML solution to produce an image with suitable visual image quality.

The primary shortcoming of ML-EM is its computational inefficiency, which mainly stems from the repeated forward projection and back projection processes. To solve this the ML-EM method was later modified using block iterative methods to create the ordered-subsets expectation maximization (OS-EM)(Hudson and Larkin 1994). In OS-EM, the projection dataset is partitioned into ordered subsets based on projection views. Instead of generating the projection estimate and backprojecting the error from all views at every iteration, the reconstructed image is updated using

these subsets of the full projection dataset. In other words, each iteration in ML-EM, which updates the image estimate once, is separated into sub-iterations in OS-EM that update the estimate multiple times, with each update using only a subset of the projection data. The number of updates is equal to the number of subsets. This results in a speed up in convergence by a factor that is equal approximately to the number of subsets. Despite the speed improvement, OS-EM still takes much longer to finish than FBP, with each iteration approximately equal computationally to an FBP reconstruction even without modeling the imaging physics. However, present computers have sufficient computational power that that iterative reconstruction algorithms are usable in routine clinical practice.

2.2.3 Regularization and Maximum A Posterior (MAP) Reconstruction

An interesting phenomenon is observed in ML-EM reconstruction: As the iterations progress, the likelihood function quickly reaches a plateau with little increment afterward, but the image estimate continues to change visually and becomes increasingly noisy. This can be attributed to the ill-posedness of image reconstruction. Inverse problems are often ill-posed, meaning that one or more of the following three conditions exist in the sense of Hadamard: (a) A solution does not exist; (b) The solution is not unique; (c) The solution does not continuously depend on the given data (Hadamard 2003).

It is desirable to obtain numerically stable solutions in practical applications. Two approaches are available to impose global constraints on the possible image estimates. One is to introduce a regularization term with whose weight with respect to the data-fit (e.g., log-likelihood) term is controlled by an adjustable parameter. The purpose of this term is to penalize undesirable (e.g., noisy) solutions, and examples of regularization are Tikhonov and total variation regularization (Rudin, Osher et al. 1992). The other is called maximum a posterior (MAP), which tries to find the most probable image estimate given the measured projection datasets. It differs from ML criterion in that a prior probability distribution is associated with the image estimate,

making some estimates more likely than others even without the given data. For instance, a Gibbs distribution has been introduced to encourage smoothness in the desired image to suppress noise in ML solution (Geman and Geman 1984). The prior distribution frequently involves the use of a weight and other hyperparameters that control the magnitude and other aspects of regularization. It turns out that the two techniques are operationally equivalent: both incorporate extra assumptions or prior knowledge about the original image in an attempt to control undesirable features in the reconstructed image (Puetter, Gosnell et al. 2005).

Comparing to ML, the incorporation of regularization can reduce or eliminate ill-posedness and stabilize the solution on one hand, while lead to anticipated images on the other hand. However, the choice of regularization parameter is critical in achieving the above objectives. Usually, the prior information in regularization is not accurate or specific about the actual activity distribution and instead encourages general features of the images such as smoothness, edge preservation, etc. Large values of the prior or regularization term weight parameter can bias the image estimate, for example resulting in as an over smoothed image when using a Gibbs prior.

2.3 Image Analysis

2.3.1 Myocardial Perfusion

SPECT and PET reconstruction generates a 3D image that can be viewed as a set of transaxial images, which are cross-sectional slices perpendicular to the axis of the body. Due to different heart orientations in patients, the transaxial images are reoriented and displayed in short-axis, vertical and horizontal long-axis slices in order to provide a patient-independent and easy to understand anatomical orientation that is relatable to myocardial vascular anatomy. The 3D perfusion status is also often summarized in a 2D polar map to facilitate interpretation. Typically, the map consists of concentric rings representing the activity concentration in circumferential profiles of short-axis slices with the radius proportional to the distance to the apex (DePasquale, Nody et al. 1988).

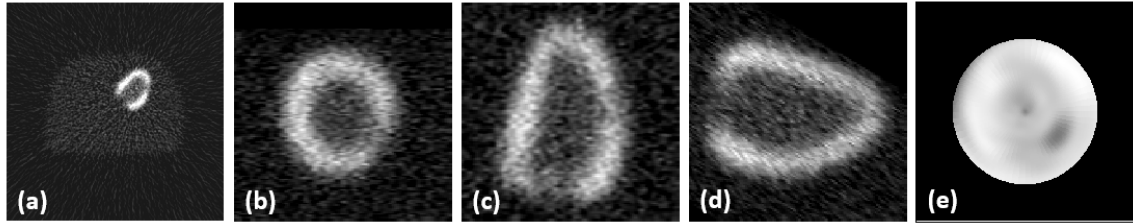


Figure 2-1. (a) a transaxial slice; (b) a short-axis slice; (c) a horizontal long-axis slice; (d) a vertical long-axis slice; (e) the polar map.

Several methods of myocardial perfusion images are introduced as follows.

a. Visual Analysis

The MPI images can be visually interpreted to identify the presence, location, severity, and extent of possible perfusion defects. Myocardial regions with the highest radiotracer uptake are assumed to be normal while regions with relatively low uptake are likely to result from perfusion defects. Defect severity is typically expressed as mild, moderate, or severe, depending on the image intensity in the defect with respect to the normal myocardium. The defect extent may be described as small, medium, or large (Hansen, Goldstein et al. 2006) or in terms of the percent of the myocardial volume in quantitative analysis. The diagnosis depends on relative activity uptake to differentiate abnormality.

b. Semiquantitative Visual Analysis

Visual interpretation has been standardized on the basis of a validated segmental scoring system to provide reproducible assessments (Berman, Kiat et al. 1991). Based on a standard 17-segment model (Cerqueira, Weissman et al. 2002), the LV is divided into three major short-axis regions (basal, mid-cavity and apical) and the apex. The basal and mid-cavity slices are further divided into six circumferential segments, and the apical slices into four segments. Each segment corresponds to a specific vascular territory. A score between 0 and 4 is assigned to each segment according to the perceived uptake of the segment: 0 for normal perfusion, 4 for absent uptake. Furthermore, the segmental analysis plays a significant role in characterizing global perfusion status: the sums of the scores of all segments serves as a measure of global

perfusion deficit. For instance, the summed difference score (SDS), defined as the difference between the summed stress score and the summed rest score, is a measure of the degree of reversibility.

c. Quantitative Analysis

Although visual analysis can provide useful diagnostic and prognostic information, it may not be inconsistent between interpretations due to differences in reader interpretation skill or different display media. Quantitative analysis can offer a more objective and reproducible diagnosis and has become an important supplement to visual analysis. It usually requires the development and validation of normal databases and related regional abnormality thresholds, which depend on many factors such as patient's gender, type of radiotracer, and imaging protocols. In this analysis, the polar map is normalized by the average activity concentration in the myocardium. When the normalized uptake falls below a specified limit, for instance, more than 2.5 standard deviations below the mean in the normal database, the specific region is deemed abnormal (DePasquale, Nody et al. 1988). Note that an overlap always exists between normal patients and those with mild defects because of imperfect imaging systems and inter-patient variations.

d. Tracer Kinetic Modeling

A tracer kinetic model describes quantitatively the rate of exchange of radiotracer between the blood and the arrows tissue compartments as a function of time. In kinetic modeling of myocardial perfusion SPECT, two time activity curves (TAC) are typically derived from the sequence of images: one for each from the blood pool and myocardium ROIs, representing the activity concentration in these organs over time. The TACs are input into a kinetic model to estimate model parameters relating to absolute MBF. In addition to the selection of appropriate kinetic models, quantitative measurement of activity concentration is also crucial to accurately estimate absolute MBF.

2.3.2 Left Ventricular Function

Left ventricular function can also provide useful diagnostic and prognostic information about CAD. It assesses the performance of heart as a blood pump. Anatomical imaging modalities such as echocardiography and MRI are typically used as the gold standard of cardiac function assessment. In spite of relatively poor image quality, gated myocardial perfusion SPECT and PET images can roughly depict LV structure and thus also be employed in LV functional analysis. The feasibility and accuracy have been demonstrated by several studies (Goris, Thompson et al. 1994; Germano, Kiat et al. 1995; Everaert, Franken et al. 1996). Several important parameters of LV function will be introduced in the following.

Ejection fraction (EF) measures the percentage of blood pumped out of the LV per beat:

$$EF = \frac{EDV - ESV}{EDV} \times 100\%.$$

End-systolic volume (ESV) quantifies the volume of blood in the ventricle at the end of the heart contraction. End-diastolic volume (EDV) quantifies the volume of blood in the ventricle at the end of filling. The cavity volumes can be calculated as the product of a single voxel's volume and the number of voxels bounded in the estimated endocardial surface and the valve plane.

Wall motion (WM) assesses the movement of myocardium wall position throughout the cardiac cycle, a significant marker of left ventricular function. It can be quantified as the distance between corresponding points on the detected endocardial surfaces between end-diastole and end-systole (Faber, Akers et al. 1991).

Wall thickening (WT) assesses the variation of LV myocardium wall thickness between end-diastole and end-systole. The thickness can be measured as the distance between the estimated endocardial and epicardial surfaces (Germano, Erel et al. 1997). WT is an important indicator of systolic function and myocardium viability. It can be used to differentiate passive wall motion from active myocardial contraction.

To evaluate these function parameters, one significant requirement is to accurately segment the LV and delineate the endocardial and epicardial surfaces at end-systole and end-diastole of the cardiac cycle from gated MPI images.

2.4 Partial Volume Effects

The analysis of both myocardial perfusion and cardiac function are significantly affected by partial volume effects (PVEs). These result from two distinct phenomena: one is the blurring due to the finite spatial resolution of the imaging system, while the other is the digital image representation with a finite voxel size (Soret, Bacharach et al. 2007). The blurring causes activity spillover between the targeted region and the neighboring regions in the reconstructed images, leading to an underestimation of myocardial activity concentration in perfusion imaging. The finite resolution of SPECT is determined by factors including the detector intrinsic resolution, collimator design, and reconstruction filtering (Jaszczak, Coleman et al. 1981) and varies at different locations and along different directions. The blurring process can be modeled as the convolution with the system point spread function (PSF). The effect of finite voxel size is modeled as downsampling from high-resolution images, known as the tissue fraction effect. It occurs at region boundaries, where the voxels partially overlap with multiple tissue types and contain a mixture of activities. The two effects can be modeled sequentially or integrated into one linear partial volume operator (Rousset, Rahmim et al. 2007). The voxel size of SPECT and PET images is normally on the order of one-half to one-third of the FWHM spatial resolution. Thus, the tissue fraction effect is not negligible, but the final blurring effect resulting from finite imaging system spatial resolution plays the dominant role in PVEs.

The severity of PVE is also closely related to the object size. Voxels in a distance of less than two system resolution FWHMs away from object boundaries are significantly affected (Hoffman, Huang et al. 1979; Yoshida 1989). However, the thickness of left ventricular

myocardium generally falls below the resolution range of current clinical nuclear cardiac imaging systems, which roughly have 10-15mm FWHM for SPECT and 5-10mm for PET (Wells 2016).

As a result, PVEs are an important limiting factor in the analysis of myocardial perfusion images. Quantitatively, PVEs alters absolute measurements of radiotracer uptake. Qualitatively, PVEs distort the appearance of actual radioactivity distribution and thus undermine the accuracy of visual interpretation when the wall thickness varies. For instance, thinner myocardium regions will appear dimmer even if the entire myocardium has the same radiotracer concentration, which may lead to a false-positive diagnosis. Comparison with normal databases decreases the need for absolute quantification, but the accuracy is still compromised due to the anatomy difference with the normal patients (Galt, Garcia et al. 1990).

2.5 Partial Volume Compensation

Many partial volume compensation (PVC) methods have been proposed to restore the underlying true activity distribution in PET and SPECT images (Erlandsson, Buvat et al. 2012). Usually, additional data such like coregistered high-resolution CT or MRI images are needed to address the tissue fraction effect (Aston, Cunningham et al. 2002). The anatomical image is registered to the functional image and ROIs are delineated and downsampled to match the voxel size. Such that the fractional contribution of each tissue classes can be determined for voxels on the boundaries (Boening, Pretorius et al. 2006; Pretorius and King 2009). The compensation demands accurate registration and segmentation to be effective. In the literature, limited studies have been conducted to address this issue and most of them were applied to simulated data. The work in this study does not use anatomical images and thus ignores the tissue fraction effect and concentrates on the compensation for the blurring effect.

PVC methods can be classified into different groups according to different standards. The effect of the system PSF can be reduced by modeling resolution during the image reconstruction

process (Tsui, Frey et al. 1994; Reader, Julyan et al. 2003), or after image reconstruction using a deconvolution operation (Teo, Seo et al. 2007; Tohka and Reilhac 2008). The former directly enhances the effective resolution of the system to minimize PVE in the reconstructed image, while the latter attempts to reduce the remaining PVE with combined resolution modeling in both projection and reconstruction. The two types of compensation are not mutually exclusive that they can be performed sequentially to achieve increased resolution recovery. Deconvolution-based PVC methods typically necessitate prior knowledge about the PSF and noise characteristics in the given nuclear medicine image in order to reverse the blurring process. Due to the intrinsic ill-posedness of the inverse problem, they suffer from high-frequency noise amplification and thus regularization is usually needed to stabilize the solution. The primary advantage of these methods is that require only the emission image but not anatomical images of the same patient, which may not be available because of the additional cost or radiation exposure.

Whether coregistered high-resolution structural images are used is an alternative criterion of categorizing PVC methods. Generally, the high-frequency structural information included in the segmented ROIs can further reduce the spillover effect, leading to improved PVC performance compared to deconvolution-based methods. Some ROI-based PVC techniques assume uniform intensity within each region and estimate the corresponding mean value after correction. For instance, the recovery coefficient (RC) method (Hoffman, Huang et al. 1979) defines the coefficient as the fraction of the original total activity inside the target ROI after resolution blurring. The regional mean activity in the measured image is scaled by the reciprocal of the RC to recover the truth. The RC method assumes zero activity in the background outside the target ROI and compensates for spill-out activity only. The RC method has been extended to compensate for both spill-out and spill-in by analogously defining recovery and cross-talk coefficients between multiple regions. This method is referred to as the geometric transfer matrix (GTM) method (Rousset, Ma et al. 1998). On the other hand, some ROI-based PVC techniques compensate for PVEs in each individual voxel in the ROI. For example, the Muller-Gartner method compensates for spill-in and

spill-out while preserving activity heterogeneity in the target ROI. It first subtracts the spill-in activity, which is estimated by blurring the assumed homogeneous background regions with known concentrations with the PSF. It then corrects for the spill-out similarly to the RC method by dividing a template image of recovery coefficients in the ROI. The method was modified for use in combination with the GTM method to estimate uptake concentrations in the background regions (Quarantelli, Berkouk et al. 2004). It has also been adapted to iteratively perform PVC on multiple regions in a cardiac PET study (Du, Madar et al. 2013).

However, several shortcomings are associated with these ROI-based PVC methods. In addition to the limited availability of anatomical images, they are sensitive to registration and segmentation errors (Zaidi, Ruest et al. 2006). It would be appealing if the prior geometric information about the target object could be employed for use in PVC while avoiding the challenges associated with registering and segment these anatomical images. Some approaches have attempted to directly delineate endocardial and epicardial contours from nuclear cardiac images and use the resulting ROIs for compensation (Nuyts, Maes et al. 1996; Dumouchel and deKemp 2011). However, the PVC performance of these methods is compromised by the limited segmentation accuracy.

2.6 Left Ventricle Segmentation

Many dedicated segmentation methods have been developed or adapted from the image processing domain. Some merely exploit low-level information such as voxel intensities within the image. Thresholding depends on contrasting intensity level to extract the myocardium, which is typically more perfused than neighboring regions in MPI. Edge detection uses the intensity discontinuity between regions to form a list of voxels representing myocardium boundaries. However, the accuracy of segmenting medical images is greatly restricted by three major image-related problems (Withey and Koles 2007). First, the myocardium is usually not uniformly perfused such that there

is a mismatch between radiotracer uptake and the underlying anatomical regions. When perfusion defects are present, the resulting myocardium might be disconnected. Second, statistical noise from radioactive decay causes uncertainty in voxel intensities, which might produce jagged myocardial surfaces. Third, PVE reduces the intensity difference between tissue classes for voxels in the proximity of the boundaries, leading to the unreliable identification of myocardium surfaces.

High-level information about the targeted object to be segmented has been incorporated to improve the performance. One model-based approach attempted to detect the endocardial and epicardial surfaces with assumptions of LV shape, connectivity, and smoothness (Faber, Stokely et al. 1991). The shape information was encoded by sampling the two surfaces cylindrically in the basal portion and spherically in the apex portion with radials emitting from the LV axis. The gradient of each radial was computed to locate the maximal intensity changes as initial edge positions. They were iteratively modified to ensure the compatibility of neighboring surface points as an effort to model connectivity and smoothness of these boundaries. In addition to intensity gradient and smoothness of contours, another model-based delineation algorithm introduced a global LV shape constraint to detect myocardium boundaries (Nuyts, Suetens et al. 1991). The shape constraint modeled the endocardial or epicardial contour in the long-axis slice as two elliptic curves tangentially meeting at the apex. More recently a completely automatic algorithm estimated the midmyocardial surface by fitting it to an ellipsoid (Germano, Kiat et al. 1995). Two count profiles normal to the estimated midmyocardial surface in both directions were extracted and individually fitted with Gaussian functions. The endocardium and epicardial surface points were determined by moving the corresponding midmyocardial point inwardly and outwardly by a predefined percentage of standard deviations of the fitted Gaussians. LV segmentation methods using geometry models are able to effectively enhance robustness to perfusion defects and noise. However, none of these methods correct for PVE prior to segmentation or incorporate system PSF into segmentation. Consequently, the wall thickness is unlikely to be accurately estimated when segmenting myocardial perfusion SPECT/PET images (Yoshida 1989; Withey and Koles 2007;

Soneson, Ubachs et al. 2009). PVE reduces the usefulness of using image intensity gradient to measure edge location (Faber, Stokely et al. 1991). The position of the maximum gradient may significantly deviate from the true edge position (Nuyts, Suetens et al. 1991). Moreover, the impact of PVE depends on the corresponding wall thickness to be estimated. Empirically determined correction may improve edge detection in one case but not necessarily in another one.

Prior knowledge of image resolution was introduced into a model-based image analysis technique to delineate endocardial radius and myocardial wall thickness directly from ECG-gated cardiac PET images (Gambhir 1990). It has been evaluated in comparison with MRI or echocardiography in several studies (Porenta, Kuhle et al. 1995; Khorsand, Graf et al. 2003; Freiberg, Hove et al. 2004). This method modeled the underlying true radial profile that extends from left ventricle axis to the extracardiac region using a square wave. The 1D model was defined with five parameters: endocardial radius, wall thickness, blood pool activity, myocardial activity and background activity concentration. These model parameters were derived by least-squares fitting the resampled radial profile and the convolution of the 1D square wave model and the 1D system PSF. Theoretically, the resulting activity parameters are PVE compensated, indicating its application as a PVC method.

Some limitations are associated with this profile fitting technique. First, the 1D profile has relatively low counts and is likely to suffer from excessive noise. Second, the fitting may fail at those profiles through perfusion defects. Moreover, resolution loss is not confined to 1D radial profiles in 3D myocardial perfusion images.

To handle these issues, a PVC scheme merely applied the profile fitting technique to estimate ROIs and then performed ROI-based compensation for gated mouse PET images in higher dimensions (Dumouchel and deKemp 2011). Later the scheme was extended to a fully 3D implementation while circumventing the intermediate step of LV segmentation (Dumouchel, Thorn et al. 2012). The 3D model image, specified by tri-linearly interpolating a set of sampling radial profiles, was convolved with the 3D system PSF and then fitted into the OS-EM reconstruction of

measured data by minimizing the LS difference. This study focused on PVC that the estimation of geometry parameters was not assessed. Meanwhile, perfusion defects were absent and the noise level was relatively low in the measured data, which was insufficient to comprehensively evaluate the model-fitting method.

In summary, PVC and LV segmentation are intertwined that it is desirable to fuse them into one framework. On one hand, the prior geometric information employed in segmentation might benefit deconvolution-based PVC without accurate ROIs defined from high-resolution anatomical images. On the other hand, the resolution and noise information used in deconvolution-based PVC may also improve the delineation of myocardial boundaries. Therefore, this study proposed a model-based reconstruction method of nuclear cardiac images using geometry and activity distribution models to simultaneously achieve improved PVC and LV segmentation.

3. Materials and Methods

3.1 Geometry Model

The function of the geometry model is to provide an accurate representation of LV shape that is adjustable enough to accommodate patient differences with as few parameters as is reasonably possible in order to ease estimation. The LV shape resembles an ellipsoid or a truncated bullet. The proposed geometry model assumes that the long axis of the LV and the valve plane have been identified, though parameters describing these could also be incorporated into the model. As illustrated in Figure 3-1a, the model parameterizes the endo- and epi-cardial surfaces using a set of rays originating from the long axis of the myocardium. The rays are in planes perpendicular to the axis and at equiangular increments in the basal and mid-ventricular regions. In the apex, the rays radiate from a point with equal polar and azimuthal angular increments. The intersections of these rays with the two surfaces are specified by two parameters: the endocardial radius (r_i) and myocardium wall thickness (t_i) along the ray. The entire myocardial surface is obtained by separate cubic spline interpolating functions for each of the two surfaces that contain the intersection points. Generation of this surface was implemented with the aid of function *csape* in MATLAB (Release 2015b, The MathWorks, Inc., Natick, Massachusetts, United States). The resulting solid model defined by the two surfaces was then voxelized and filled with segmental activities to generate the model image.

The selection of sampling radial profiles is crucial for the geometry model. Typically, more samples and smaller sampling intervals can improve its capability of accurately describing geometry variability, but will also increase model complexity. In this study, the sampling scheme assumed that the most basal plane (valve plane) and the position of the apical epicardium had been manually estimated in advance to simplify implementation in this phase of development. These parameters determine the upper and lower bounds of the geometry model along the axis of the LV. The dividing point between the cylindrical coordinate used to describe the barrel of the myocardium

and the spherical coordinates used to describe the apical dome was located on the axis with two-fifths of the estimated axial extent of the LV from the lower bound. The cylindrical coordinate included four equally spaced planes perpendicular to the axis, eight rays around the axis in each plane. The spherical coordinate included eight rays emitting from the dividing point at an angle of 45° with respect to the axis and an additional ray on the axis. As shown in a later chapter, the sampling scheme had the ability to model the LV geometry based on XCAT phantom with an approximately 95% overlap of myocardium voxels.

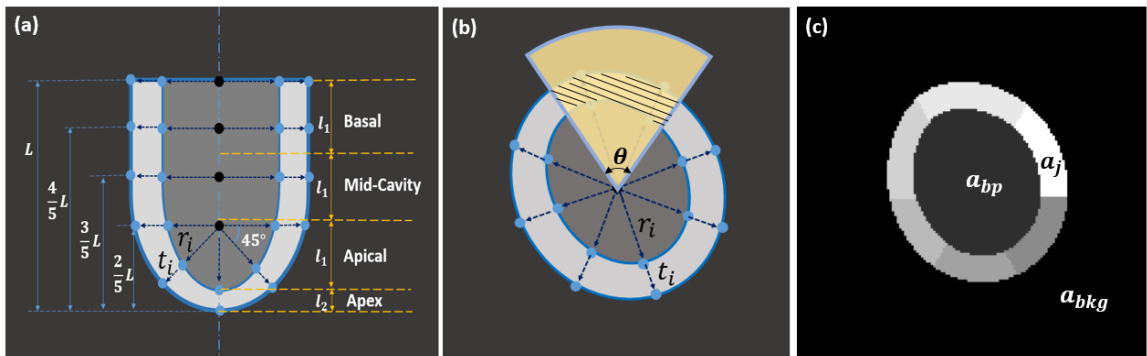


Figure 3-1. Illustration of the LV geometry model and the activity distribution model. (a) Long-axis view; (b) Short-axis view; (c) An example short-axis model image generated with 8 rays around the axis in the geometry model and 6 myocardial segments in the activity distribution model.

3.2 Activity Distribution Model

In addition to the geometry model, an activity distribution model is also required to specify tracer uptake in the resulting blood pool, myocardium and body background regions. Conventionally, the myocardial perfusion image is defined using voxels. However, interpretation of myocardial perfusion images does not rely on the value of every voxel. For instance, a two-dimensional polar map is often used to summarize the three-dimensional perfusion status. The voxels are redundant parameters in some sense. Therefore, the proposed model parameterizes the activity distribution using anatomically meaningful regions instead of voxels. It can significantly reduce the number of unknown parameters while preserving important diagnostic information.

The model divides the myocardium into segments are similar to those used in standardized myocardial quantitative analysis. It assumes uniform activity concentration in these segments (a_j) that in the blood pool (a_{bp}) and body background (a_{bkg}). Specifically, the reoriented LV is partitioned into four major short-axis slices: basal, mid-cavity, apical, and apex. The apex slice does not contain the blood pool and the myocardium in this slice is treated as a single segment. In the other three slices, the myocardial ring is further divided into a number of equiangular segments. Each segment is defined as the intersection region (shadowed area) with a circular sector that starts from the axis with a predefined central angle θ . The angular position of the first segment is controlled by a parameter, and other segments follow sequentially without gaps between them.

The number of segments is variable and their positions do not necessarily correspond to rays in the geometry model. More segments can improve local activity estimation but would also increase model complexity as well as the sensitivity to noise. For simplicity, this study remains consistent with the standardized 17-segment model: six segments each for the basal and mid-cavity slices, four segments for the apical slice and one for the apex slice. Note that there exists a 30° offset of the angular position parameter between the six- and four-segment slices.

3.3 Imaging System Model

A voxelized model image f_p can be produced from the geometry and activity distribution model parameters \mathbf{p} defined above

$$\mathbf{p} = (r_1, r_2, \dots, r_{N_r}, t_1, t_2, \dots, t_{N_r}, a_1, a_2, \dots, a_{N_s}, a_{bp}, a_{bkg}),$$

where r_i and t_i ($i = 1, 2, \dots, N_r$) denote the endocardial radius and wall thickness parameters along N_r sampling rays in the geometry model, a_j ($i = 1, 2, \dots, N_s$) denote the activity concentrations of N_s myocardial segments, and a_{bp} and a_{bkg} denote the activity concentration in the blood pool and body background, respectively. The values of the model parameters are estimated by adjusting

them to fit the model image to the observed data. The goodness of the fit is judged in terms of the model of the image formation process.

For either SPECT or PET, a general linear imaging system can be used to describe the formation of the projection images:

$$\mathbf{g}_0 = \mathbf{H} \cdot \mathbf{f} + \mathbf{n}_{Poisson},$$

where \mathbf{g}_0 is a vector in the projection space and represents the observed projection data, \mathbf{f} is a vector in the image space and represents the original voxelized activity image, and $\mathbf{n}_{Poisson}$ denotes the projection space vector representing the uncorrelated Poisson noise in the projection bins. Note that \mathbf{H} is the system matrix modeling the physical effects in the projection process, such as attenuation, scatter and detector response. Element h_{ij} is the probability that an emission event in voxel j of the activity distribution image will be detected in projection bin i . The system matrix can be simple or complex as desired. This study focused on PVEs and PVC, and thus only factors related to the degraded spatial resolution were included in order to reduce computational cost. In particular, photon attenuation and scatter were ignored.

In the image domain, the observed image \mathbf{f}_0 can be written in terms of a general reconstruction operator \mathcal{R} as follows.

$$\mathbf{f}_0 = \mathcal{R}(\mathbf{g}_0) = \mathcal{R}(\mathbf{H} \cdot \mathbf{f} + \mathbf{n}_{Poisson})$$

FBP reconstruction is a linear process and the reconstruction operator \mathcal{R} can thus be described using a reconstruction matrix \mathbf{R} .

$$\mathbf{f}_0 = \mathbf{R} \cdot \mathbf{g}_0 = \mathbf{RH} \cdot \mathbf{f} + \mathbf{R} \cdot \mathbf{n}_{Poisson}$$

3.4 Objective Function

Instead of the intensities of all voxels, the proposed method estimates the parameters of the geometry and activity distribution models that give the best match between the image generated by the model and the measured data. The input image is contaminated by noise, so the metric for the goodness of fit was a statistical criterion based on the statistical likelihood, i.e., the probability that the image resulted from the given set of model parameters. A shape constraint was also incorporated to regularize the ill-posed reconstruction problem and increase the robustness to perfusion defects and noise. The model parameters were optimized by seeking the minimum of an objective function that quantifies the model matching. It consists of two components: one is a data-fitting term that encourages fitting to the observed data based on maximum likelihood (ML) criterion, either in the projection domain or in the reconstructed image domain; the other component is a regularization term that penalizes deviations from a priori assumption about the model parameters.

3.4.1 Data-Fitting in the Projection Domain

In the imaging model, each projection bin follows an uncorrelated Poisson distribution. In the ML component of the objective function, the mean is assumed to be equal to the projection of the activity image being estimated. The resulting likelihood function $L(\mathbf{p})$ is given as follows

$$L(\mathbf{p}) = Prob(\mathbf{g}_O | \mathbf{f}_P(\mathbf{p}); \mathbf{H}) = \prod_{j=1}^M \frac{\exp(-g_{Pj}) g_{Pj}^{g_{Oj}}}{g_{Oj}!}.$$

In the above function, M denotes the number of projection bins, g_{Oj} represents the counts in the j th bin of the observed projection data, and \mathbf{g}_P denotes the projection of the estimated image $\mathbf{g}_P = \mathbf{H} \cdot \mathbf{f}_P$.

The ML estimator maximizes $L(\mathbf{p})$ to seek the object model parameters \mathbf{p} that makes the observed projection datasets most probable (i.e., highest value of the likelihood). The data-fitting

term can equivalently maximize any monotonic transformation of the likelihood term, for example the log-likelihood function, to simplify the computation. The expression is shown below, with image-independent constants removed:

$$\max_{\mathbf{p}} \sum_{j=1}^M (g_{Oj} \log g_{Pj} - g_{Pj}) .$$

3.4.2 Data-Fitting in the Image Domain: FBP

It has been shown that noise statistics in FBP reconstructed images can be well approximated as a multivariate normal distribution (Papoulis and Pillai 2002), which is derived from the central limit theorem and the fact that FBP is a weighted sum of independent projection data. Thus the statistical likelihood of the parameters can be modeled using:

$$pdf(\mathbf{f}_O) = \frac{1}{\sqrt{(2\pi)^k |\Sigma|}} \exp\left(-\frac{1}{2}(\mathbf{f}_O - \boldsymbol{\mu})^T \boldsymbol{\Sigma}^{-1}(\mathbf{f}_O - \boldsymbol{\mu})\right).$$

In the above equation, $\boldsymbol{\mu}$ denotes the image generated from the model parameters, or $\boldsymbol{\mu} = \mathbf{RH} \cdot \mathbf{f}_P$, and $\boldsymbol{\Sigma}$ is the $k \times k$ covariance matrix and dependent on $\boldsymbol{\mu}$.

Due to the large size of the covariance matrix, the involved matrix inverse and multiplication operations make the evaluation of the likelihood function computationally intensive. Additionally, it has been shown that FBP noise variance remains relatively constant for all pixels regardless of the original image pattern (Wilson and Tsui 1993). If we assume zero noise correlations as well as uniform noise variance, or equivalently, independent identical Gaussian noise in the pixels, the covariance matrix can be replaced by a diagonal matrix with identical non-zero diagonal elements. The resulting log-likelihood function can be formulated as follows.

$$\log L(\mathbf{p}) = -k_1(\mathbf{f}_O - \mathbf{RH}\mathbf{f}_P)^T \cdot (\mathbf{f}_O - \mathbf{RH}\mathbf{f}_P) + k_2$$

where k_1 and k_2 are constant scalars that can be ignored during optimization. Therefore, the ML criterion is reduced to a least-squares (LS) expression:

$$\min_{\mathbf{p}} \sum_{i=1}^N (f_{oi} - (\mathbf{RH}\mathbf{f}_{\mathbf{p}})_i)^2.$$

Accurately modeling the spatially-varying resolution in the reconstructed image is very time-consuming, especially when it must be performed once for each update of the parameters. In order to increase the efficiency, the resolution modeling can be approximated using a spatially invariant isotropic Gaussian kernel \mathbf{G}_{σ} . As a result, the modeling can be reduced to the convolution between the model image estimate and the Gaussian kernel, which can be implemented in the frequency domain along with FFT. The modified data-fitting objective is as follows:

$$\min_{\mathbf{p}} \sum_{i=1}^N (f_{oi} - (\mathbf{G}_{\sigma} * \mathbf{f}_{\mathbf{p}})_i)^2.$$

3.4.3 Data-Fitting in the Image Domain: OS-EM

As discussed in Chapter 2, the iterative OS-EM reconstruction algorithm has the advantage that it can be used to compensate for image degrading factors. As a result, it is desirable to have an image-domain objective function that is applicable to it. However, OS-EM is not a linear reconstruction algorithm, so a different objective function is needed. It has been shown that the OS-EM reconstruction algorithm approximately leads to log multivariate normal noise statistics in the image domain (Barrett, Wilson et al. 1994; Wilson, Tsui et al. 1994). In other words, the log of the reconstructed image follows a multivariate normal distribution. Intuitively, the data-fitting term with OS-EM reconstruction is to simply apply the procedure with FBP to the log of the reconstructed image. However, the uniform variance between pixels cannot be well approximated in the log image. The relationship between pixel variance and mean is approximately linear (Wilson

and Tsui 1993). Therefore, the pixel values of OS-EM reconstructed images were assumed to follow uncorrelated Gaussian distributions with variances proportional to the means. Since the mean image is not available, it is approximated with the observed image. With the spatially invariant Gaussian resolution approximation, the data-fitting objective function can be expressed as a weighted least square (WLS) objective function as follows:

$$\min_{\mathbf{p}} \sum_{i=1}^N \frac{(f_{oi} - (\mathbf{G}_{\sigma} * \mathbf{f}_{\mathbf{p}})_i)^2}{f_{oi}}$$

3.4.4 Regularization

Regularization is of great importance in stabilizing ill-posed reconstruction problems. It rejects improbable solutions by introducing prior knowledge about the uptake image or the target object. Compared to conventional pixel-based reconstruction, the proposed model-based method already implicitly includes regularization in the object model. For instance, the activity distribution model will automatically produce a piecewise uniform image without large pixel-to-pixel variations, excluding the necessity of an explicit regularization term to suppress noise. Furthermore, the geometry model ensures some degree of continuity of the resulting myocardium and the smoothness of the surfaces; otherwise, the presence of perfusion defects might lead to disconnected myocardial regions, and the image noise is likely to result in jagged boundaries. However, it may be desirable to incorporate additional information into the objective function using the geometry and activity distribution models.

Instead of using pixel-based regularization functions, we introduced a geometric constraint directly built on the model parameters. It encourages uniform wall thickness by favoring smaller variances of wall thickness parameters. The constraint further reduces the impact of perfusion defects and noise on greatly distorting the LV structure.

$$Var(t_j) = \frac{1}{N_r - 1} \sum_{j=1}^{N_r} (t_j - \bar{t})^2, \text{ where } \bar{t} = \frac{1}{N_r} \sum_{j=1}^{N_r} t_j$$

The objective functions that combine the data-fitting and regularization terms are summarized in the following.

The projection domain objective function with accurate resolution and noise modeling is:

$$\min_{\mathbf{p}} \sum_{j=1}^M (g_{Pj} - g_{Oj} \log g_{Pj}) + \beta \cdot \frac{1}{N_r - 1} \sum_{j=1}^{N_r} (t_j - \bar{t})^2.$$

The image domain objective function for FBP reconstructed images with accurate resolution modeling and approximated noise modeling is:

$$\min_{\mathbf{p}} \sum_{i=1}^N (f_{Oi} - (\mathbf{RH}\mathbf{f}_P)_i)^2 + \beta \cdot \frac{1}{N_r - 1} \sum_{j=1}^{N_r} (t_j - \bar{t})^2.$$

The image domain objective function for FBP reconstructed images with approximated resolution and noise modeling is:

$$\min_{\mathbf{p}} \sum_{i=1}^N (f_{Oi} - (\mathbf{G}_\sigma * \mathbf{f}_P)_i)^2 + \beta \cdot \frac{1}{N_r - 1} \sum_{j=1}^{N_r} (t_j - \bar{t})^2.$$

The image domain objective function for OS-EM reconstructed images with approximated resolution and noise modeling is:

$$\min_{\mathbf{p}} \sum_{i=1}^N \frac{(f_{Oi} - (\mathbf{G}_\sigma * \mathbf{f}_P)_i)^2}{f_{Oi}} + \beta \cdot \frac{1}{N_r - 1} \sum_{j=1}^{N_r} (t_j - \bar{t})^2.$$

In all the above, β is the regularization parameter that balances the relative strengths between the two terms. Note that the value of β is a user-selectable parameter that must be determined based on some criterion.

3.5 Optimization

Minimizing the objective function is the next component of the proposed method. It is difficult to analytically express the model image as a function of model parameters. Based on the complicated nonlinear mapping, the objective function is assumed to be nonconvex. Nonlinear and nonconvex functions are inclined to possess a variety of local minima, especially with a large number of parameters. Most optimization algorithms, such as gradient descent and Newton's method, are developed to find a local minimum based on the derivative of the function. For instance, zero first-order derivative is a necessary condition of a local minimizer for a continuously differentiable function in an open neighborhood. Therefore, it is challenging to globally optimize the proposed objective functions that no optimization algorithm can guarantee the achievement of the global minimum of the objective function.

3.5.1 Global Optimization: MultiStart

In order to increase the probability of achieving the global minimum, we used an optimization scheme named MultiStart. Since the value of optimized model parameters heavily depends on the initial estimate, MultiStart initializes the optimization with multiple points and then selects the result corresponding to the minimal objective function value. The initial points are randomly scattered or systematically positioned to cover likely candidates of the global minimum, in the hope that one or more are located in its "basin of attraction". With enough trials, the MultiStart method is more likely to achieve the global minimum. Although the success is not guaranteed without an infinite number of trials and initial parameter values that fully sample the parameter space, MultiStart is regarded as the gold standard of optimization in this study.

The MultiStart approach is not clinically practical because the computation time is proportional to the number of trials. It is desirable to explore optimization approaches that can find the global minimum with reduced computational effort. One approach is to find a better

optimization scheme, and the other is to find initial estimates that are close enough to the global estimate. The two approaches will be discussed in the following.

3.5.2 Efficient Optimization: Group-wise Alternating Scheme

We have proposed an optimization scheme to improve the computation efficiency. It divides the model parameters into several mutually exclusive groups. It then alternatively optimizes parameters in one group while fixing parameters in the others. The process is repeated until the difference in values of the objective function between consecutive iterations falls below a threshold. The scheme can greatly reduce the dimension of the parameter space in each of the partial optimizations. This is an attractive feature especially for the fully three-dimensional implementation that has a large number of parameters.

The parameter groups are of great importance to the optimization performance. It is desirable that these groups are relatively orthogonal, which can reduce the number of iterations and accelerate the convergence. In order to increase the inter-group independence, parameters of the same type should be grouped together. In particular, the endocardial radius, wall thickness and myocardial segmental activity parameters were separated into three groups. For the remaining two parameters, activity concentrations in the blood pool and background, using another two one-element groups would complicate the alternating scheme, but was unlikely to evidently improve the efficiency. Therefore, the group-wise alternating optimization scheme finally used three parameter groups. The first group determined the shape and activity of the blood pool region and consisted of the endocardial radius parameters and the blood pool activity concentration. The second group included all the myocardial segmental activity parameters. The third group was comprised of the background region activity concentration and wall thickness parameters. Alternatively, the parameters might be classified into a group of geometry parameters (radius, thickness) and a group of activity concentrations. But the alternating optimization scheme using

the two groups was less effective than using the proposed three groups, which will be shown in Chapter 5.

The optimizing order of the three groups can have a considerable impact on the optimization result. According to a coarse-to-fine rule, the alternation should start from parameters that have the largest effect on the value of the objective function. Typically, the wall thickness of an initial estimate is uniform and selected from a reasonable range, and the initial concentrations are estimated as the mean activity of corresponding ROIs. These parameters are close to the true values to some extent. The endocardial radii thus largely determine the activity distribution in the model image. If the radius parameters were significantly mismatched, the fitting of other parameters would become futile. Therefore, the first group was optimized first. It is difficult to make informed decisions about the order of the other two groups. The two possibilities of the alternating order (1st, 2nd, and 3rd; 1st, 3rd, and 2nd) were later compared in a perturbation study of initial points. Basically, the alternating optimization was applied with regard to various sets of initial points that were randomly selected from perturbation intervals of different model parameters. The resulting objective function and model parameters were used to assess the optimization performance, the details of which will be revealed in Chapter 5. The results imply that it was favorable to optimize the second group prior to the third one, resulting in the agreement of the final alternation order and the group index.

In this study, each optimization run, either for one trial in the MultiStart method or a subgroup execution in the group-wise alternating scheme, was implemented using function *fmincon* in MATLAB. *fmincon* is a gradient-based method and aims at finding the minimum of constrained nonlinear multivariate functions. The optimization used the interior-point algorithm (Byrd, Gilbert et al. 2000). Without an analytical expression of parameter updating, the iterative process of fitting the geometry and activity distribution models to the observed data in the image domain is approximately summarized in Figure 3-2.

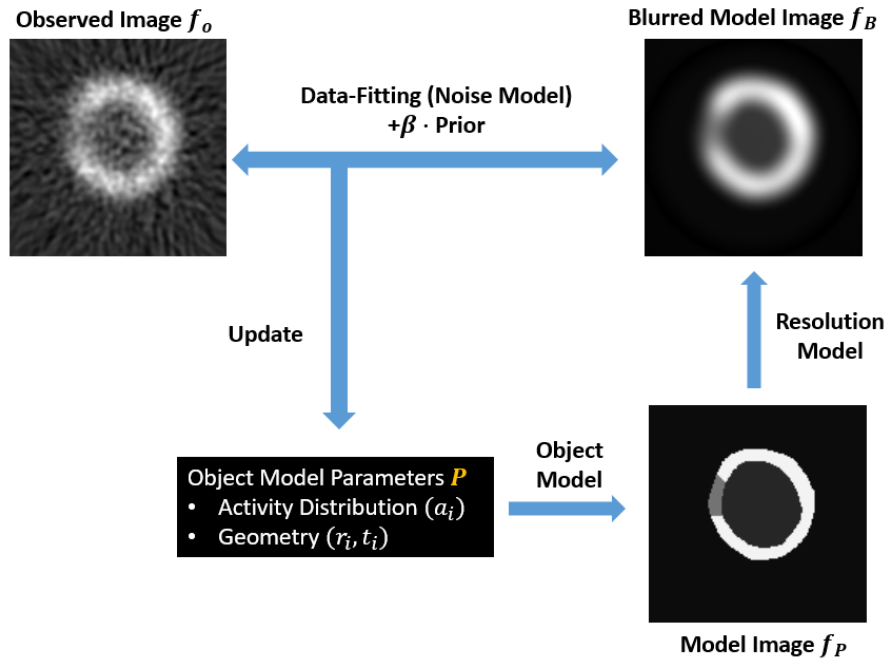


Figure 3-2. The iterative fitting process of the model-based reconstruction in the image domain.

3.5.3 Initial Parameter Estimation

A perturbation study described in Chapter 5 showed that the group-wise alternating scheme greatly reduced the dependence of ultimate results on the initial points comparing to direct optimization of all parameters. In general, it was insensitive to perturbations in the initial estimates of all the model parameters except the wall thickness. This result implies that the errors resulting from poor initial estimates of the radius and activity parameters can be compensated for during optimization. Thus it is not critical to find very good initial estimates of these parameters. However, a close initial guess is still beneficial in terms of speeding up convergence.

Many methods in the literature can be adapted to estimate initial model parameters from the given cardiac image, such as fitting a square wave model to radial count profiles originating from the axis (Dumouchel and deKemp 2011). However, the 1D method is sensitive to image noise and perfusion defects. Thus an improved but relatively simple method was proposed to derive initial parameters from short-axis slices. The proposed method was based on the fact that the

myocardium normally has higher tracer uptake than adjacent regions in myocardial perfusion SPECT/PET images. Note that potentially high uptake in extra-cardiac regions is assumed to have been masked out in the cardiac image to be fitted. Based on the approximately circular short-axis LV shape, the method aimed at finding the endocardial radius that maximizes the summed activity in the myocardium ROI. The ROI was determined by the radius and a predefined constant wall thickness. After obtaining the geometry model parameters, the initial concentration parameters were calculated as the regional mean activity of corresponding ROIs, resulting in the same initial activity concentrations for all segments. The 2D initial parameter estimation is illustrated in Figure 3-3. In this method, we observed that the activity concentration was typically overestimated in the blood pool and background but underestimated in the myocardium due to PVEs.

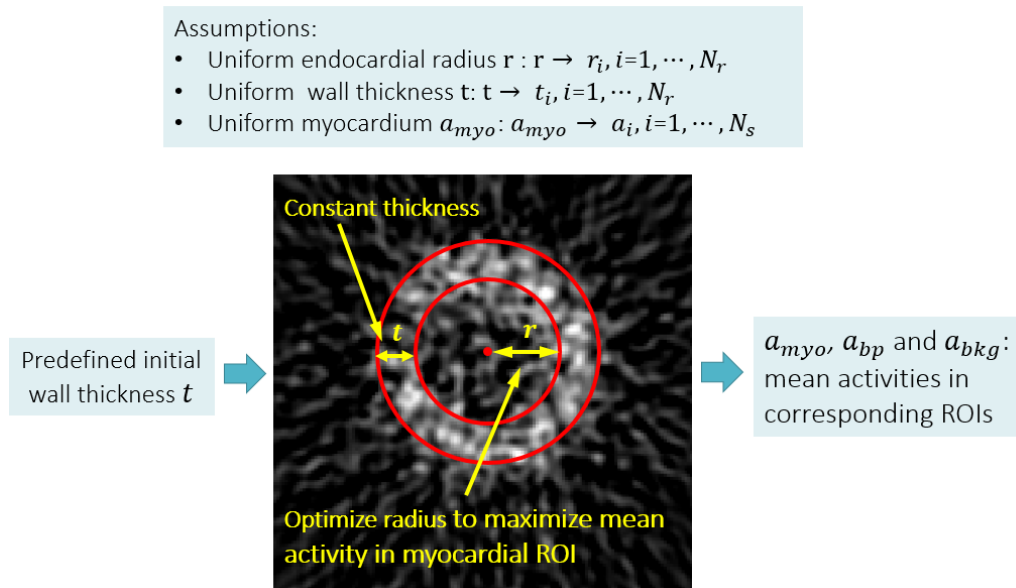


Figure 3-3. Illustration of generating a 2D initial estimate from a short-axis slice for a predefined initial wall thickness.

Because the alternating optimization scheme was sensitive to errors of the wall thickness in the initial estimate, the above procedure was repeated to generate multiple trial sets of initial parameters based on different wall thicknesses. These trials were optimized in parallel and the result with the minimal objective function was regarded as the globally optimized model parameters. The

average wall thickness measured with echocardiography was $8.6 \pm 1.3\text{mm}$ at diastole and $11.5 \pm 1.3\text{mm}$ at systole (Nuyts, Maes et al. 1996). Therefore, eleven initial values of the myocardial wall thickness were used in this study ranging from 7.5mm to 12.5mm in increments of 0.5mm . Compared to the MultiStart method, this alternating method significantly reduced the number of optimization trials while maintaining comparable optimization effectiveness.

In the preliminary 3D implementation, the short axis slices of the reoriented perfusion image were first fitted slice-by-slice using the method above. Figure 3-4 displays the flowchart of generating a 3D initial estimate. For each thickness trial, an initial estimate was generated and optimized using the group-wise alternating scheme for each slice. The slice-by-slice fitting results were then synthesized into a 3D initial estimate, as revealed in Figure 3-5. The radius and thickness parameters in the four planes perpendicular to the axis of the LV were computed as the average of corresponding parameters of short-axis slices that were within half the axial distance between adjacent planes. Due to difficulties in fitting slices in the apical and apex region, the initial wall thickness on the axis was fixed at 7.0mm . The endo- and epi-cardial radii along the 45° line were estimated assuming that the apical dome had a half-ellipsoidal geometry. The two ellipsoids for the endocardium and epicardium were both centered at the dividing point between the cylindrical and spherical coordinates. Based on the estimated major and minor axis, the radii along the 45° line were derived using the equation in the figure. The difference of the estimated endo- and epi-cardial radii yielded the corresponding initial wall thickness parameters. The initial myocardial activities were assumed to be homogeneous and the segmental parameters were computed by averaging all the segmental parameters from the mid-cavity slices. The initial concentration parameters of the blood pool and background were estimated similarly by averaging the values from the mid-cavity slices.

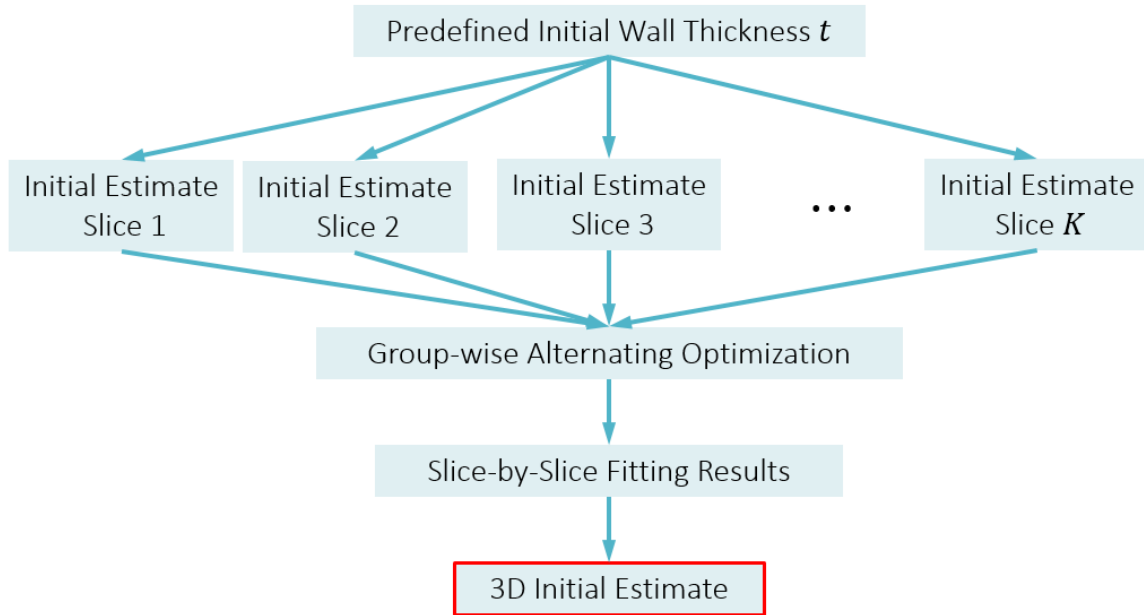


Figure 3-4. Illustration of generating a 3D initial estimate for a predefined initial wall thickness.

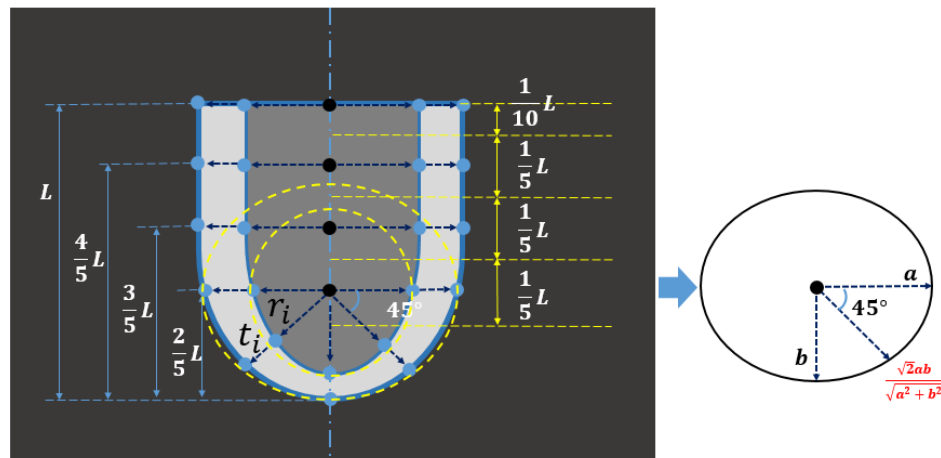


Figure 3-5. Illustration of combining slice-by-slice fitting results into initial optimization parameters for fully 3D fitting.

Based on the eleven values of the wall thickness, eleven sets of initial 3D model parameters were generated using the above method. The optimized set of model parameters resulting in the smallest value of the objective function were regarded as the global optimum of fully 3D fitting.

Figure 3-6 shows the procedure of the proposed group-wise alternating optimization scheme.

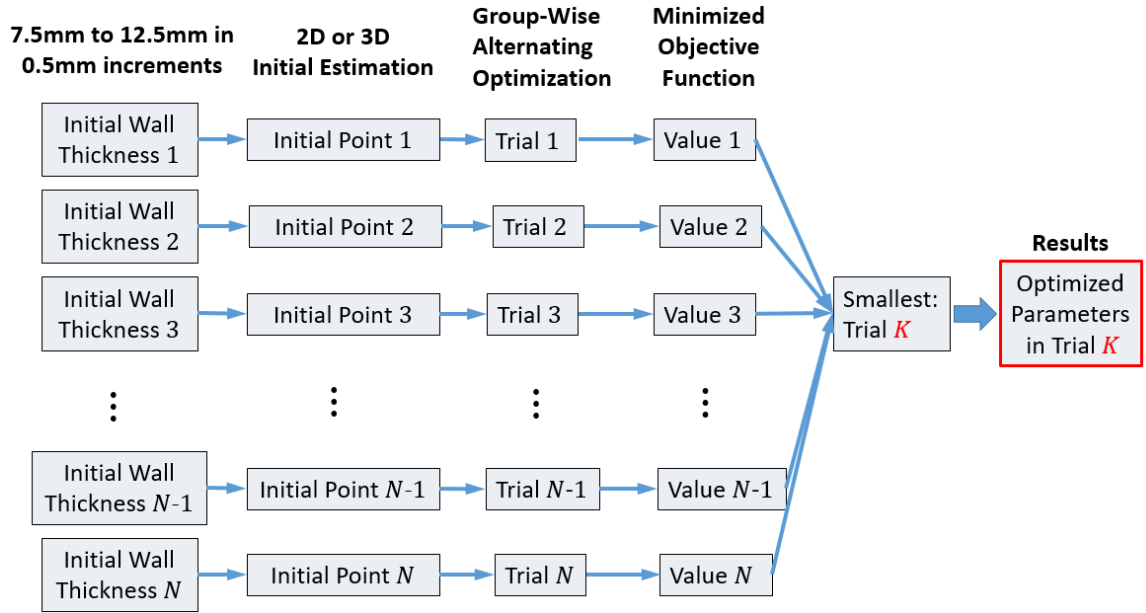


Figure 3-6. The procedure of the group-wise alternating optimization scheme.

3.6 Evaluation

The proposed method was applied to analytically simulated myocardial perfusion SPECT images, where the ground truth of the geometry and activity parameter values were known. We simulated both 2D short-axis slices and full 3D transaxial images. The proposed method was evaluated by computing the difference between the estimated model parameters with the truth. It was also evaluated by interpreting the estimated model parameters from the perspective of left ventricle segmentation, mid-myocardial surface estimation, and partial volume compensation. The details will be discussed in the following.

3.6.1 2D Simulation

The phantom image was a 144×144 short-axis image of $1mm^2$ pixel size. The LV geometry was extracted from the XCAT phantom in order to model realistically myocardial shape. The background and blood pool had homogeneous activity concentrations. The myocardium was

nonuniform with a perfusion defect having a 45° angular extent and 50% severity (i.e., reduction in activity concentration relative to normal myocardium). The defect in the anteroseptal direction overlapped with one segment of the proposed 8-segment activity distribution model. The relative activity concentrations were defined as follows: blood pool=15, background=5, normal myocardium=95, perfusion defect=45. The phantom image is shown in Figure 3-3a.

Projection data were generated using an in-house projection code (Frey, Ju et al. 1993). The gamma camera rotated around the center of the phantom image (radius of rotation=26 cm) to acquire data at 128 views over 360° . The distance-dependent collimator-detector response was modeled, but attenuation and scatter were not. The noise-free projections were contaminated by uncorrelated Poisson noise using a Poisson-distributed pseudorandom number generator to generate multiple noisy datasets. Two noise datasets were simulated by differently scaling the data prior to contamination. The standard noise data was scaled to approximately match the counts in an ungated short-axis image of clinical myocardial perfusion SPECT. The higher noise data had only 10% counts of the standard data in order to simulate the effects of applying the method to a gated image with ~ 8 gates per cardiac cycle.

For linear reconstruction, we used the implementation of FBP *iradon* in MATLAB with a Hamming filter (cutoff frequency=0.25 cycles/pixel). For iterative non-linear reconstruction, we used an in-house OS-EM software (8 subsets, 3 iterations) (Hudson and Larkin 1994; Frey and Tsui 2006).

Figure 3-7 displays the phantom image, the projection data, and the reconstructed noise-free and noisy images. Figure 3-8 plots the circumferential profiles for quantitative comparison. Each one evenly sampled the myocardium with 64 radial profiles from the center and the value was computed as the average along the true wall thickness. Generally, the myocardial activity concentration was underestimated due to PVE. The spatial resolution was better with OS-EM than FBP, as indicated by the noise-free profile closer to the truth. The noise textures were distinct and the resulting

myocardium concentration fluctuation with OS-EM was more dramatic, especially at the higher noise level. Consequently, the defect was barely visually detectable.

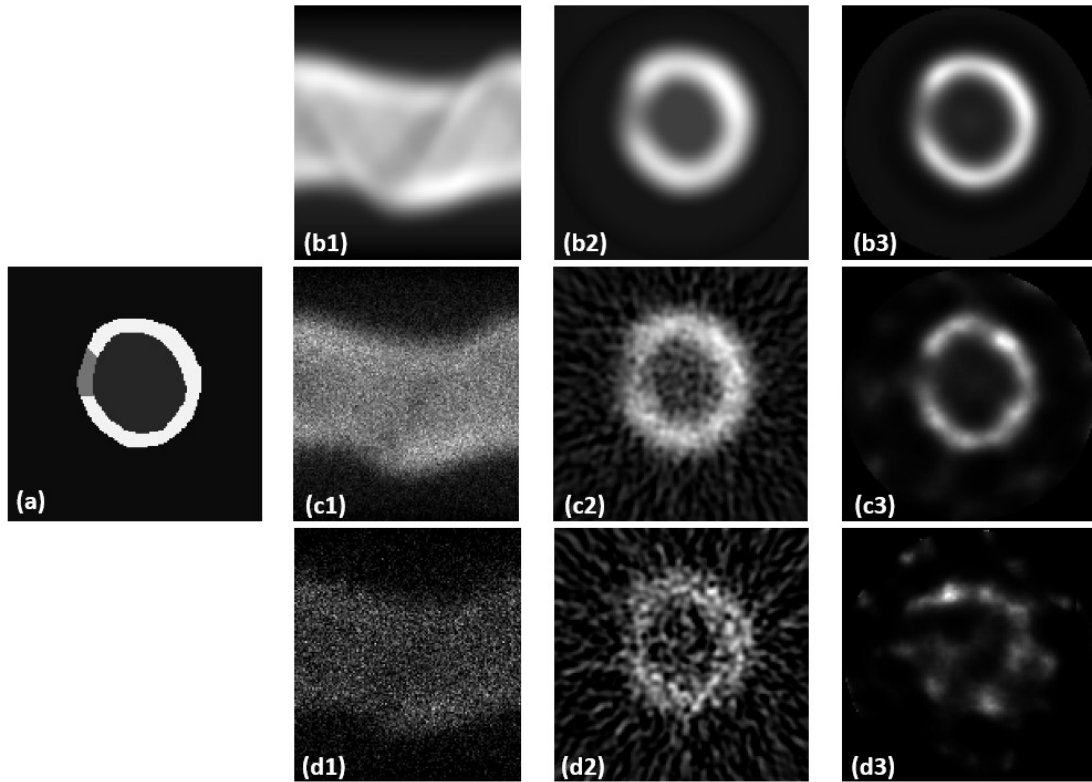


Figure 3-7. Myocardial perfusion SPECT simulation of short-axis slices: (a) the phantom image; (b) noise-free data; (c) standard noise data; (d) high noise data, containing 10% counts of the standard data. Each dataset consists of three images: from left to right, the sinogram and the FBP and OS-EM reconstructions. The negative values were set to zero in the display.

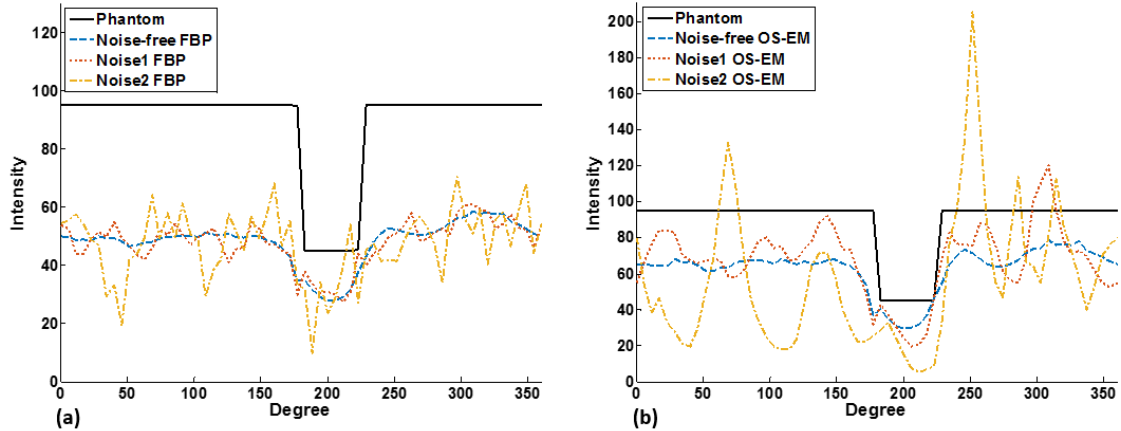


Figure 3-8. Circumferential profiles of simulated short-axis images: (a) FBP reconstruction; (b) OS-EM reconstruction.

3.6.2 3D Simulation

The XCAT-based phantom consisted of 120 transaxial slices that covered the cardiac region. Each slice was a 512×512 image with a 1 mm^3 voxel size. The background and blood pool had homogeneous activity concentrations. The myocardium was nonuniform with a perfusion defect having 50° angular extension, 20mm axial length, and 50% severity. It approximately overlapped with the mid-inferolateral segment in standardized 17-segment model. The relative regional activity concentrations remained unchanged from the 2D simulation: normal myocardium=95, perfusion defect=45, blood pool=15 and background=5.

In the 2D simulation, the gamma camera rotated around the LV axis to acquire the projections, which, however, was not correct in practice. In the 3D simulation, the camera rotated around the body axis to acquire 128 projections over 360° from the transaxial phantom. This results in a more realistic asymmetric and spatially varying reconstructed PSF. Since the proposed method only attempted to compensate for PVEs, the imaging process modeled collimator-detector response but not photon attenuation or scatter. Similarly, the noise-free projection dataset was contaminated by uncorrelated Poisson noise.

The 3D volume was FBP reconstructed using a series of 2D reconstructions of the transaxial slices, with the aid of function *iradon* in MATLAB (Hamming filter, cutoff frequency=0.25 cycles/pixel). The volume was then manually reoriented and truncated into a 128×128×128 matrix to generate short-axis, vertical long-axis, and horizontal long-axis slices, as shown in Figure 3-9. The perfusion images were also synthesized into polar maps, which used 64 sampling radial profiles in each short-axis slice and extracted the maximal intensity along each profile. Figure 3-10 displays the polar maps and their main diagonal profiles.

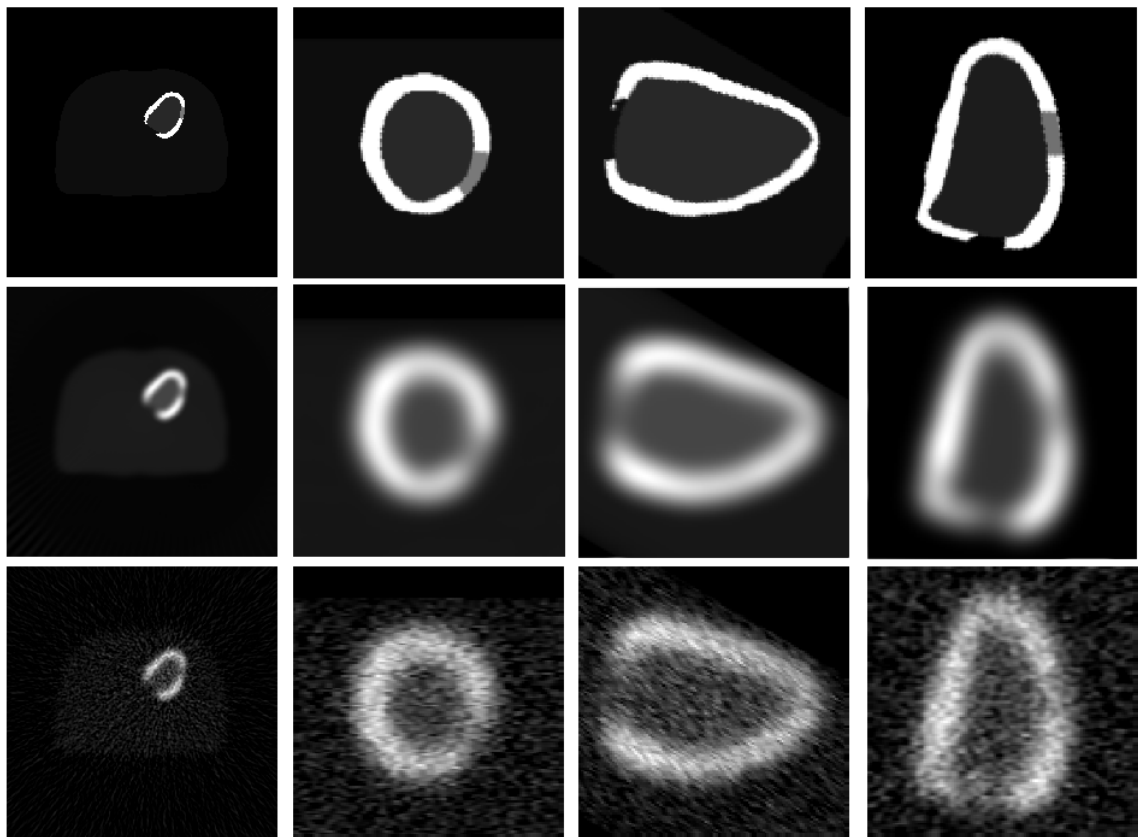


Figure 3-9. Myocardial perfusion SPECT simulation of a 3D transaxial phantom. From top to bottom: the phantom, noise-free data, noisy data. From left to right: a transaxial slice, a short-axis slice, a vertical long-axis slice, a horizontal long-axis slice. The negative values were set to zero in the display.

The noise texture in the reoriented slices was different from that in the transaxial slices. Since the image was independently reconstructed on the basis of transaxial slices, the blurring in

FBP yielded more noise correlation within the transaxial slice than between the slices. In addition, some regions with zero intensity were noticeable in the example short-axis and vertical long-axis slices. They corresponded to the outside of the body and were introduced during reorientation and truncation. The mismatch with the homogeneous background assumption was eliminated by restricting the model fitting to smaller ROI that excluded these voxels.

In the reconstructed images or the associated polar maps, a region of reduced uptake, mimicking a perfusion defect, was visible at the apex. This artifact was due to PVEs combined with the relatively thinner myocardium at the apex, as shown in the example vertical long-axis slice of the phantom image. PVE also resulted in marked underestimation of the absolute uptake in the myocardium.

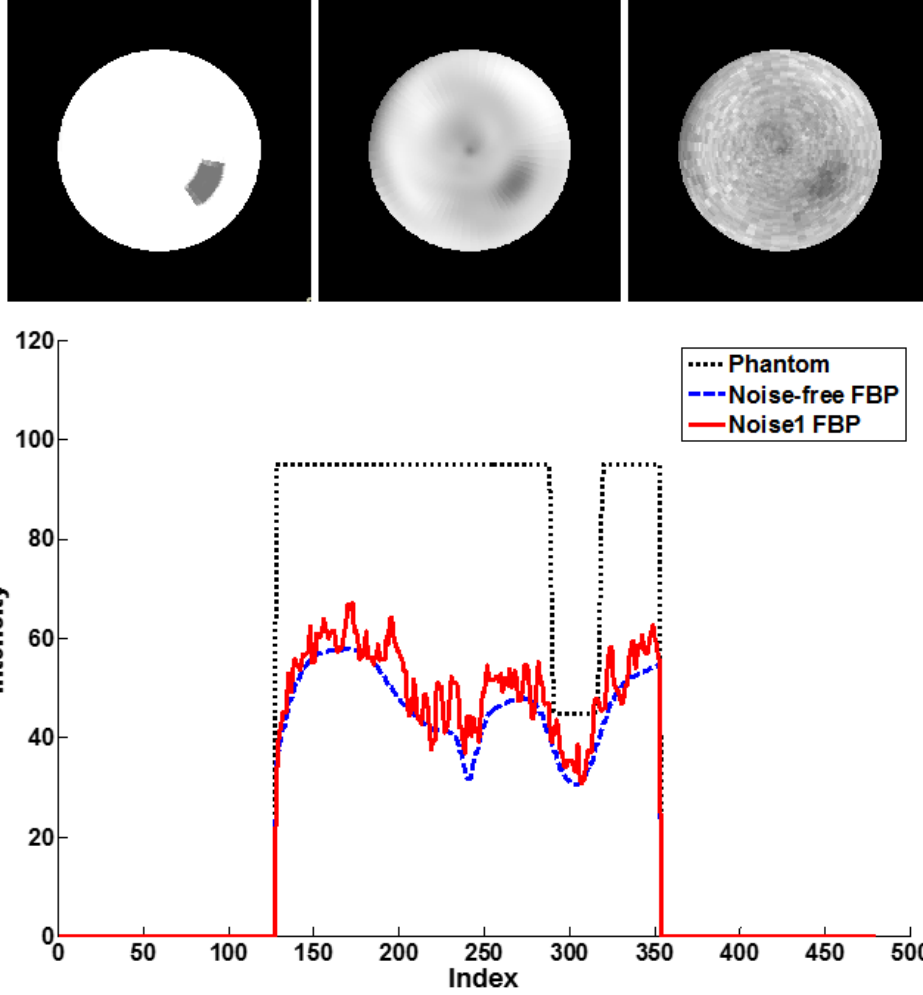


Figure 3-10. Main diagonal profiles of the polar maps corresponding to the phantom, noise-free and two noisy images.

3.6.3 Errors of Parameter Estimation

To directly evaluate the estimation, the difference between the estimated model parameters and the underlying truth were calculated, which is named the average of root mean square error ($\mu RMSE$) over the sampling rays or the myocardial segments. The $\mu RMSE$ expressions for endocardial radius r_i , wall thickness t_i and myocardial activity concentration a_i are listed below.

$$\mu RMSE(r) = \frac{1}{N_r} \sum_{i=1}^{N_r} \sqrt{\frac{1}{N_{noise}} \sum_{n=1}^{N_{noise}} (r_i^{(n)} - R_i)^2}$$

$$\mu RMSE(t) = \frac{1}{N_r} \sum_{i=1}^{N_{rad}} \sqrt{\frac{1}{N_{noise}} \sum_{n=1}^{N_{noise}} (t_i^{(n)} - T_i)^2}$$

$$\mu RMSE(a) = \frac{1}{N_s} \sum_{j=1}^{N_s} \sqrt{\frac{1}{N_{noise}} \sum_{n=1}^{N_{noise}} (a_j^{(n)} - A_j)^2}$$

N_r , N_s and N_{noise} denote the number of sampling rays, the number of myocardial segments and the number of noise realizations. R_i , T_i and A_j represent the corresponding true values of ray i and myocardial segment j .

3.6.4 Efficacy of Left Ventricle Segmentation

The proposed model-based reconstruction can be viewed as a segmentation method. The estimated geometry model parameters can be indirectly evaluated by comparing the resulting myocardium mask (M_1) with the true mask (M_2). Their overlap is quantified with Dice similarity coefficient (DSC) (Zou, Warfield et al. 2004):

$$DSC = \frac{|M_1 \cap M_2|}{(|M_1| + |M_2|)/2}.$$

The numerator denotes the number of shared myocardial pixels while the denominator calculates the average number of myocardium pixels.

The proposed method was also compared to simple thresholding with respect to the accuracy of myocardium segmentation. The thresholding method first smoothed the reconstructed noisy image using a Gaussian low-pass filter. Those pixels with values greater than a predefined threshold were assumed to represent the myocardium. The standard deviation of the Gaussian filter and the threshold were selected to maximize the average DSC over all noise realizations.

3.6.5 Efficacy of Mid-Myocardial Surface Estimation

The proposed method can also be used to estimate the mid-myocardial surface. Along each ray in the geometry model, the mid-myocardial point is computed as the endocardial radius plus half the thickness parameter. As revealed in Chapter 4, the relatively small wall thickness cannot be reliably determined from myocardial perfusion SPECT and PET images due to the poor spatial resolution. Consequently, the endocardial and epicardial surfaces cannot be precisely estimated, either. In contrast, the estimation of the mid-myocardial surface is more robust to poor resolution and noise statistics. Therefore, the resulting mid-myocardial surfaces from different gating frames might be useful in improving the assessment of wall motion. For evaluation, the proposed method was compared to three related methods in the literature.

The RadialCOM method statistically estimated the mid-myocardial radii from resampled radial profiles originating from the long axis of the LV (Goris, Thompson et al. 1994). The mid-myocardial radius was calculated as the first moment of the count rate distribution, i.e., the center of mass of the count profile.

The MaxIntensity method estimated the mid-myocardial line from short-axis images assuming that the mid-myocardial points tended to have the maximum intensity along the resampled radial profile (Soneson, Ubachs et al. 2009). A geometric constraint was incorporated to penalize large variations between neighboring mid-myocardial radii.

The RadialFitting method was based on a model-based fitting of resampled radial profiles originating from the long axis of the LV (Dumouchel and deKemp 2011). Each profile was modeled using a 1D square wave function defined by five parameters: the endocardial radius, the wall thickness, and the activity concentrations in the blood pool, myocardium, and background. These model parameters were obtained by minimizing the LS difference between the profile and the convolution of the model function and the approximated system PSF. The mid-myocardial radius was estimated as the endocardial radius plus half the wall thickness.

3.6.6 Efficacy of Partial Volume Compensation

The proposed model-based reconstruction method can also be perceived as a PVC method. The resulting model images were compared to those obtained from two existing PVC methods.

One is a deconvolution-based method termed as reblurred Van Cittert iteration with total variation-based regularization to suppress noise amplification (Tohka and Reilhac 2008). It was based on the assumption of uncorrelated normal noise distribution in the reconstructed image. Just like the proposed method, it required no left ventricular ROIs but the system PSF, which was approximated using a spatially-invariant Gaussian kernel G_σ . However, the proposed method is expected to have superior performance due to the additional LV structural information included in the geometry model and the shape prior.

The objective function is formulated as follows:

$$\min_{f_P} \sum_x \|\mathbf{f}_o(x) - \mathbf{G}_\sigma * \mathbf{f}_P(x)\|^2 + \lambda_{TV} \sum_x |\nabla \mathbf{f}_P(x)|.$$

where $|\nabla \mathbf{f}_P(x)|$ was implemented as $\sqrt{|\nabla \mathbf{f}_P(x)|^2 + \varepsilon^2}$ to ensure differentiability, where ε was a small scalar and set as tenth of the mean of the absolute observed image intensities $|\mathbf{f}_o(x)|$.

The update equation is expressed as:

$$\mathbf{f}_P^{(n+1)}(x) = \mathbf{f}_P^{(n)}(x) + \alpha \left(\mathbf{G}_\sigma * (\mathbf{f}_o - \mathbf{G}_\sigma * \mathbf{f}_P^{(n)}) \right)(x) + \alpha \cdot \beta_{TV} \operatorname{div} \frac{\nabla \mathbf{f}_P^{(n)}(x)}{\sqrt{|\nabla \mathbf{f}_P^{(n)}(x)|^2 + \varepsilon^2}}$$

where step length $\alpha=1.5$, regularization parameter $\beta_{TV}=0.25$, the same as in the original article.

The iteration number n was chosen to minimize $\mu RMSE$ of myocardial segmental activities of the resulting PVE-compensated images.

The other one is an ROI-based PVC method that required both the system resolution modeling and the delineated blood pool, myocardium and background ROIs (Du, Madar et al. 2013). The iterative compensation was described using:

$$f_{myo}^{(n+1)} = \frac{f_{myo}^{(0)} - (f_{bp}^{(n)} * G_{\sigma} + f_{bkg}^{(n)} * G_{\sigma})m_{myo}}{m_{myo} * G_{\sigma}}$$

$$f_{bp}^{(n+1)} = \frac{f_{bp}^{(0)} - (f_{myo}^{(n+1)} * G_{\sigma} + f_{bkg}^{(n)} * G_{\sigma})m_{bp}}{m_{bp} * G_{\sigma}}$$

$$f_{bkg}^{(n+1)} = f_{bkg}^{(0)} - (f_{myo}^{(n+1)} * G_{\sigma} + f_{bp}^{(n+1)} * G_{\sigma})m_{bkg}.$$

In these equations, $f_{myo}^{(n)}$, $f_{bp}^{(n)}$ and $f_{bkg}^{(n)}$ represent the regional image of left ventricular myocardium, blood pool and the rest of the image, respectively. The superscript denotes the number of iterations (0 means no compensation). m_{myo} , m_{bp} and m_{bkg} denote the corresponding binary ROI images for each region. Typically, accurate ROIs were obtained from registered high-resolution anatomical images; for comparison, we also used approximate ROIs derived from the estimated geometry model parameters.

Our interest focused on PVE compensated myocardial activities. In the first equation, the numerator attempts to remove the spill-in activity from the blood pool and the background while the denominator calculates the recovery coefficients to compensate for the spill-out. The process was repeated until convergence. It took six iterations to yield sufficiently small difference between consecutive iterations.

4. Results and Discussion (2D): Global Optimization

To gain insights into the properties of the proposed method, it is necessary to systematically characterize the LV geometry and activity distribution models, resolution and noise modeling of the imaging and reconstruction process, and the shape prior. Without losing generality, the method was applied to simulated short-axis images for improved efficiency.

It is critical that the objective function is actually optimized to achieve the global minimum; otherwise, all the derived conclusions cannot be well justified. Therefore, the MultiStart method was employed in this chapter regardless of its high computation intensity. It used 1000 random trials of initial points around the underlying truth. Each activity concentration parameter was uniformly sampled in the $\pm 20\%$ interval of the truth. Each endocardial radius was also uniformly sampled in an interval centered at the truth with the interval size equal to the corresponding true wall thickness. The initial wall thickness was indirectly obtained as the difference between the endocardial radius and the epicardial radius, which was analogously sampled from the same-size interval centered at the epicardium position.

4.1 Geometry Model

It is interesting to quantify the ability of the proposed geometry model in describing realistic LV structures in short-axis slices. To investigate this, three short-axis myocardium mask images representing different LV shapes were extracted from the XCAT phantom. For each XCAT-based mask image, its LS difference with the mask image generated from the geometry model was minimized by optimizing the model parameters. Different numbers (6, 8, 16, and 32) of radii were used to sample the donut-like shape. The myocardium masks resulting from the optimized model parameters were evaluated in terms of DSC with the truth, as shown in Figure 4-1. In the three cases, the DSC monotonically increased with more radii. The smallest DSC was more than 93% even with only six profiles, which demonstrated the effectiveness of the model. It also implies that

the model has the capability to describe realistic endocardial and epicardial contours when the number of radii is sufficiently large. However, more radii indicate more model parameters to be estimated, leading to the higher computational intensity of optimizing these model parameters and higher sensitivity to image noise. The number of radii should be chosen to strike a balance between accuracy and efficiency. Therefore, the short-axis geometry model used 8 radii in the following studies.

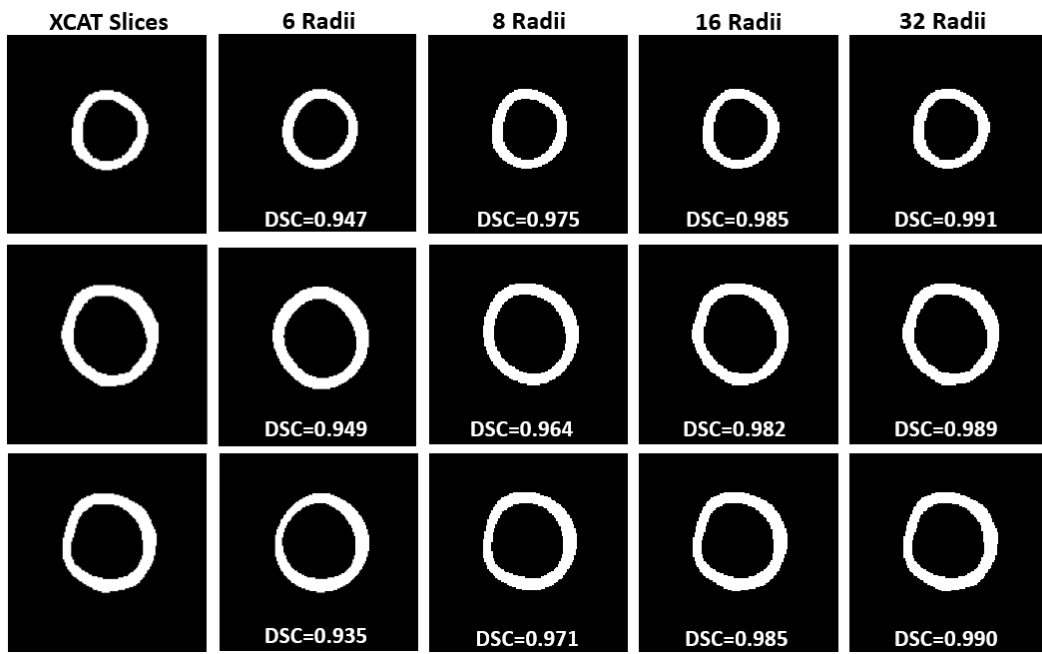


Figure 4-1. Fitting the geometry model to XCAT short-axis myocardium masks with different numbers of radii.

4.2 Activity Distribution Model

The 2D phantom image, which was defined using 8 myocardial segments, was fitted with the activity distribution model of 6, 8 and 12 myocardial segments in the short-axis slice, respectively. The LS difference between the phantom image and the image generated from the object model (8 radii in the geometry model) was minimized by optimizing the model parameters. The optimized model images and the corresponding myocardial circumferential profiles are displayed in Figure 4-

2. It is evident that model mismatch can result in approximated quantification of defect extent and severity. With the proposed activity distribution model, the defect extent can only be measured in increments of the segment size. If the location and size of the defect do not exactly match one or more myocardial segments in the model, the defect severity will never be accurately estimated and could confound diagnosis. However, this inaccuracy should be compared to what can be accomplished with the raw perfusion images and PVC compensation methods.

The mismatch would be difficult to avoid in practice because no prior knowledge about defect is available, even from high-resolution anatomical images, to accurately configure the activity distribution model. To reduce the adverse impact, one approach is to decrease the segment size, or equivalently increase the number of segments, in an effort to confine the approximation to a relatively smaller region. Alternatively, an additional variable, which defines the angular position of segments, can be introduced to eliminate the location mismatch. In both cases, the improved ability to model defect would be achieved at the expense of increased model complexity and likely greater uncertainty in the values of the estimated parameters.

In the following studies, we did not consider mismatch between the activity distribution model and the phantom image. The 8-segment model was used such that the defected region overlapped with one myocardial segment. The resulting model image (Figure 2c) was regarded as the ground truth. Note that the geometry model using 8 radii included a small mismatch with the phantom, as indicated by the smoother endocardial and epicardial contours. Since the geometry mode and the activity distribution model are closely related to each other in determining the model image, there was also a slight difference between the corresponding myocardial circumferential profiles of the phantom and the 8-segment image.

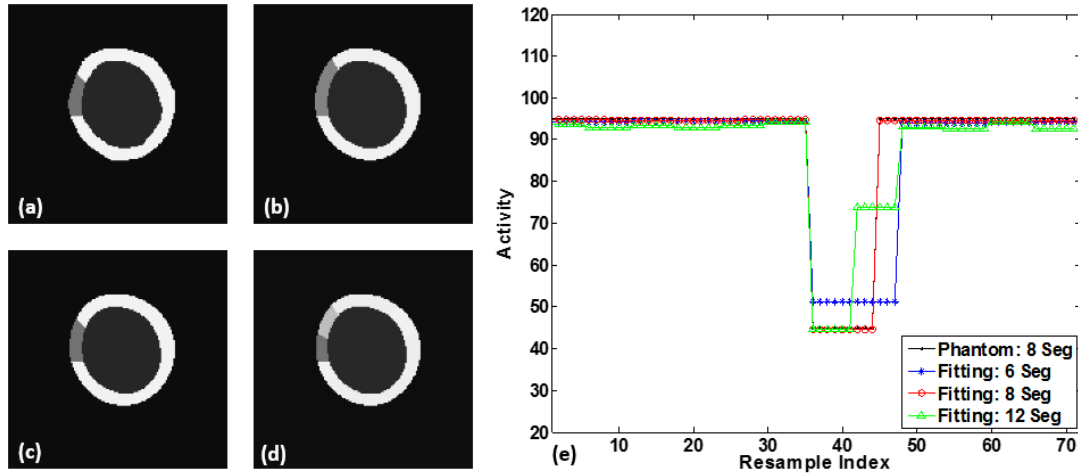


Figure 4-2. Fitting the activity distribution model to the short-axis phantom image using different numbers of myocardial segments. (a) The phantom image; (b)-(d) Optimized model images using 6, 8 and 12 myocardial segments; (e) Resampled myocardial circumferential profiles.

4.3 Resolution Model

To improve computational efficiency, one implementation of the proposed method approximates the modeling of resolution in the reconstructed image domain using a spatially invariant Gaussian kernel, which was derived by minimizing the LS difference between a noise-free reconstruction and the Gaussian-blurred phantom image within the inscribed circular ROI of the images. The fitted standard deviation was $\sigma = 6.04\text{mm}$ (FWHM=14.23mm) for FBP reconstruction, which used a Hamming filter with the cutoff frequency=0.25 cycles/pixel, and $\sigma = 3.84\text{mm}$ (FWHM=9.04 mm) for OS-EM reconstruction (8 subsets, 3 iterations), which only modeled the collimator-detector response and did not use any post-reconstruction filtering.

Figure 4-3 qualitatively and quantitatively demonstrates the validity of the resolution approximation for FBP and OS-EM reconstructions. It is difficult to visually distinguish the blurred images obtained with the true and approximate models. But the difference images exhibited some differences of the two resolution models. The RMSE within the ROI was 0.99 for FBP and 2.26 for OS-EM. In addition, the profiles overlap almost entirely for FBP, while the profile difference

for OS-EM reconstruction was slightly larger especially in the blood pool. These observations indicate that the Gaussian kernel more accurately modeled the resolution for FBP than for OS-EM.

The effects of approximated resolution modeling on estimated values of the geometry and activity distribution (i.e., the complete model of the myocardium) model parameters were also evaluated by LS fitting the blurred myocardial model image to the noise-free reconstruction. The fitting included the uniform thickness prior with a regularization parameter $\beta = 0.1$. The FWHMs of fitted Gaussian kernels was deliberately perturbed in both directions to examine the influence of errors in resolution modeling. Figure 4-4 visually compares the estimated endocardial radius, wall thickness and myocardial activity parameters. Table 4-1 shows the averaged parameters over radii or segments along with the percentage errors.

The fitted Gaussian resolution resulted in the underestimation of the average endocardial radius by 3.59% for FBP and 6.45% for OS-EM. Due to the relatively small wall thickness, the average value was overestimated by 18.22% for FBP and 23.71% for OS-EM with 1.5~2.0mm biases. The smaller errors for FBP than OS-EM agreed with the results in Figure 4-3. However, the underestimation error of the average myocardial activity concentration was smaller for OS-EM (4.47%) than FBP (7.14%). This mainly results from the better resolution in OS-EM than FBP. Note that the errors resulting from the approximate resolution were relatively larger for the wall thickness. The errors were expected to be reduced with more realistic 3D simulation.

When a smaller FWHM was used during model fitting, the estimated myocardium had a larger size and lower concentration to compensate for the reduced system blurring; the biases were the opposite when a larger FWHM was used. For FBP, accurate resolution modeling using forward projection and reconstruction was also incorporated as a criterion. The results were the closest to the phantom fitting reference but did not exactly match. The small differences can be attributed to the bias in the shape prior, or that the optimization might fail to achieve the global minimum. These results imply the significance of resolution modeling in improving estimation accuracy.

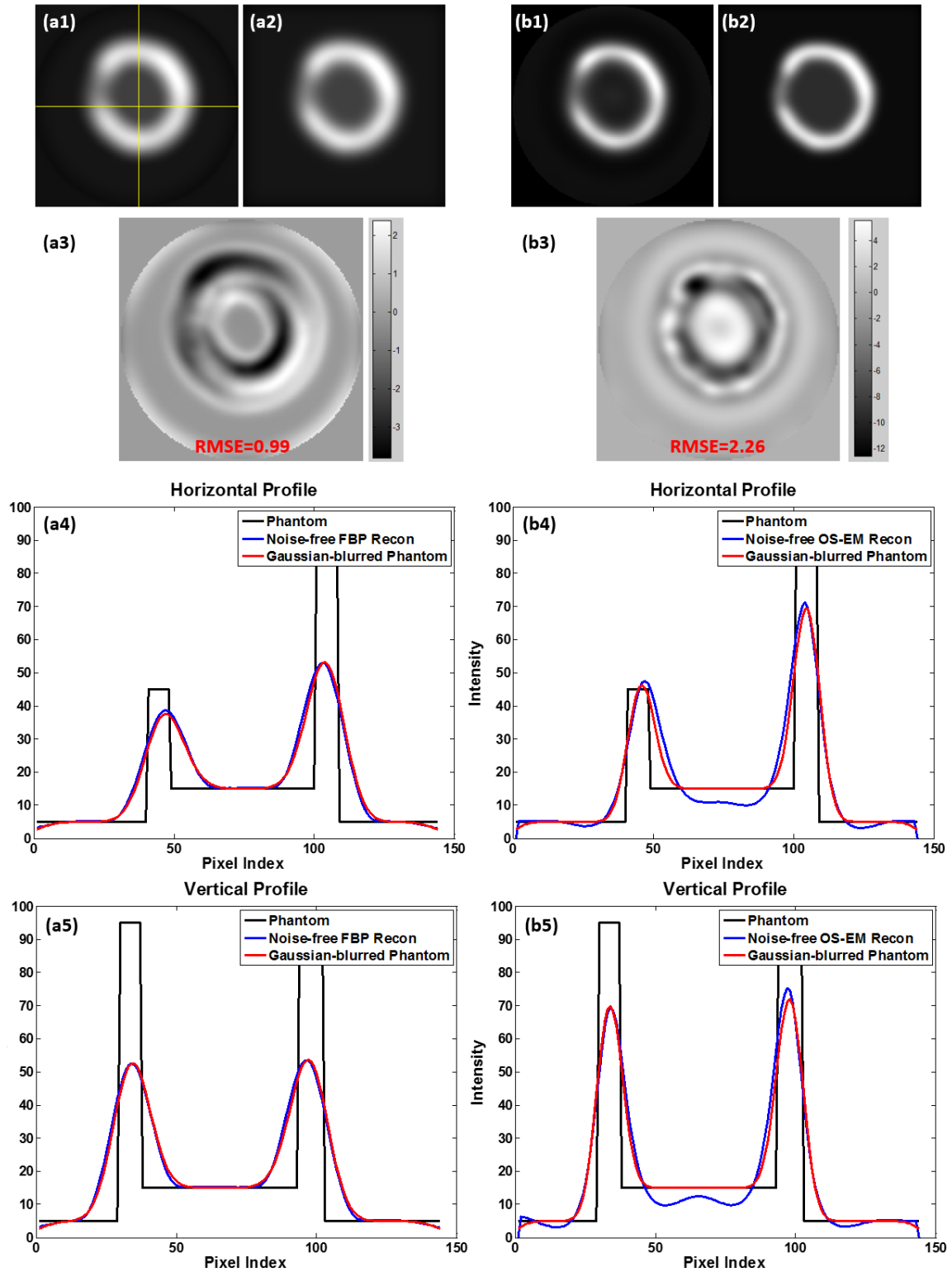


Figure 4-3. Approximated resolution modeling in FBP and OS-EM reconstruction using spatially invariant Gaussian kernels. (a) FBP; (b) OS-EM; (1) Noise-free reconstruction; (2) Gaussian-blurred phantom image; (3) The difference image of (1) and (2); (4) Central horizontal profiles; (5) Central vertical profiles.

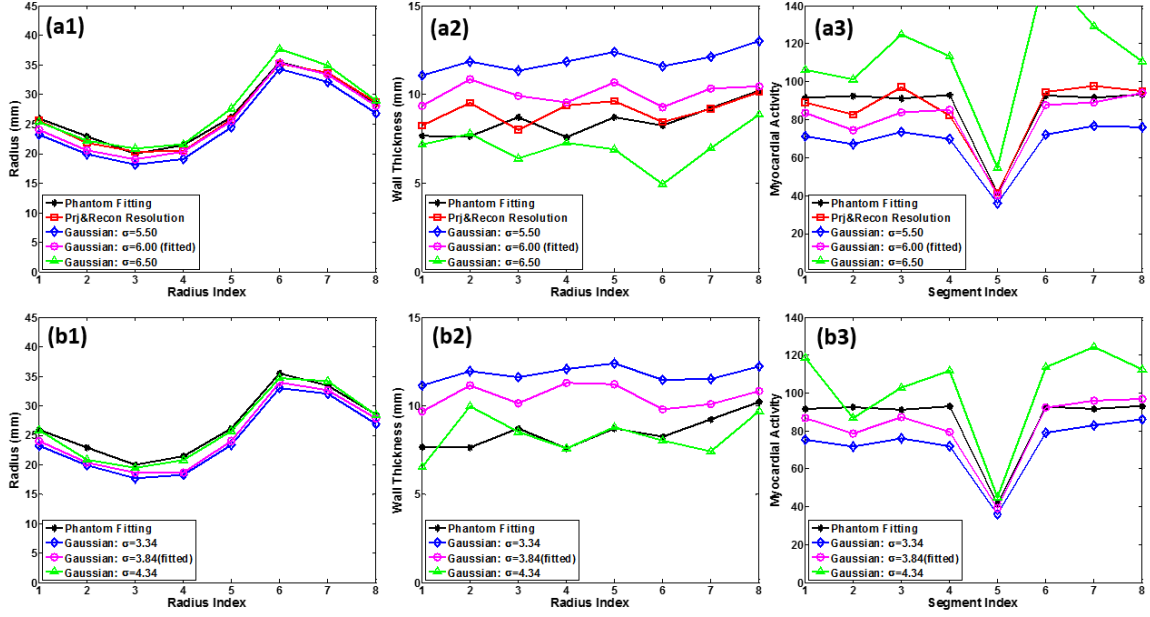


Figure 4-4. Estimated (1) endocardial radius, (2) wall thickness, and (3) myocardial segmental activities from (a) FBP and (b) OS-EM noise-free reconstruction with different fitting resolution models.

Table 4-1. The average values of endocardial radius, wall thickness, and myocardial activity parameters over radii or segments in Figure 4-4, along with the percentage errors with respect to the phantom fitting reference.

		Endocardial Radius r_i (mm)	Wall Thickness t_i (mm)	Myocardial Activity a_i
Phantom Fitting Reference		26.72	8.50	85.93
FBP	Prj & Recon Resolution	26.40 (-1.16%)	9.06 (6.64%)	84.98 (-1.11%)
	Gaussian: $\sigma = 5.50$	24.74 (-7.39%)	11.90 (39.99%)	67.83 (-21.06%)
	Gaussian: $\sigma = 6.00$ (fitted)	25.76 (-3.59%)	10.05 (18.22%)	79.79 (-7.14%)
	Gaussian: $\sigma = 6.50$	27.37 (2.46%)	7.03 (-17.25%)	112.33 (30.73%)
OS-EM	Gaussian: $\sigma = 3.34$	24.28 (-9.12%)	11.79 (38.75%)	72.42 (-15.71%)
	Gaussian: $\sigma = 3.84$ (fitted)	24.99 (-6.45%)	10.52 (23.71%)	82.08 (-4.47%)
	Gaussian: $\sigma = 4.34$	26.23 (-1.83%)	8.32 (-2.14%)	101.88 (18.57%)

4.4 Noise Model

4.4.1 FBP reconstruction

As discussed in Chapter 3, in the image-domain implementation of the ML estimation of the myocardial model parameters, the noise statistics of the pixels in FBP reconstructed images were assumed to follow an identical uncorrelated normal distribution. In other words, pixel variances

were uniform across the image and the correlation between pixels were zero. We assess the validity of this assumption in the following.

The variance image was numerically computed based on 10000 noise realizations. It was also theoretically derived based on the noise-free projection and the reconstruction matrix (Wilson 1994). The results are compared to the noise-free reconstruction in Figure 4-5. The two variance images agreed well with each other. They resembled a heavily smoothed version of the noise-free reconstruction. The standard deviations of the pixel variance in the myocardium, the blood pool, the background and the circular ROI were 1.53, 1.16, 3.31 and 5.20, respectively. Although the pixel variances were not strictly equal, the variations between pixels were much smaller than in the activity image, implying the reasonability of the equal variance assumption.

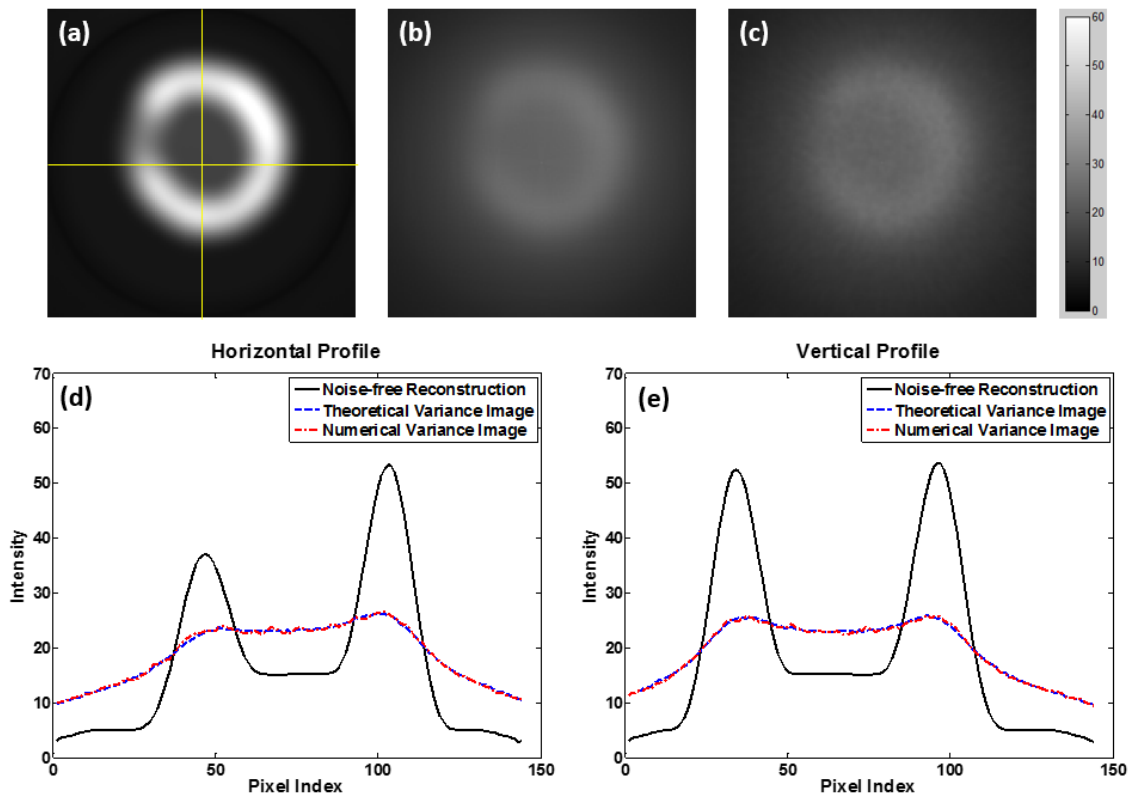


Figure 4-5. Evaluation of the variance images of FBP reconstruction. (a) Noise-free FBP reconstruction; (b) Theoretically calculated variance image; (c) Numerically calculated variance image based on 10000 noise realizations; (d) Central horizontal profiles; (e) Central vertical profiles.

The correlation coefficient matrix of the central column of the image was numerically calculated and visualized from different views in Figure 4-6. The elements of the k th diagonal, where $k=0$ represents the main diagonal, represent the coefficients for a correlation distance k . As expected, the noise correlation decreased rapidly with distance. The correlation was less than 0.6 when the distance was greater than two pixels. However, the correlation was over 0.8 for adjacent pixels. The fact that this was neglected is likely to introduce estimation biases. Also, the correlation behaved differently in different regions, as shown in Figure 4-6d. It was approximately uniform within the myocardium and blood pool, and was somewhat larger in the background.

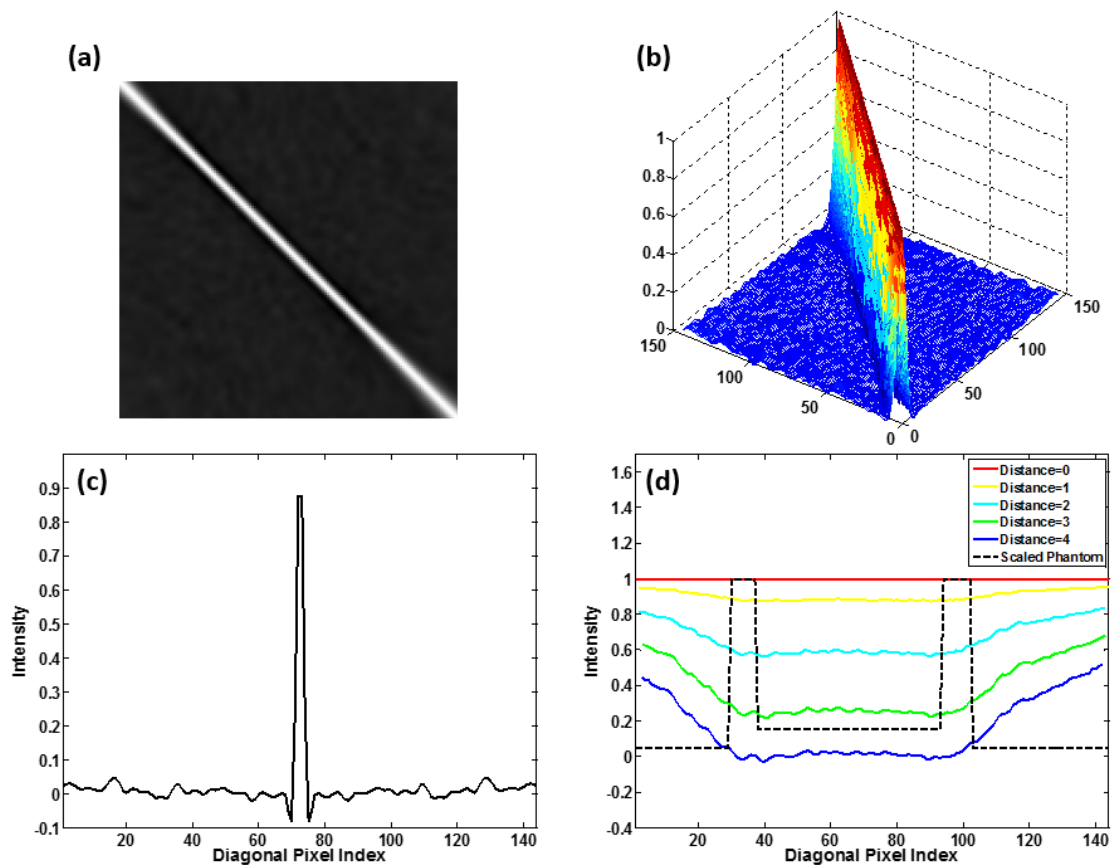


Figure 4-6. The correlation coefficient matrix of the central column of the FBP reconstructed image: (a) the image, (b) the mesh plot, (c) the antidiagonal profile, and (d) the diagonal profiles.

We also evaluated the impact of the noise approximation, which included the assumptions of the uniform variance and zero correlation between pixels, on estimated myocardial model parameters. The noise-free reconstruction and 50 noise realizations were fitted with the approximated Gaussian resolution kernel. The results are shown in Figure 4-7, where the error bars represent the standard deviations over noise realizations. The difference between the noise-free reconstruction fitting parameters and the mean parameters over noise realizations is associated with the estimation bias introduced by the noise model mismatch. The small difference demonstrates that the identical uncorrelated normal distribution is a good approximation of noise statistics in FBP reconstruction for the proposed model-fitting method.

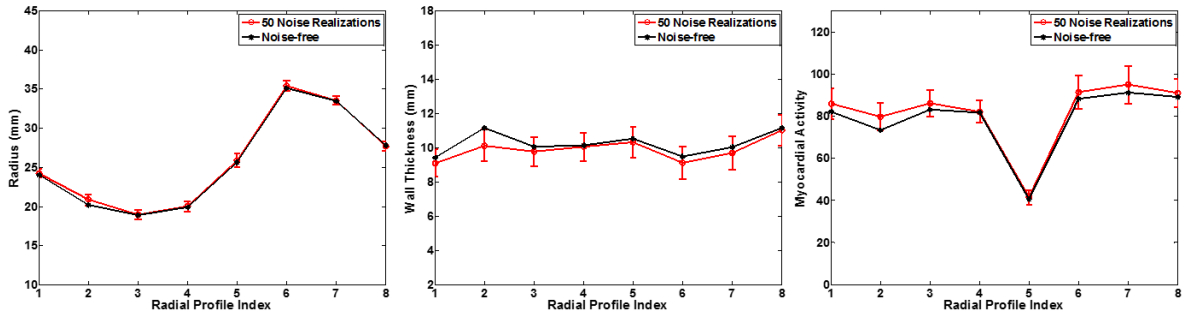


Figure 4-7. Comparison of estimated (a) endocardial radius, (b) wall thickness, and (c) myocardial segmental activity from the FBP noise-free reconstruction and 50 noise realizations using the approximated noise modeling.

4.4.2 OS-EM Reconstruction

The noise statistics in OS-EM reconstruction are approximately lognormal multivariate distributed, as discussed in Chapter 2. For simplicity, the proposed method assumes that the pixels follow uncorrelated normal distributions and that the pixel variance is proportional to the mean.

To evaluate the normal distribution approximation, four activity histograms were plotted for four pixels based on 1000 noise realizations using OS-EM reconstruction, each representing one of the four homogeneous activity regions (normal myocardium, defect, blood pool and background) in the phantom image. The settings of OS-EM reconstruction are given in Chapter 3. The histograms were then fitted using lognormal and normal distributions. The results are shown in Figure 4-8 and

the mean square errors (MSEs) of the fitting are listed in Table 4-2. The normal fitting was mildly inferior to the lognormal fitting in the normal myocardium and the perfusion defect, with the MSEs increased by 62.20% and 49.43%, respectively. However, it is evident that the lognormal fitting was more suitable in the blood pool and background, where the normal fitting increased the MSEs by 316.77% and 579.62%, respectively. Pixel values are non-negative in OS-EM reconstruction. With reduced tracer uptake, the histogram became increasingly asymmetric, resulting in the larger fitting errors with the normal distribution in corresponding regions. When applying the proposed method, in addition to masking out extra-cardiac regions (e.g., the liver) with high uptake, it might be helpful to constrain the model fitting in a tighter ROI around the LV, such that the smaller background might yield smaller estimation biases.

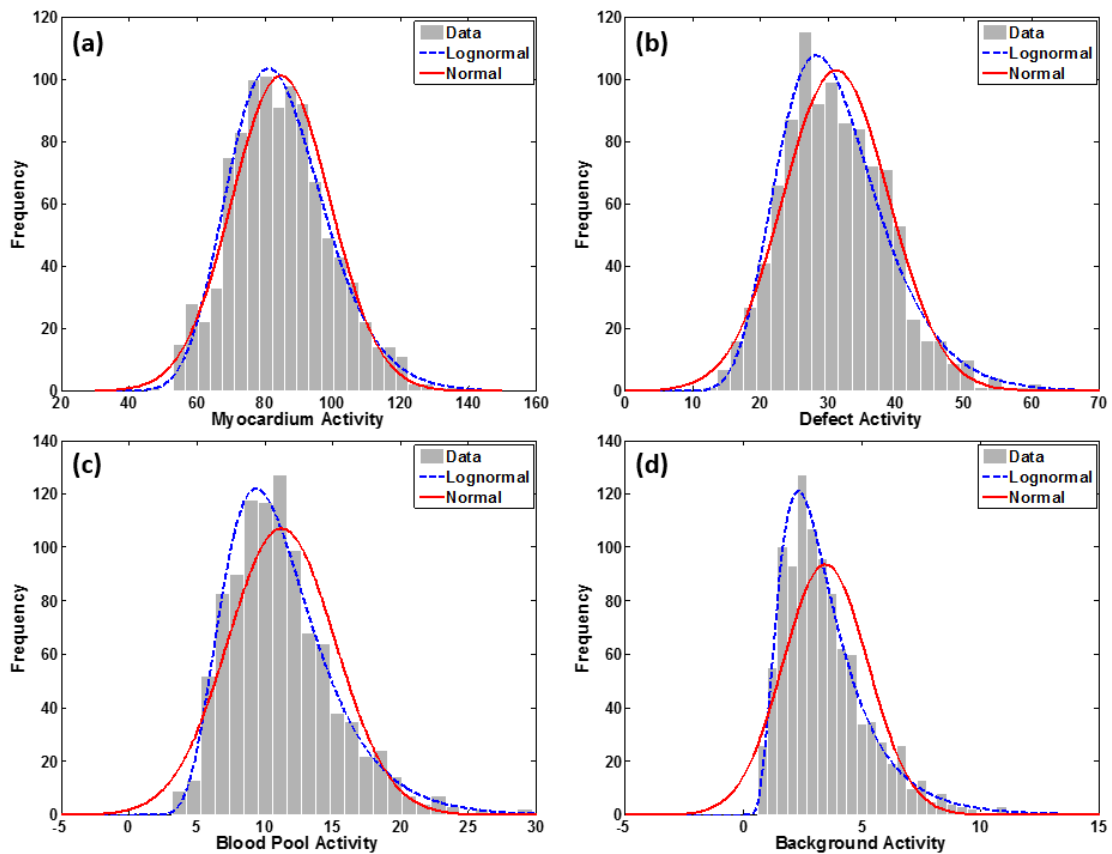


Figure 4-8 Fitting pixel intensity histograms based on 1000 OS-EM noise realizations using lognormal and normal distributions. The pixel is located in (a) the myocardium, (b) defect, (c) blood pool and (d) background, respectively.

Table 4-2. Mean square errors (MSE) of fitting the histograms using lognormal and normal distributions in Figure 4-8.

	Normal Myocardium	Perfusion Defect	Blood Pool	Background
Lognormal	36.01	52.22	41.63	45.05
Normal	58.41	78.03	173.50	306.17

To assess the assumption of zero noise correlation, the correlation coefficient matrix of the central column of the image was similarly calculated and visualized in Figure 9. The correlations roughly followed a sinc function as a function of correlation distance, similar to what was observed for FBP. However, the central peak was much wider, indicating that the pixel values were correlated for larger distances. Thus the approximation that the pixel values are uncorrelated is more valid for FBP than OS-EM reconstructions. Also, the region-dependent correlation exhibited different patterns from FBP. The correlations were relatively uniform in the blood pool and background and smaller in the myocardium than the previous two regions, as shown in Figure 4-9d.

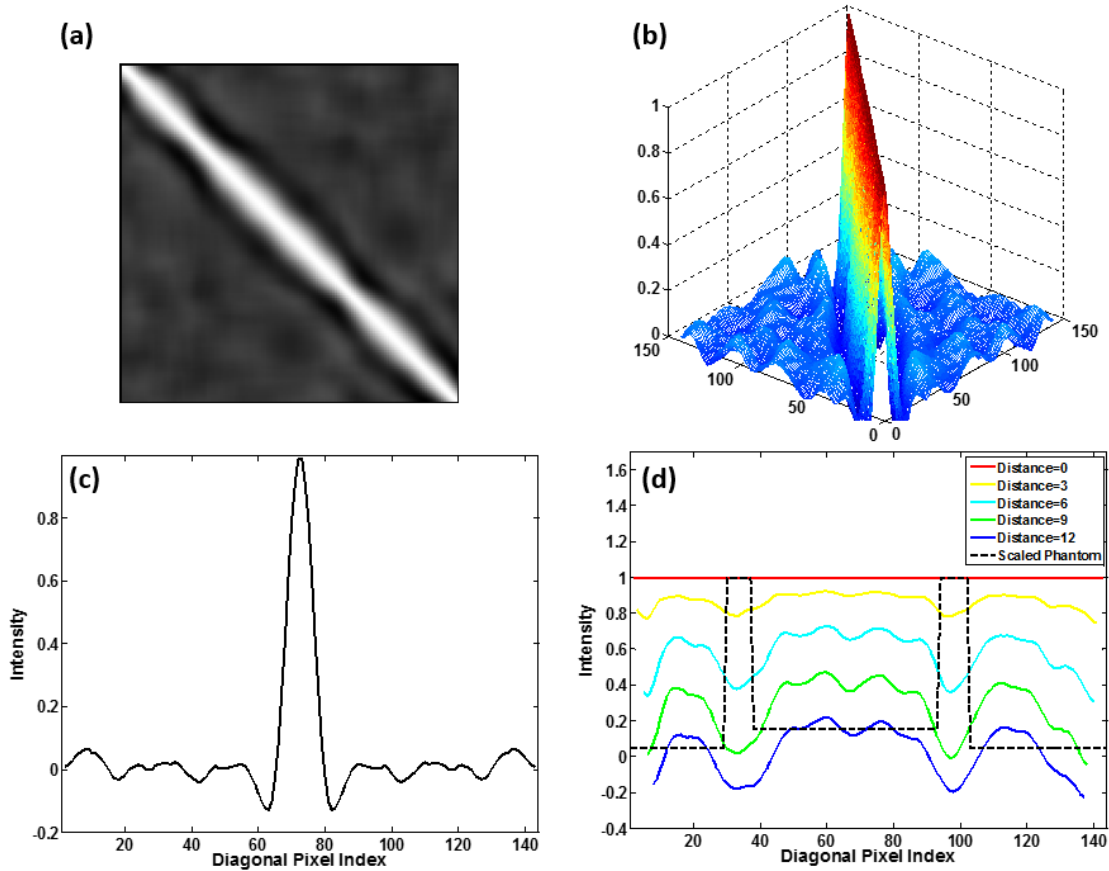


Figure 4-9. The correlation coefficient matrix of the central column of the OS-EM reconstructed image: (a) the image, (b) the mesh plot, (c) the antidiagonal profile, and (d) the diagonal profiles.

We also plotted the pixel variance as a function of mean in order to investigate the relationship, as shown in Figure 4-10. These data show clearly that the variance was not uniform and that thus WLS fitting is more appropriate for OS-EM reconstructed images.

The variance versus mean data were fitted with linear and quadratic functions, where the latter yielded a smaller error. The mean image can be approximated by the noisy reconstruction. Thus, if the relationship between mean and variance were available, the variance image could be derived to obtain the weighting coefficients. However, the fitting parameters are image dependent and estimating this relationship in practice would be computationally expensive and. If the variance is assumed to be proportional to the mean or the square of the mean, it would be unnecessary to

specify the exact parameters. Despite the smaller error with the quadratic fitting, it is better to assume a linear relationship between the variance and the mean for a number of reasons. First, the fitted quadratic coefficient was much smaller than the linear coefficient. In addition, the pixels where there was the largest deviation from the linear relationship were for small values of the mean, which corresponded to pixels in the background. The data points with the means larger than 30 were well approximated by a linear relationship. In the implementation, the impact of background pixels can thus be reduced by restricting the model fitting to a smaller ROI that includes less of the background region.

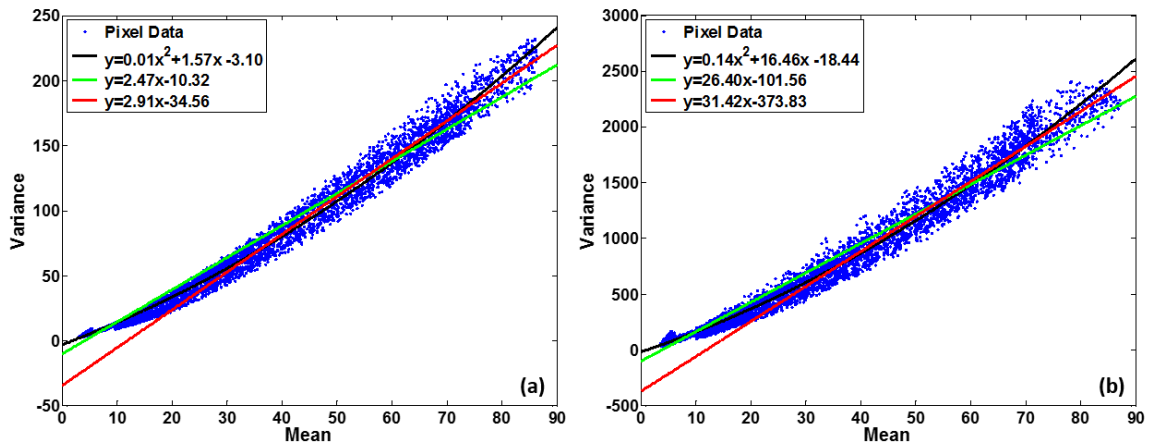


Figure 4-10. The pixel variance versus mean in based on 1000 OS-EM reconstructions at the two noise levels.

We also evaluated the effect of the approximated noise modeling on estimated model parameters, as shown in Figure 4-11. With the Gaussian resolution kernel, 50 noise realizations were processed using LS fitting and WLS fitting with two weighting schemes: one used the reciprocal of the square of the reconstructed noisy image, while the other used the reciprocal of the reconstructed image itself, corresponding to the assumption of a quadratic and linear relationship, respectively. The noise-free OS-EM reconstruction was also LS fitted for reference. Note that the shape prior was not included to allow a fair comparison of LS and WLS, because the weighting would alter the relative strengths of the data-fitting and regularization terms, making it difficult to select equivalent regularization parameters. The WLS with the linear weighting resulted in smaller

estimation errors than LS fitting. WLS fitting using the quadratic weighting, implying the reasonability of the noise modeling approximation.

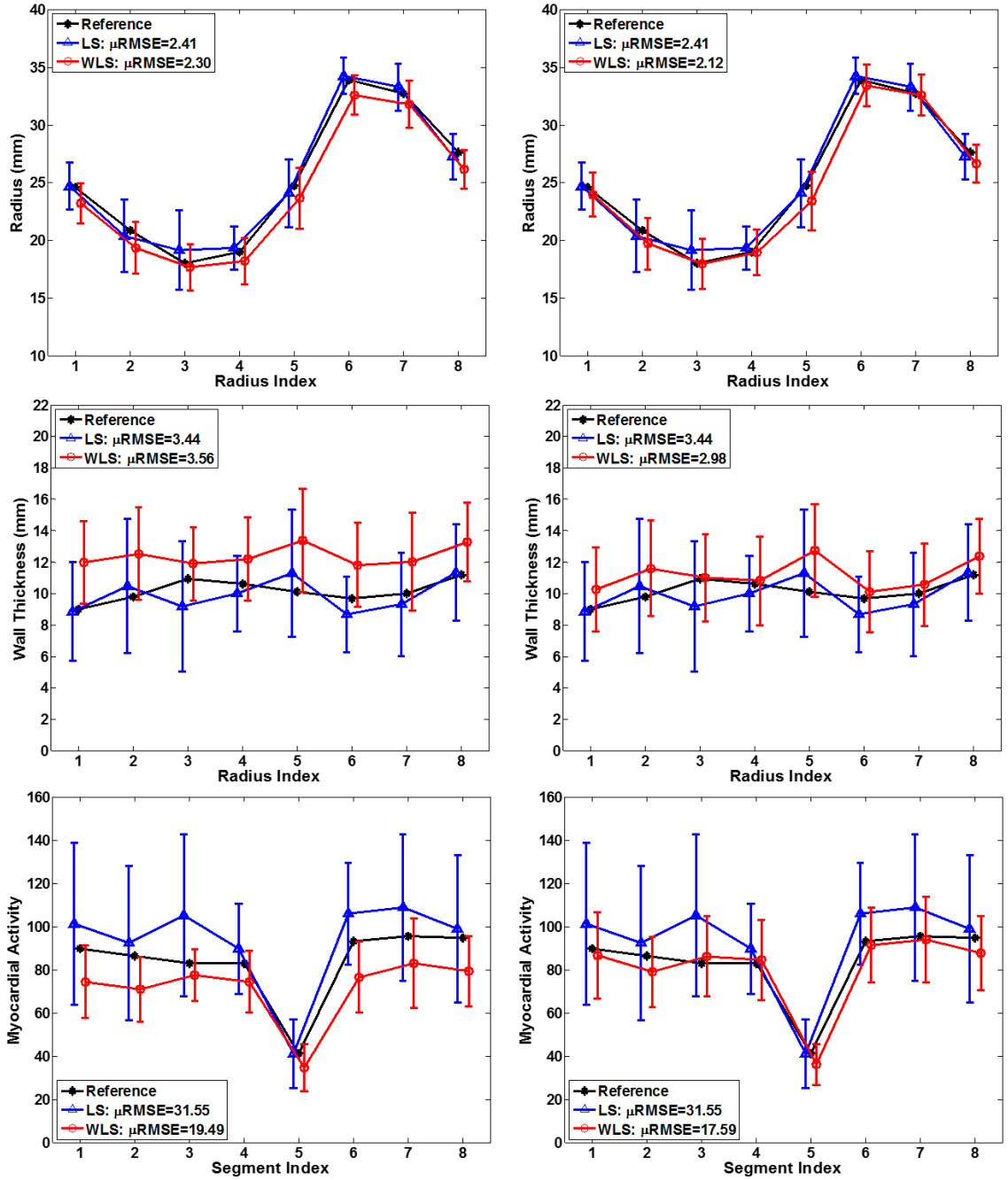


Figure 4-11. Comparison of LS and WLS fitting with OS-EM reconstructed images. The references are from LS fitting of the noise-free reconstruction. Left: the variance was assumed to be proportional to the square of the mean. Right: the variance was assumed to be proportional to the mean. The error bars represent the standard deviation over 50 noise realizations.

4.5 The Thickness Prior

One function of the shape prior is to stabilize the solution of the ill-posed reconstruction problem by introducing additional information about the LV geometry. To demonstrate its effectiveness, the proposed method was applied to the FBP reconstructed noisy image using different values of the regularization parameter. The parameters were optimized with respect to the objective function using the MultiStart method described above. Among the 1000 initial point trials, the 10 resulting in the smallest value of the objective function were selected for each regularization parameter. Figure 4-12 shows the averaged standard deviation of the myocardial activity parameters over segments as a function of the regularization parameters. Figure 4-13 qualitatively compares the first three sets of the estimated myocardial activities.

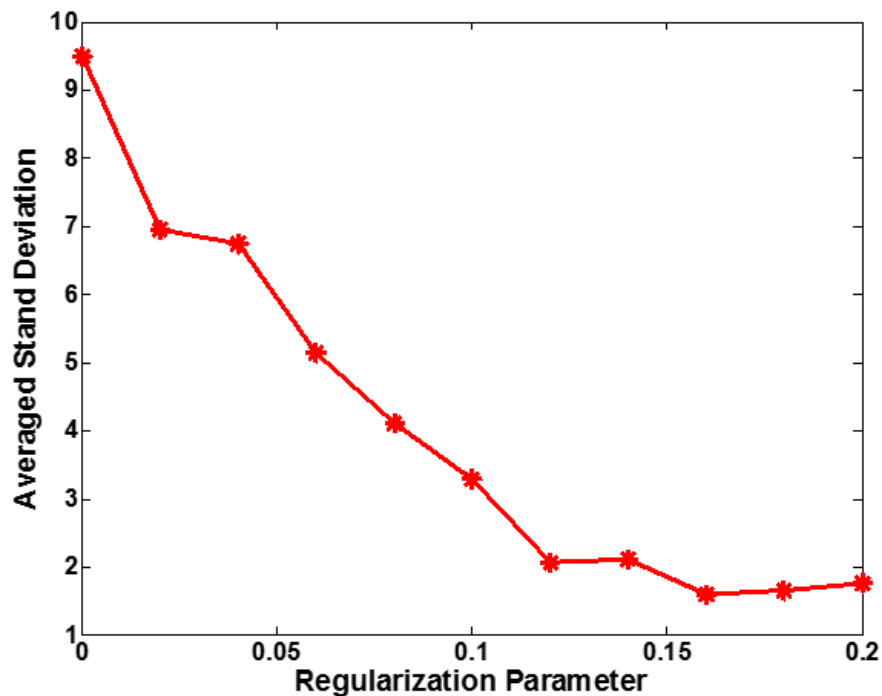


Figure 4-12. Illustration the relationship between the prior strength and the stability of the solution.

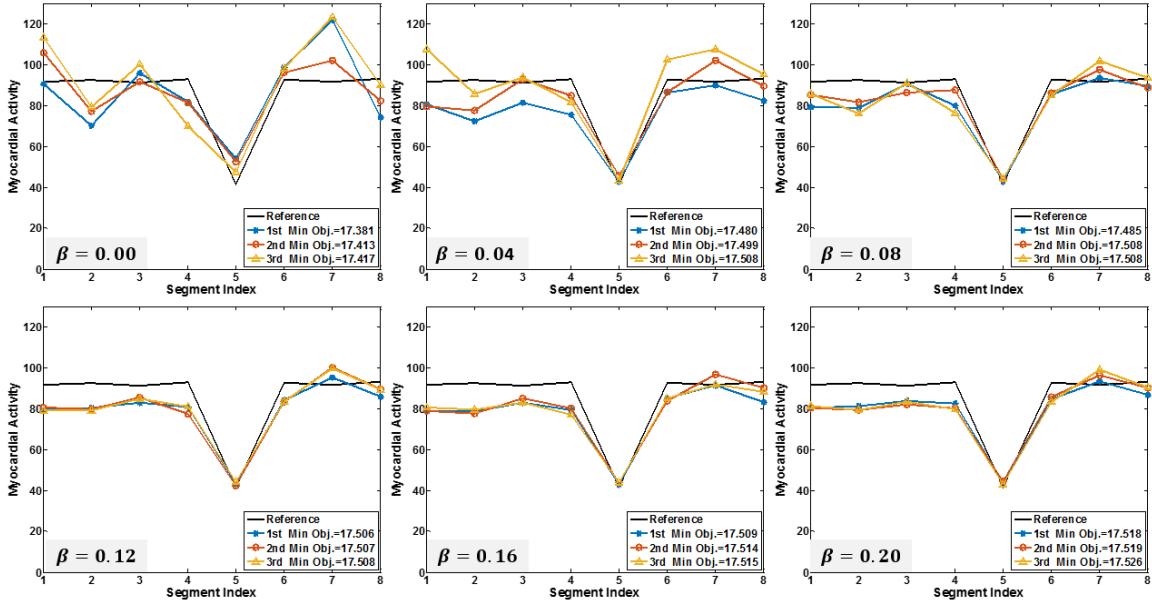


Figure 4-13. Illustration of the effect of the shape prior and its ability to stabilize the solution.

Without the prior or with a small value of the prior strength, there were significant variations between the three selected curves, although the corresponding objective function values were close to each other. Generally, the variations monotonically decreased with increased prior strength. The observation indirectly indicates that the uniform-thickness prior improved the stability of the model-based reconstruction problem.

It should be understood that the improved stability was obtained at the expense of potential biases, since the prior does not exactly quantify the characteristics of the object to be estimated. Therefore, it is important to use an appropriate value of the regularization parameter to achieve an appropriate balance between fitting the observed data and the prior knowledge. If the prior is too weak, it may not help to improve the stability; if it is too strong, the estimated parameters might greatly deviate from the truth.

Figure 4-14 plots the mean value of the data-fitting term against the mean value of the prior term (not scaled by the parameter β) for various values of the regularization parameter. As expected, the variance of the wall thicknesses became increasingly smaller with increased prior

strength. In the following, the regularization parameter $\beta=0.1$ was selected for the standard noise data and $\beta=0.2$ for the high noise data when fitting the simulated FBP reconstructed images. The choices allowed a standard deviation of approximate 0.9mm maximum in the thickness parameters.

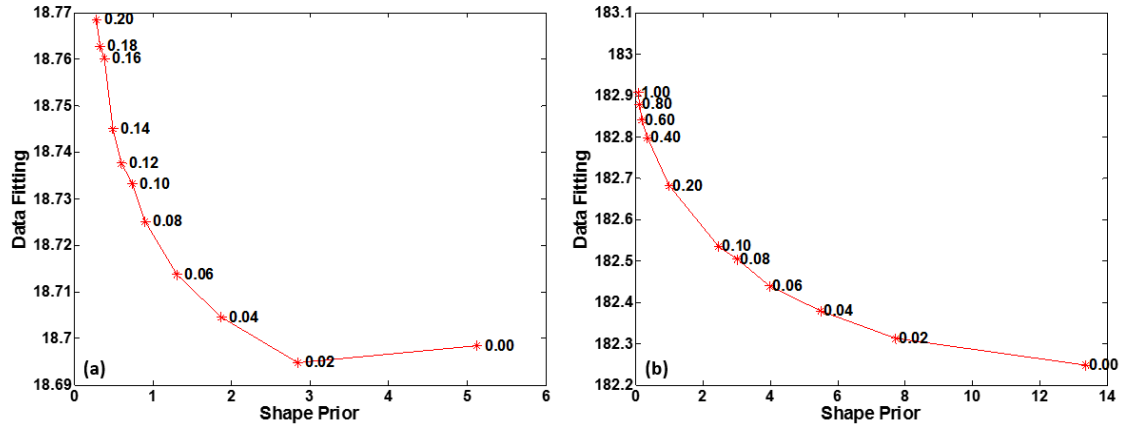


Figure 4-14. The mean value of the data-fitting term versus the mean value of the shape prior over 50 noise realizations using FBP for different values of the regularization parameter: (a) the standard noise data; (b) the high noise data.

4.6 Parameter Estimation

In this section, we evaluated the proposed model-based reconstruction method including all the various modeling approximations discussed before. The method was applied to the simulated FBP reconstructed short-axis images at the standard the high noise levels.

Figure 4-15 compares the estimated endocardial radius, wall thickness, and myocardial segmental activity parameters, with and without the shape prior. The model images generated from the mean model parameters are displayed in Figure 4-16.

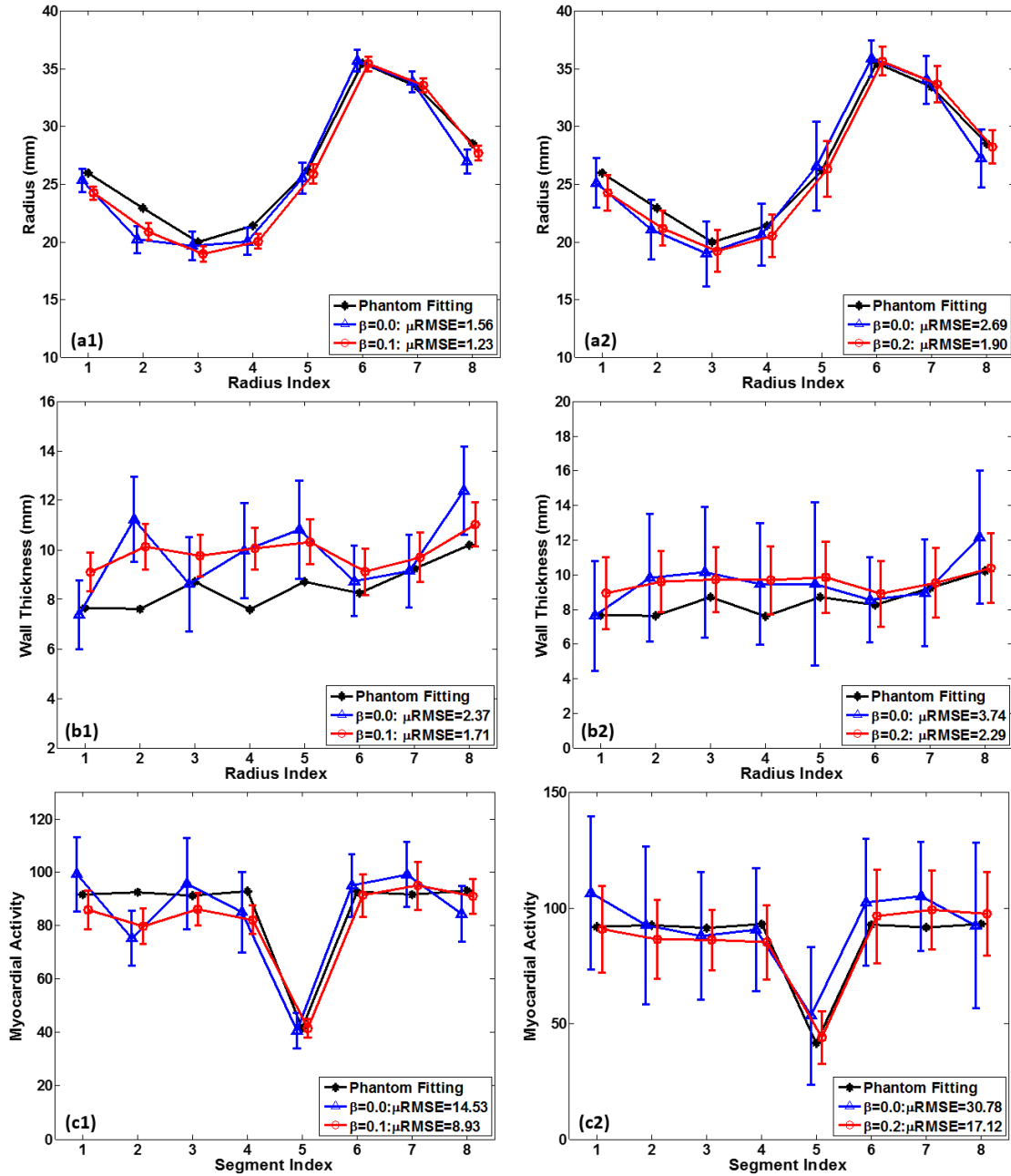


Figure 4-15. Estimated (a) endocardial radius, (b) wall thickness and (c) myocardial segmental activity parameters from FBP reconstructed images. The error bar represents the standard deviations over 50 noise realizations. The left and right columns correspond to the standard and high noise data, respectively.

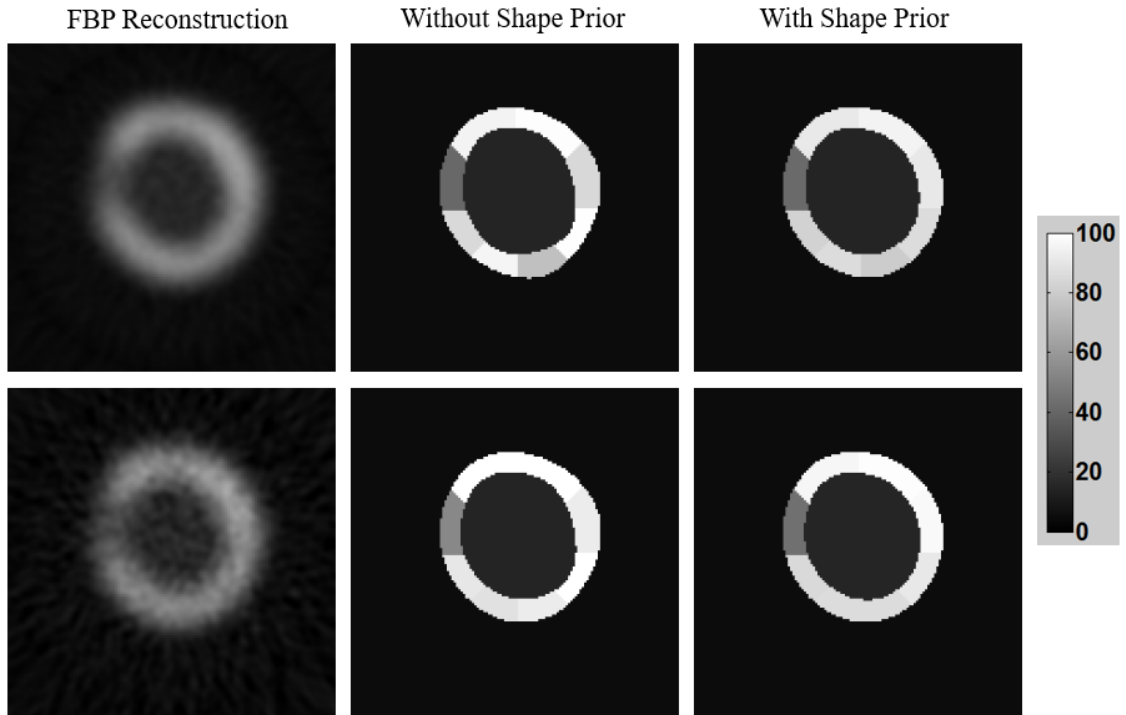


Figure 4-16. Comparison of the mean FBP reconstructed image and the mean model images. The top and bottom rows correspond to the low and high noise levels, respectively.

Comparing the mean model parameters and the phantom fitting truth, the size of the myocardium was overestimated and the myocardial activity concentration was underestimated. However, the difference was sufficiently small, demonstrating the high accuracy of the proposed method. Qualitatively, the perfusion defect could be easily discriminated based on the mean model images. The improved contrast also demonstrates the effectiveness of the implicit PVC in recovering the absolute uptake quantification.

On the other hand, the large error bars indicate that the proposed method suffered from considerable variability, especially at the high noise levels. The incorporation of the thickness constraint did consistently improve the estimation precision to some extent. However, the variability might still pose a challenge in consideration of the low counts in the gated myocardial perfusion images.

To provide better visualization of the variability, the estimated myocardial activity concentration parameter was plotted against the corresponding wall thickness parameter of the abnormal segment (which contained the perfusion defect) and the opposing normal segment. The distributions of data points based on 50 noise realizations are displayed in Figure 4-17. Without the shape prior, the wall thickness ranged from 2mm to 20mm for the abnormal segment for the high noise data. The constraint reduced the spread of values around the truth. However, the deviations in thickness and uptake in both the normal and abnormal segments were large and there was a significant correlation.

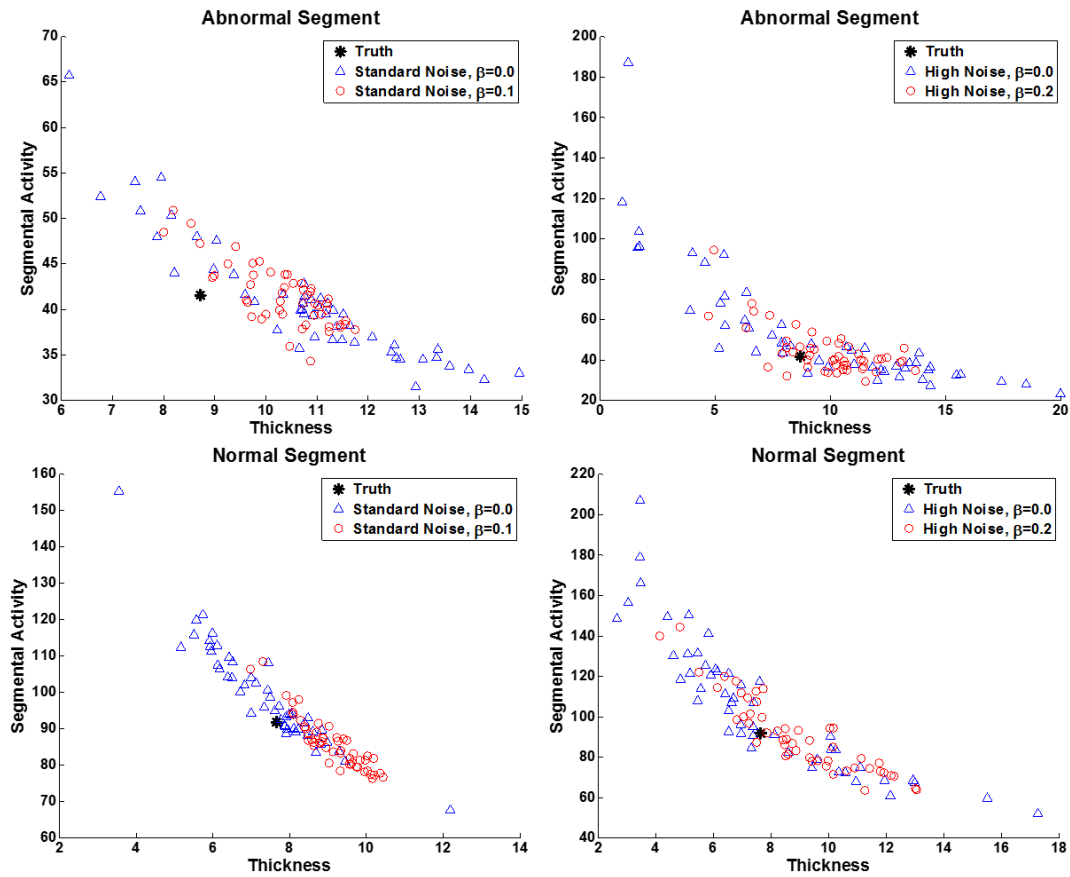


Figure 4-17. Scatter plots of the estimated myocardial activity versus the wall thickness of the abnormal segment (#5) and the opposing normal segment (#1) based on 50 noise realizations. The left and right columns correspond to the standard and high noise levels.

Based on the scatter plots in Figure 4-17, overestimation of wall thickness was generally associated with underestimation of myocardial activity concentration, and vice versa. To gain further insights into the relationship, the mean myocardial concentration was plotted against the mean thickness, as shown in Figure 4-18. The data points from 50 noise realizations were also fitted with a linear function. The R^2 values indicate that the relationship was well described by a linear model, especially when the thickness prior was used. The relationship implies that the total activity in myocardial segments (i.e., the product of activity concentration and segment volume) would be less sensitive to noise. In addition, the truth point, which represented the true activity concentration and wall thickness, was always located in the lower left region of the fitted line. This deviation might correspond to the biases from the approximate resolution and noise modeling. Note that the estimated thickness and concentration pairs averaged over the myocardium ring also had large variations. The maximum overestimation errors of the wall thickness were about 30% and 50% for the standard and high noise levels, respectively.

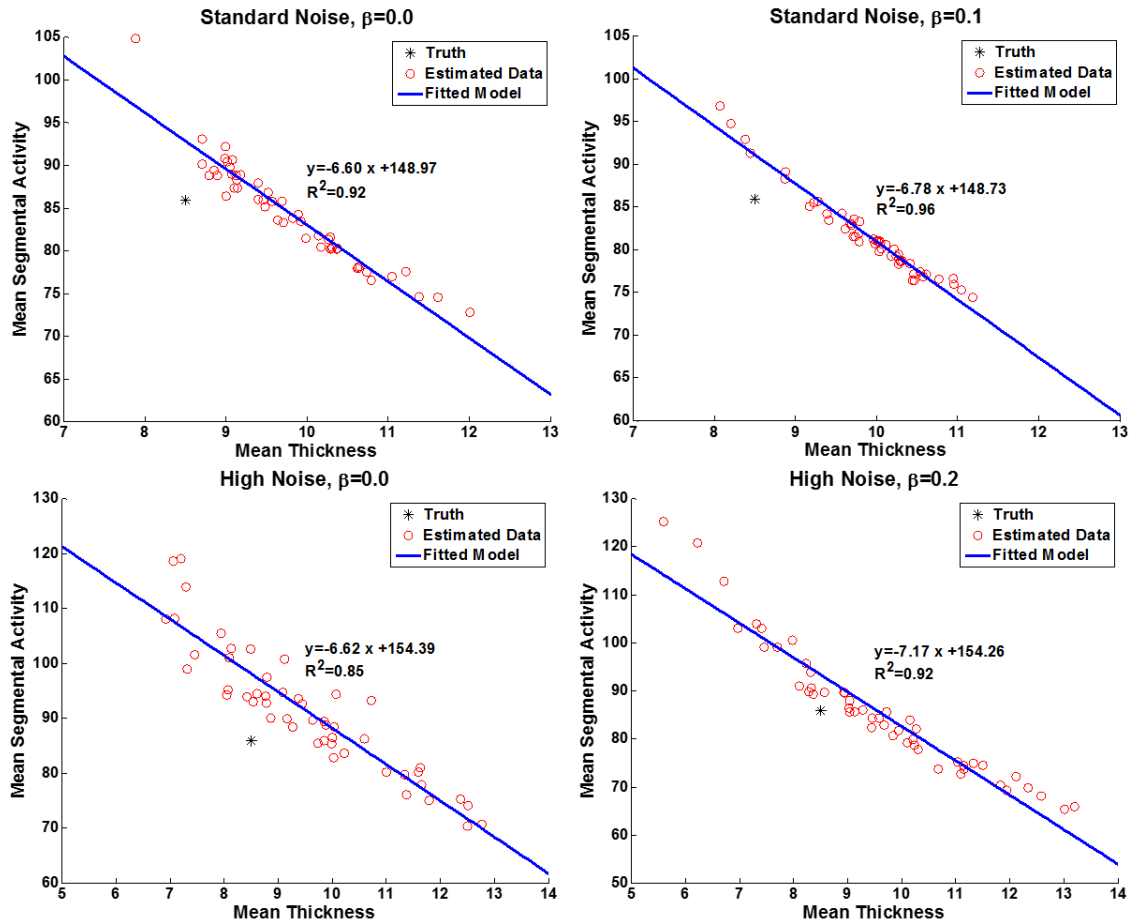


Figure 4-18. The mean of estimated myocardial segmental activity parameters versus the mean of wall thickness parameters. The data points based on 50 noise realizations were fitted with a linear function.

The estimates of the blood pool shape and activity are also important. The activity concentration is useful in deriving the input function for kinetic modeling. The cavity volume, which can be computed from the endocardial radius parameters, is associated with several left ventricular function parameters. Figure 4-18 quantifies the estimated concentration and cavity volume of the blood pool based on 50 noise realizations. The values of the estimates were more disparate for the higher noise level. In this case, the introduction of the shape constraint made little difference in reducing the variations. This makes sense since the constraint only penalized the thickness parameters. On the other hand, the underestimation of the concentration is unexpected as

spillover of activity from the myocardium would, at first thought, seem likely to result in overestimation of the activity in the blood pool. This underestimation might be related to the underestimation of the cavity volume and the overestimation of the wall thickness. As a result, a small fraction of the highly perfused myocardium was mistakenly included in the true blood pool ROI. Therefore, the concentration of the blood pool would be underestimated as a compensation.

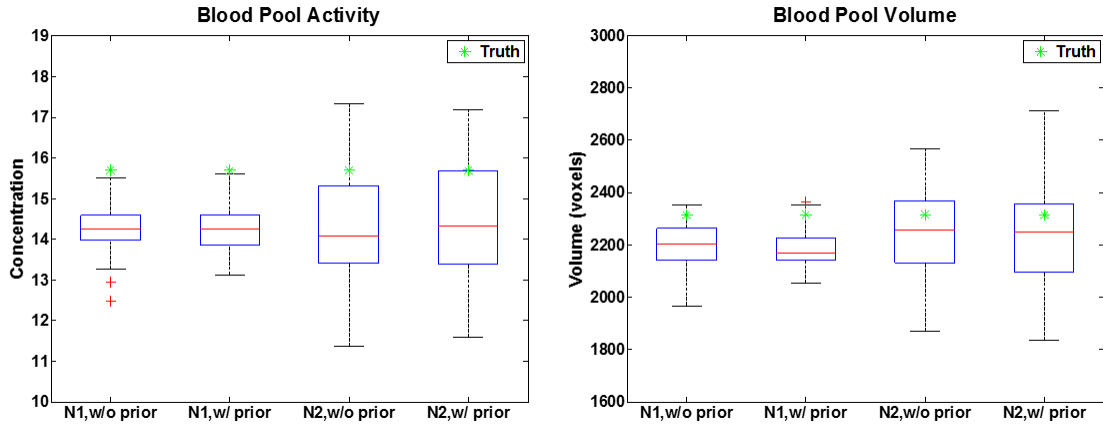


Figure 4-19. Box plots summarizing the distributions of estimated blood pool activity concentration and the cavity volume.

4.7 Simplified 1D Model

The above results demonstrate that the proposed method was sufficiently accurate based on the simulated short-axis images. It is computationally challenging to accurately model resolution and noise in reconstructed images. Also, the MultiStart method with 1000 initial trials is not guaranteed to reach a global minimum and could produce bias. Even with accurate resolution and noise modeling and perfect global optimization, it is unknown whether the proposed model-fitting method will generate biased model parameters. In addition, it is unknown whether accounting for resolution and noise statistics in the image formation process will improve LV segmentation, and what factors resulted in the observed variability in the values of the estimated parameters.

A simplified 1D model was used to investigate these questions. The true object f_T was comprised of a rectangular function with height $h = 10$ on a uniform background; the background to signal intensity ratio was 1:10. The width of the signal ranged from $27mm$ to $123mm$ in increments of $6mm$, while the size of the object was $1000mm$. The imaging system consisted of convolving the above object with a Gaussian kernel G_σ with a FWHM of $40mm$, giving the noise-free observed object, and then adding uncorrelated Gaussian noise, n_G , with a mean of 0 and a standard deviation of 1. The process is described mathematically by the following equation and the object and measured data are displayed in Figure 4-20.

$$f_O = G_\sigma * f_T + n_G$$

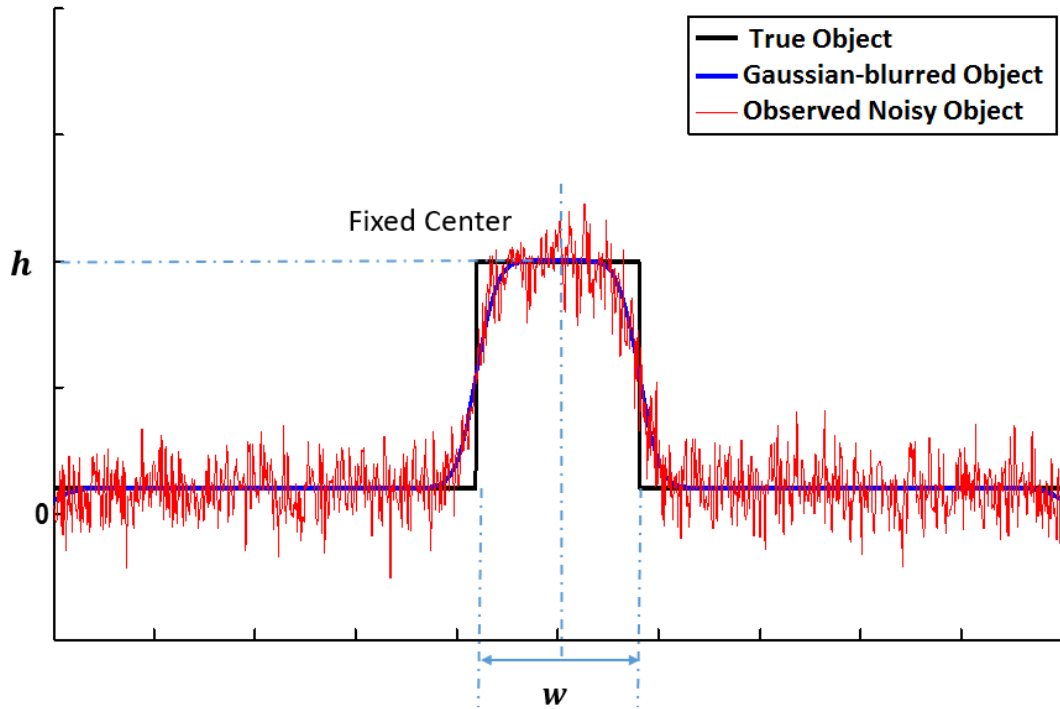


Figure 4-20. A simplified 1D model to simulate the proposed method.

Similar to the proposed method, the objective of the 1D model is to estimate the signal width w and height h that minimize the LS difference between the observed data and the Gaussian-blurred square wave model $s(w, h)$, which is expressed as follows.

$$\min_{w,h} \|f_o - G_\sigma * s(w,h)\|^2$$

The objective function was globally optimized by exhaustively searching the parameter space. The center of the signal in the model $s(w, h)$ was aligned with the center of the true signal in during model fitting. No noise model mismatch was present, but the FWHM of the resolution kernel was deliberately perturbed by $\pm 10\%$ to simulate PSF measurements.

Alternatively, the object structure was also detected using a conventional gradient-based method, which does not need prior information about resolution and noise. It first smoothed the observed noisy signal using a low-pass Gaussian filter (FWHM=11.78) and then determined the boundaries by locating the points that corresponded to the maximal gradient magnitude.

The two methods were applied to the object simulated with a variety of signal widths. For each width, we generated 1000 noise realizations. The estimation error was normalized by the corresponding true object width. The mean and standard deviation of the normalized error are visualized and compared in the figure below.

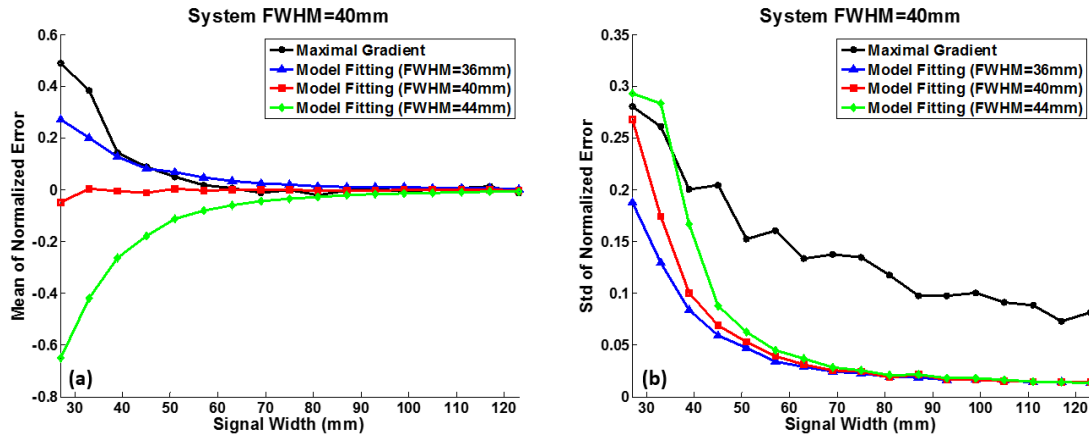


Figure 4-21. Plots of normalized error in the estimated signal width using the 1D model fitting method as a function of signal width. For comparisons, results of a conventional gradient-based method are shown. The (a) mean and (b) standard deviations of the percentage estimation error are plotted against the object width over 1000 noise realizations.

The mismatched resolution introduced estimation biases, the severity of which became increasingly significant for smaller objects. Using smaller FWHM in the fitting was led, on average, to overestimation of the object size, and vice versa. Without resolution mismatch, the width estimate was unbiased over the entire range of object sizes investigated. In contrast, the gradient-based method tended to overestimate the object size when it was comparable to or smaller than the system FWHM. The mean percentage error was over 10% at the system FWHM. The phenomenon was also noticed in a previously-proposed LV segmentation method that relied on image gradients to delineate the myocardial surfaces (Nuyts, Suetens et al. 1991).

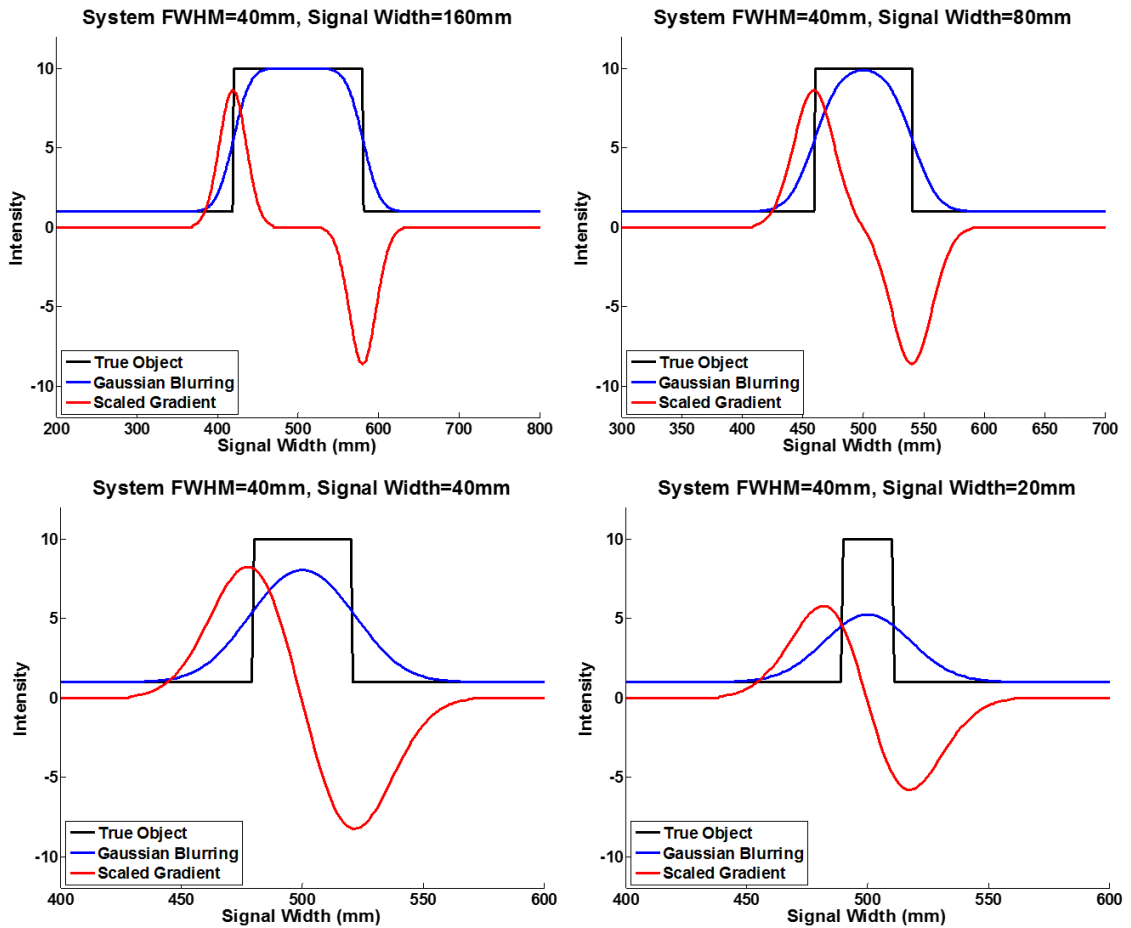


Figure 4-22. A simplified 1D model to illustrate the overestimation of signal size with gradient-based methods when it is comparable to or smaller than the system FWHM.

Figure 4-22 illustrates the size overestimation of the gradient-based method. When the object was sufficiently large, the gradient of the observed signal exhibited two peaks with opposite signs, while the maximal magnitude points were aligned with the object edges. For a reduced object size, the two gradient peaks were closer together. When the size was comparable to the system FWHM, the two lobes within the object were merged together, resulting in an asymmetry in the two gradient peaks. Consequently, the points of the maximal gradient magnitude deviated outwardly from the object edges. When dealing with noisy data in practice, denoising is normally a necessary step for gradient-based methods. The involved blurring effect will also contribute to the size overestimation.

In terms of estimation precision, smaller objects are likely to suffer more variability, as shown in Figure 20b. However, it was considerably smaller with the proposed model fitting method than with the gradient-based method. When the object width was equal to the system FWHM, the normalized mean standard deviation of the former was approximately 10% while that of the latter was almost doubled.

The simplified 1D model has indirectly answered the three questions proposed in the beginning. First, the model-fitting method was inherently unbiased, not like gradient-based segmentation methods with small objects. The estimation biases mainly result from approximated modeling in the fitting process or the flawed global optimization. Second, modeling resolution and noise in the image is likely to improve segmentation accuracy and precision in comparison with conventional gradient-based methods that only depend on image pixel values, especially when the object size is comparable to or smaller than the system FWHM. Third, the similarity between myocardium wall thickness and image resolution greatly contributed to the variability when applying the proposed method to the simulated short-axis images. The main cause was not because of the imperfect global optimization scheme MultiStart, which might result in widely distributed local minima between noise realizations.

These observations have several other important implications. First, the current uniform-thickness shape prior can only reduce the variability but cannot eradicate it, even using an extremely large regularization parameter. It only quantifies the relative difference between thickness parameters but provides no absolute information about them. The thickness can be entirely underestimated or overestimated, just like in the simplified 1D model. On the other hand, without compromising the estimation accuracy, the variability is an inevitable problem when segmenting LV from myocardial perfusion images. It is impossible to accurately determine the thickness merely based on the given image. The problem can be alleviated with improved system resolution, which implies the better performance with cardiac PET than SPECT.

4.8 Discussion

In this chapter, we investigated the proposed model-based reconstruction method on the basis of its components, including the mismatches in the geometry and activity distribution models, the approximations in the resolution and noise modeling, and the effectiveness of the shape prior. In spite of the imperfect modeling, the estimated model parameters were reasonably close to the truth. Particularly, a simplified 1D model revealed crucial properties about the estimation accuracy and precision as a function of the object size and demonstrated the superiority of the model-fitting method in segmentation comparing to gradient-based methods. However, some other issues need further discussion.

An important feature of the geometry model is to generate continuous and smooth myocardial contours regardless of image noise. However, the endocardial surface is actually not smooth due to the presence of papillary muscles. Theoretically, these muscles can be depicted with a sufficiently large number of radial profiles. The inherent smoothness is a relative measurement depending on sampling intervals. Meanwhile, papillary muscles are commonly not differentiable in myocardial perfusion SPECT because of its limited spatial resolution. Even though they become

more visible in cardiac PET, the relatively small size restricts their influence on the proposed method. Thus, we did not use more sampling radial profiles to sacrifice efficiency for the unnecessary modeling capability. The choice of eight samples was a good trade-off between simplicity and accuracy in modeling short-axis slices.

The activity distribution model assumes homogeneous blood pool, myocardial segments, and the background. The resulting model image is noise-free but provides no details of tracer uptake within each region, such as transmural heterogeneity. Some important image details might have been eliminated along with reduced model parameters. The issue can be lessened by dividing the model image into more piecewise uniform regions. However, it is necessary to strike a balance between the efficiency of the proposed method and the preservation of critical diagnostic information. It might imply that the proposed method can only supplement but cannot replace conventional reconstruction methods.

Since the proposed method focused on compensation for PVE, the imaging process in this study included only noise and resolution modeling but no attenuation and scatter modeling. It should be applied along with attenuation and scatter correction to improve activity quantification. Photon attenuation and scatter arise from the interactions with matter while the finite spatial resolution comes from limitations of the imaging system (Galt, Garcia et al. 1990). Therefore, their corrections can be separately performed on the observed data or the resulting model image.

In this study, the Gaussian approximated system PSF was obtained by fitting the blurred phantom image into the noise-free reconstruction. However, the technique is only feasible in the simulation studies. In practice, it is usually derived based on measurements from the reconstructed image. For FBP, the PSF is independent of the underlying tracer distribution and the measurement is straightforward: place a point source at the target location and then image and reconstruct it the same way as in the given image (Tohka and Reilhac 2008). For OS-EM, however, the resolution is object-dependent and the above method is not accurate. A perturbation method is commonly used

to characterize the regional resolution (Wilson 1994). It perturbs the pixel values at the target position in the original reconstruction to simulate a “new” object that superimposes a point source on the true object. The perturbed image is then projected and reconstructed without changing the settings. The difference between the new and original reconstruction can roughly represent the PSF. Currently, the PSF only included blurring effects in the imaging system and the reconstruction algorithm. The effect of cardiac motion can also be integrated into the PSF (Nuyts, Maes et al. 1996), such that the proposed method might be extended from gated myocardial perfusion images to ungated ones.

The uniform-thickness shape prior initially attempted to serve two purposes. One was to regularize the ill-posed problem with improved stability, which had been validated in the above. The other was to penalize the narrowing of myocardium at the location of perfusion defects. As expected, no underestimation of the wall thickness of the defected segment was noticed with the prior. However, the underestimation was not observed even when the prior was not incorporated. Thus, the results failed to show whether the prior can fulfill the second purpose. The absence of the anticipated thickness underestimation might be due to the relatively high uptake in the defect. As a result, the myocardium narrowing was considerably less favorable when fitting the observed data, even with the prior. If the defect had 100% severity, the advantage of the prior might be manifested.

Meanwhile, other priors might be investigated to introduce additional information. For instance, the shape of the myocardial contour is approximately elliptical on the short-axis view. In addition to the current prior, we experimented another one that attempted to minimize the distance between the radius samples and the fitted ellipse contour. Figure 22 assesses the model parameters estimated from the FBP reconstruction at the higher noise level, with and without the new prior. It did not help with the thickness estimation. Nevertheless, it effectively reduced the variability of radius estimation, resulting in smaller errors in the resulting radius parameters as well as the myocardial segmental activity parameters.

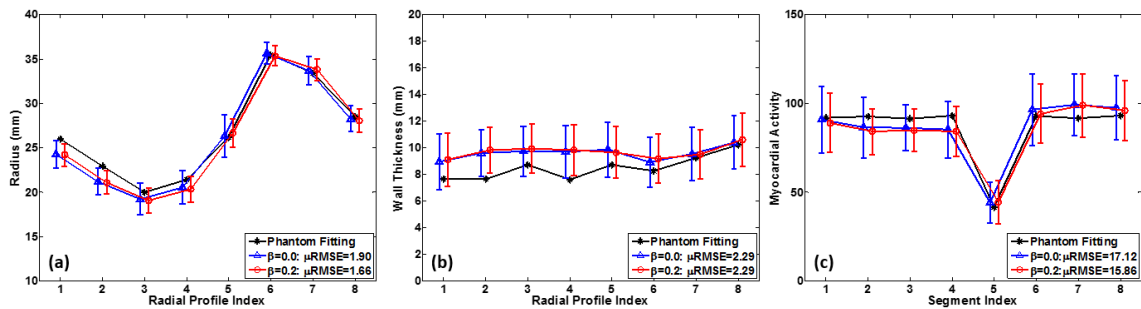


Figure 4-23. The incorporation of a new shape prior that encourages an elliptical distribution of endocardial contour in the short-axis slice.

In this chapter, the objective function was optimized using MultiStart, which is time-consuming and might still get stuck in a local minimum. However, the global minimum may not be strictly required in practice. For instance, the widely used OS-EM reconstruction does not guarantee the convergence to the global optimum, and the iterations are even terminated early to suppress noise amplification (Wu 1983). Provided that the results can truthfully reflect the underlying activity distribution to some extent, it is desirable to develop an efficient and robust optimization method. The next chapter will present results using the proposed alternating optimization scheme.

5. Results and Discussion (2D): Efficient Optimization

The proposed model-based method has high computational costs compared to voxel-based reconstructions. This is partly because of the additional step required to generate voxelized images from the model, but largely because the model parameters are non-linearly related to both the projections and the reconstructed image. As a result, we developed a group-wise alternating optimization scheme to improve computational efficiency. The proposed scheme was first characterized by quantifying its performance on perturbed initial estimates. The scheme was then evaluated using simulated short-axis images from the perspective of LV segmentation, mid-myocardial surface estimation, PVC, and defect detection. The details are given in the following.

5.1 Group-wise Alternating Optimization

It is meaningful to investigate the performance of the proposed alternating optimization scheme in response to a wide distribution of initial estimates due to the impact of initial model parameters on the optimization results. For simplicity, the initial estimate was assumed to consist of uniform endocardial radii (r), uniform wall thicknesses (t), and homogenous myocardial segmental activities (a_{myo}), which corresponded to a short-axis model image with endo- and epi-cardial contours that are concentric circles. In addition, the activity concentrations were assumed to be homogeneous in the blood pool (a_{bp}) and background (a_{bkg}). Totally, five parameters were needed to specify an initial estimate.

To explore the impact of initial parameters, the initial parameters were randomly sampled from predefined ranges. Table 5-1 shows the eleven combinations of ranges of the five parameters used in this work. The trials of initial points were generated by uniformly sampling these intervals in each combination. The reference combination, abbreviated as Ref, consisted of ranges approximately centered at the mean values of the corresponding parameters of the phantom image. The other combinations were defined by shifting the ranges for one of the parameters to higher or

lower values while keeping other ranges fixed. Perturbing the parameters separately in this way provides insight into the sensitivity of each parameter. Shifting to higher or lower values represents methods for estimating the initial estimates that result in over- or under-estimation. The widths of the ranges represent the ranges of errors that might be expected for real methods for estimating the initial parameter values. These combinations of ranges are denoted by letters indicating the parameter that was shifted: r for the endocardial radius, t for the myocardial thickness and myo, bp, and bkg for the myocardial, blood pool, and background activity concentrations, respectively. The direction of shifting is denoted by H or L for shifting of the range to higher or lower values, respectively.

Table 5-1. Combinations of sampling ranges of endocardial radius (r), wall thickness (t), and activity concentrations in the myocardium (a_{myo}), blood pool (a_{bp}), and background (a_{bkg}).

	Abbreviations	r (mm)	t (mm)	a_{myo}	a_{bp}	a_{bkg}
Phantom Mean	Phan	26.7	8.5	85.9	15.0	5.0
Reference	Ref	[20, 32]	[7, 10]	[70, 100]	[12,18]	[4,6]
r	rL	[16, 20]	[7, 10]	[70, 100]	[12,18]	[4,6]
	rH	[32, 36]	[7, 10]	[70, 100]	[12,18]	[4,6]
t	tL	[20, 32]	[5, 7]	[70, 100]	[12,18]	[4,6]
	tH	[20, 32]	[10, 12]	[70, 100]	[12,18]	[4,6]
a_{myo}	myoL	[20, 32]	[7, 10]	[55, 70]	[12,18]	[4,6]
	myoH	[20, 32]	[7, 10]	[100, 115]	[12,18]	[4,6]
a_{bp}	bpL	[20, 32]	[7, 10]	[70, 100]	[9,12]	[4,6]
	bpH	[20, 32]	[7, 10]	[70, 100]	[18,21]	[4,6]
a_{bkg}	bkgL	[20, 32]	[7, 10]	[70, 100]	[12,18]	[3,4]
	bkgH	[20, 32]	[7, 10]	[70, 100]	[12,18]	[6,7]

One critical parameter in an alternating scheme is the grouping and order of the parameters optimized in a particular alternation. We investigated 3 schemes. The first two schemes partitioned the model parameters into three groups: (1) myocardial radius and blood pool activity ($a_{bp}, r_i, i = 1, \dots, N_r$), (2) segmental activities ($a_i, i = 1, \dots, N_s$), and (3) myocardial thickness and background activity ($a_{bkg}, t_i, i = 1, \dots, N_r$). The first scheme optimized the parameters in group 1, then group

2, and finished with group 3. The second scheme used the same three groups but switched the optimization order of groups 2 and 3. The third scheme used two groups, a geometry group $(r_i, t_i, i = 1, \dots, N_r)$ and an activity group $(a_{ap}, a_{bkg}, a_i, i = 1, \dots, N_s)$, and optimized them in that order. The three schemes are referred to as *3Groups-Order123*, *3Groups-Order132* and *2Group-Order12*, respectively.

The proposed model-fitting method was applied to a simulated FBP reconstructed short-axis image representing the standard noise level. The model parameters were optimized using the three alternation schemes, which were initialized with 100 random points from each combination of the sampling ranges. Figure 5-1 shows the resulting values of the objective function and the RMSEs of the estimated myocardial model parameters. The RMSEs were computed with reference to the results using the MultiStart method, which is more computationally intensive but also more likely to reach a global maximum and averaged over radii or segments. The error bars represent the standard deviations over the 100 initial points from each combination of perturbed initial parameter ranges.

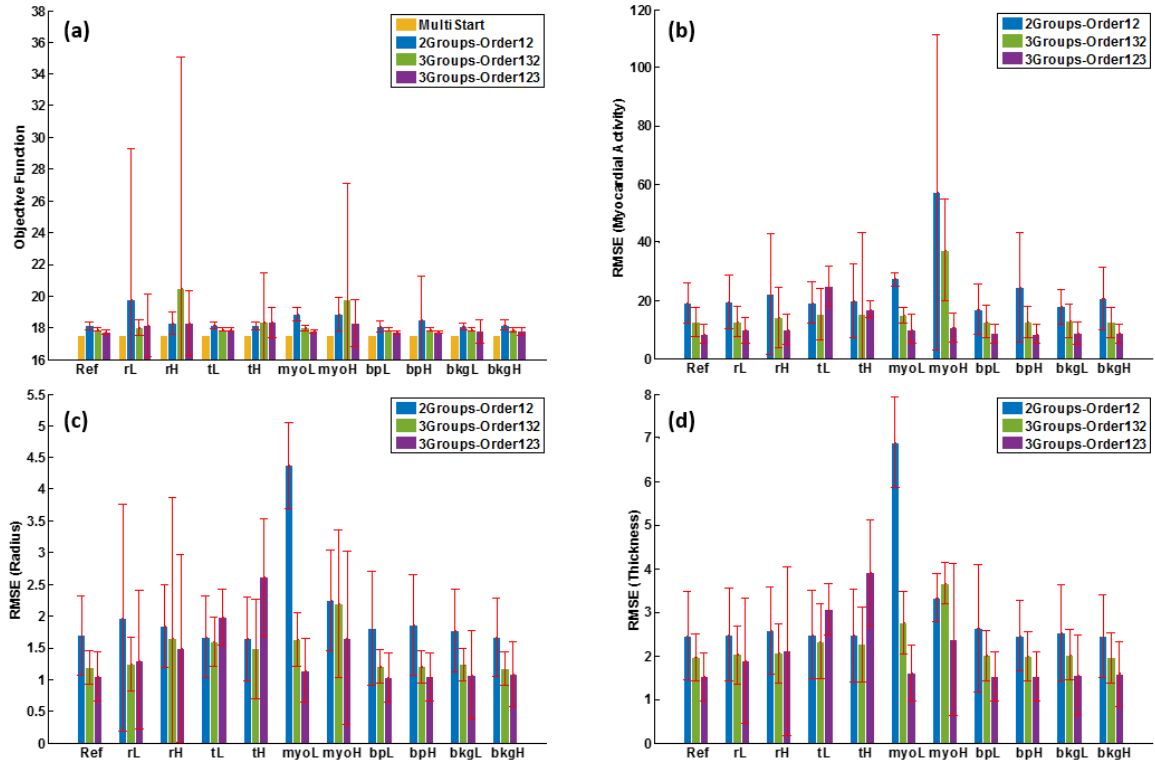


Figure 5-1. Results from the three proposed optimization schemes, 3Groups-Order123, 3Groups-Order132, and 2Groups-Order12. For each of the optimization ranges described in Table 5-1 the graphs show (a) the resulting values of the objective function and RMSEs of the estimated (b) myocardial segmental activity, (c) endocardial radius, and (d) wall thickness parameters.

As shown in Figure 5-1a, the 3Groups-Order123 scheme generally resulted in comparable or smaller mean values of the objective function after minimization than the other two. Also, the mean values varied less between the eleven combinations of initial parameter ranges. Finally, the 3Groups-Order123 scheme resulted in similar values of standard deviations over the range combinations than the other two between combinations, indicating more consistent sensitivity to the initial parameter values. The mean values of the objective function and the standard deviations increased for the range combination rL for 2Groups-Order12, and at rH and myoH for 3Groups-Order132 in comparison to the reference combination of ranges. These results imply that the proposed scheme was more effective (lower mean value of the objective function) and robust (less

sensitive to initial parameter range and lower RMSE) in minimizing the objective function. In addition, the comparison of RMSEs shows that the 3Groups-Order123 scheme resulted in the smallest mean errors in the estimated myocardial activity, endocardial radius and wall thickness parameters except for range combinations tL and tH. It seems that the thickness could not be optimized as effectively as other parameters.

In general, the 3Groups-Order123 alternating scheme outperformed the other two schemes in minimizing the objective function and producing accurate estimation, except when the initial wall thickness estimate was far from the truth. To address the problem, multiple wall thicknesses were used to generate multiple initial estimates from the reconstructed image using the method described in Chapter 3. The initial estimate resulting in the minimum value of the objective function was deemed as the global optimum. As a result, the 3Groups-Order123 scheme combined with the use of multiple initial wall thicknesses was adopted for the remainder of the work in this dissertation. The combined scheme is referred to as the proposed alternating scheme.

The proposed alternating scheme was applied to 50 noise realizations of the FBP reconstructed short-axis images at the standard noise level. Figure 5-2 plots the mean value of the minimized objective function versus the initial thickness for thicknesses ranging from 7.5mm to 16.5mm in increments of 0.5mm. A global minimum was achieved near 12.5mm. Note that the difference in the objective function between the global minimum and the value using the MultiStart method was very small (<0.2), demonstrating the comparable effectiveness of the two optimization methods.

To further investigate the influence of the initial wall thickness we compared the mean estimated wall thickness as a function of initial thickness using the proposed alternating optimization scheme. Figure 5-3 shows the results of this comparison. The alternating scheme resulted in a mean estimated wall thickness that was less than the initial wall thickness by approximately a fixed amount of 2.0mm for all the initial values investigated. Note that the resulting

mean thickness using the alternating optimization scheme with an initial thickness=12.5mm was very close to that obtained using the MultiStart method. In particular, there was an about a 1.5mm difference in the estimated mean thickness between the phantom fitting (truth) and the MultiStart results. This implies that the proposed alternating scheme is almost as good as the MultiStart method while being substantial less computationally intensive.

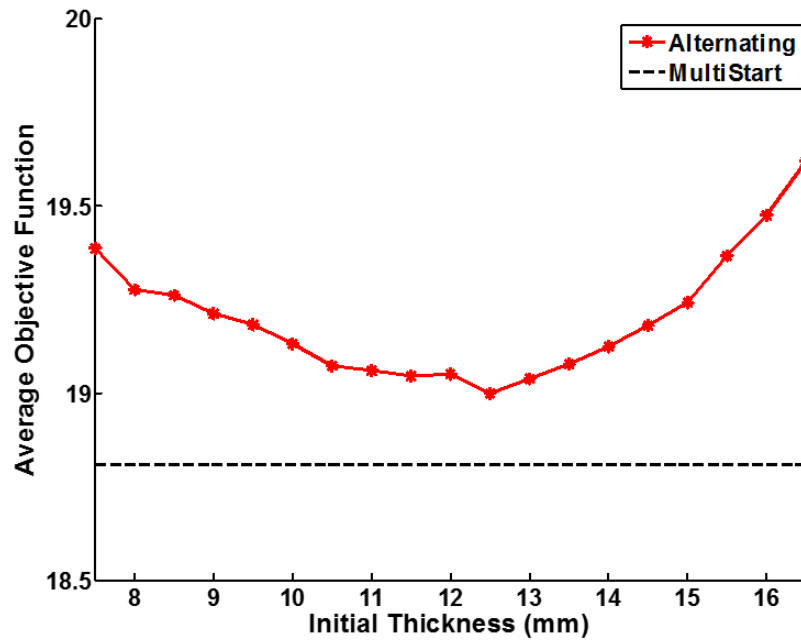


Figure 5-2. The smallest value of the objective function obtained using the proposed alternating optimization scheme versus the initial wall thickness.

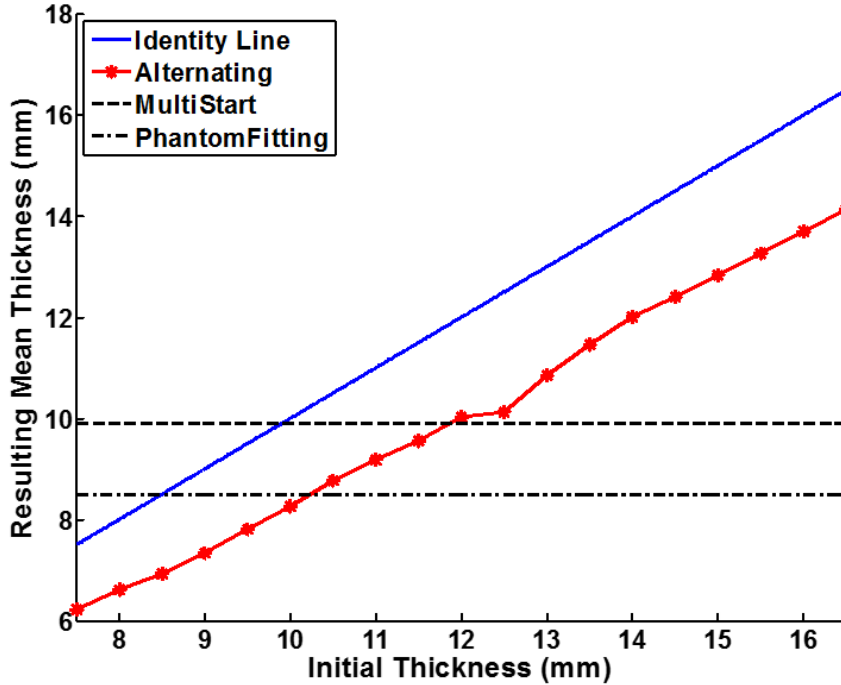


Figure 5-3. The mean wall thickness obtained with the proposed alternating scheme versus the initial values.

5.2 Parameter Estimation

Figure 5-4 compares estimated myocardial model parameters using the MultiStart method and the proposed group-wise alternating optimization scheme with initial values of the wall thickness evenly spaced over the range 7.5 to 12.5 mm. For the standard noise data, the two methods yielded comparable estimation errors ($\mu RMSE$). For the high noise data, however, the alternating scheme resulted in much smaller errors, as shown in Table 4-2.

The above observation is strongly related to the different ranges of initial thicknesses used in the two optimization methods. The MultiStart method randomly sampled the initial thicknesses from 0.5 to 1.5 times the mean wall thickness of the phantom, resulting in an approximate range from 4.5mm to 12.5 mm. The alternating scheme used eleven thicknesses equally spaced between 7.5mm and 12.5mm based on the average variations of the wall thickness of the normal myocardium. As indicated by the simplified 1D model in Chapter 4, there is a degeneracy between the wall thickness and system resolution in terms of their effects on the estimated images. This

degeneracy implies that the global minima were widely distributed over the 50 noise realizations. For the standard noise data, the ranges of initial thicknesses used in the two methods both seemed to be large enough to cover the range of likely global minima, which led to comparable estimation errors. However, due to the relative insensitivity of the objective function to changes in the wall thickness, higher noise data would tend to result in a larger spread in the range of estimated wall thicknesses. It seems that the range of initial thicknesses used in the alternating scheme was not large enough guarantee to reproduce the global optimal values of the parameters obtained with the MultiStart method. Consequently, the estimated model parameters were likely to be local minima due to the use of an insufficient range of initial estimates, resulting in the much smaller variations using the alternating method for the high noise data.

Table 5-2. RMSEs of estimated endocardial radius, wall thickness and myocardial activity parameters using the MultiStart method and the proposed alternating scheme for the standard and high noise data shown in Figure 5-4.

		RMSE of Endocardial Radius r_i (mm)	RMSE of Wall Thickness t_i (mm)	RMSE of Myocardial Activity a_i (pixel value)
Standard Noise	MultiStart	1.23	1.71	8.93
	Alternating	0.99	1.48	8.80
High Noise	MultiStart	1.90	2.29	17.12
	Alternating	1.51	1.61	13.26

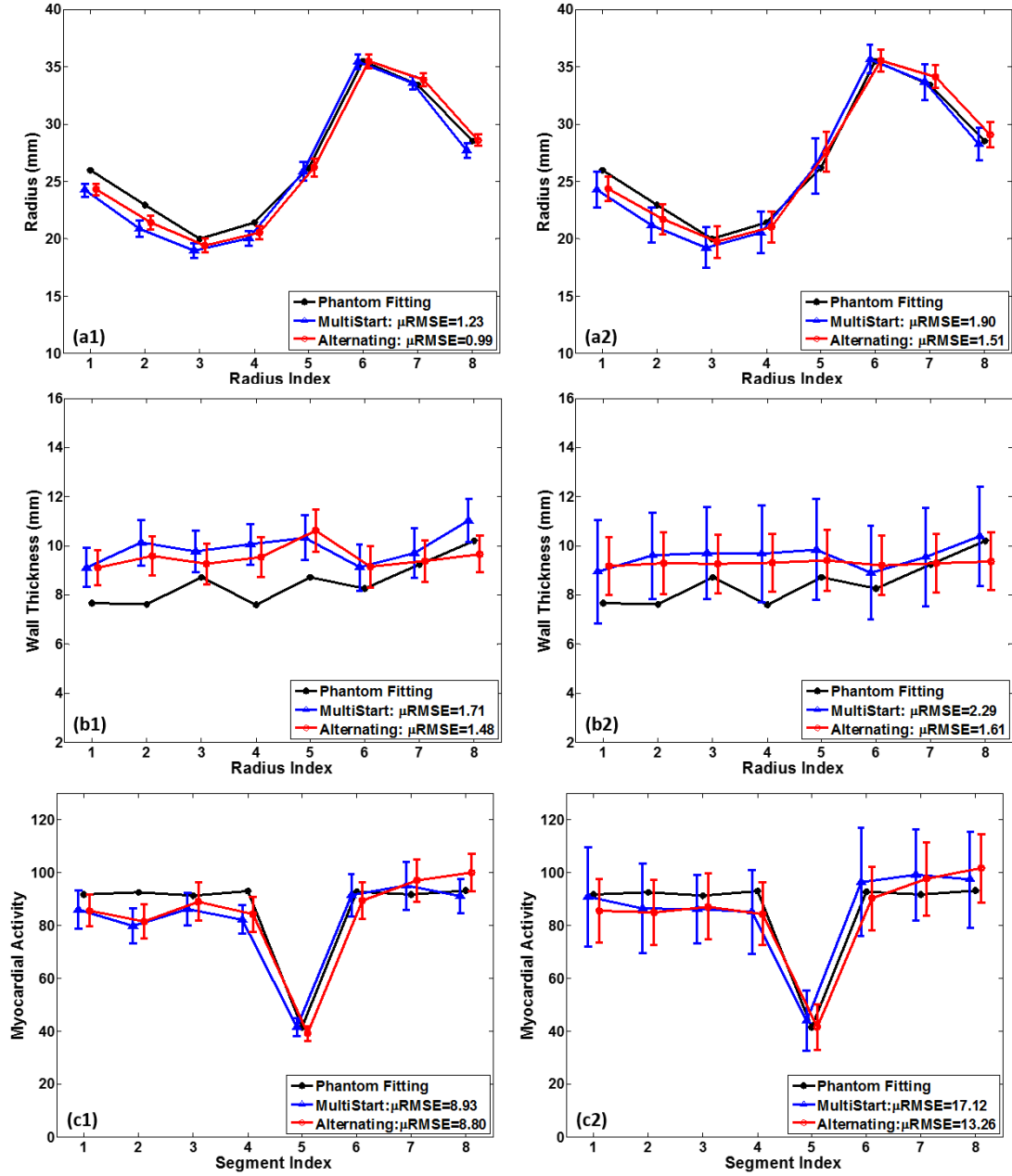


Figure 5-4. Comparison of values of the estimated (a) endocardial radius, (b) wall thickness and (c) myocardial activity parameters using the MultiStart method and the proposed group-wise alternating optimization scheme. The left and right columns correspond to the standard and high noise data. The error bars represent the standard deviations over 50 noise realizations of the FBP reconstructed short-axis images.

5.3 Left Ventricle Segmentation

Figure 5-6 compares the proposed method to thresholding in segmenting the myocardium from the FBP reconstructed short-axis images. The geometry model parameters used to model the myocardium were optimized using the alternating method and the MultiStart method. For the thresholding method, the pre-smoothing and the threshold used in the segmentation were optimized to maximize the mean DSC of segmented myocardium over 50 noise realizations. For the standard noise data, the standard deviation of the Gaussian denoising filter was 2.0mm and the pixel value threshold was 41.0 gave the maximum mean DSC=0.77; for the high noise data, a standard deviation of the Gaussian filter of 3.6mm, and the threshold of 38.5 to achieve the maximum mean DSC=0.73.

For the thresholding, the variations in the DSC values between noise realizations were relatively small with a standard deviation of 0.01 for both noise levels. The segmentation accuracy was limited with the maximum mean DSCs over 50 noise realizations equal to 0.77 and 0.73 for the standard and high noise data, compared to the mean DSCs of 0.91 and 0.88 using the proposed method with the alternating scheme. Moreover, the ROI maps of the segmented myocardium exhibited jagged boundaries and discontinuities at the perfusion defect. These shortcomings likely result from the fact that the thresholding only depended on the intensity contrast between the myocardium and the remaining regions. However, the contrast locally varied as a result of statistical noise, the presence of perfusion defects, and PVEs.

The proposed model-based method resolved the problem of jagged boundaries and disconnected myocardium due to the smoothness imposed by the geometry model, which, by its nature, produces smooth and continuous myocardial surfaces. In addition, the prior used prior also encourages uniform wall thicknesses. In addition, the modeling of the resolution and noise in the image formation process might have contributed to the greatly improved segmentation accuracy. However, the model-based method was more sensitive to noise than the thresholding in terms of

LV segmentation, as indicated by the larger standard deviations of the DSC with the high noise data. The variability is inherent in the proposed model-based method with myocardial perfusion SPECT and PET images due to the ill-posedness of the reconstruction problem.

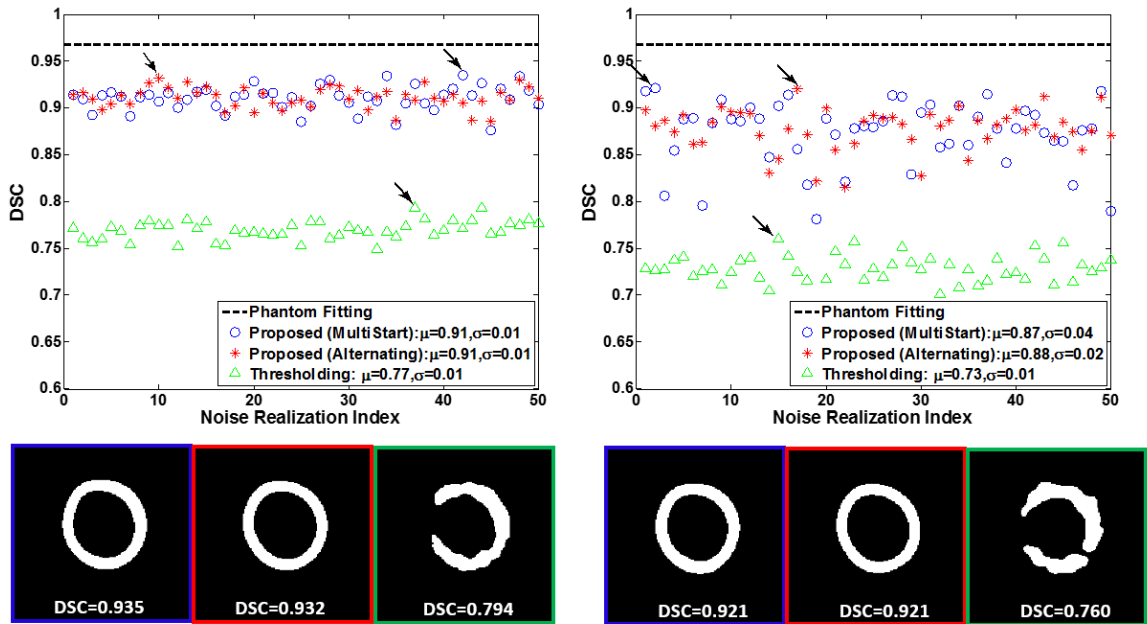


Figure 5-5. Evaluation of the estimated geometry model parameters in terms of LV segmentation accuracy. The top row compares the DSCs of 50 noise realizations using different methods. The bottom row shows the segmented myocardium masks of the maximum DSCs, as pointed by the arrows. The left and right columns correspond to the standard and high noise data with FBP reconstruction.

5.4 Estimation of the Mid-Myocardial Surface

Figure 5-7 compares the errors in the estimates of the endocardial radius, wall thickness, and mid-myocardial radius, which was calculated as the endocardial radius plus half the wall thickness. The means and standard deviations were computed from on 50 noise realizations and using the MultiStart method or the proposed group-wise alternating optimization scheme.

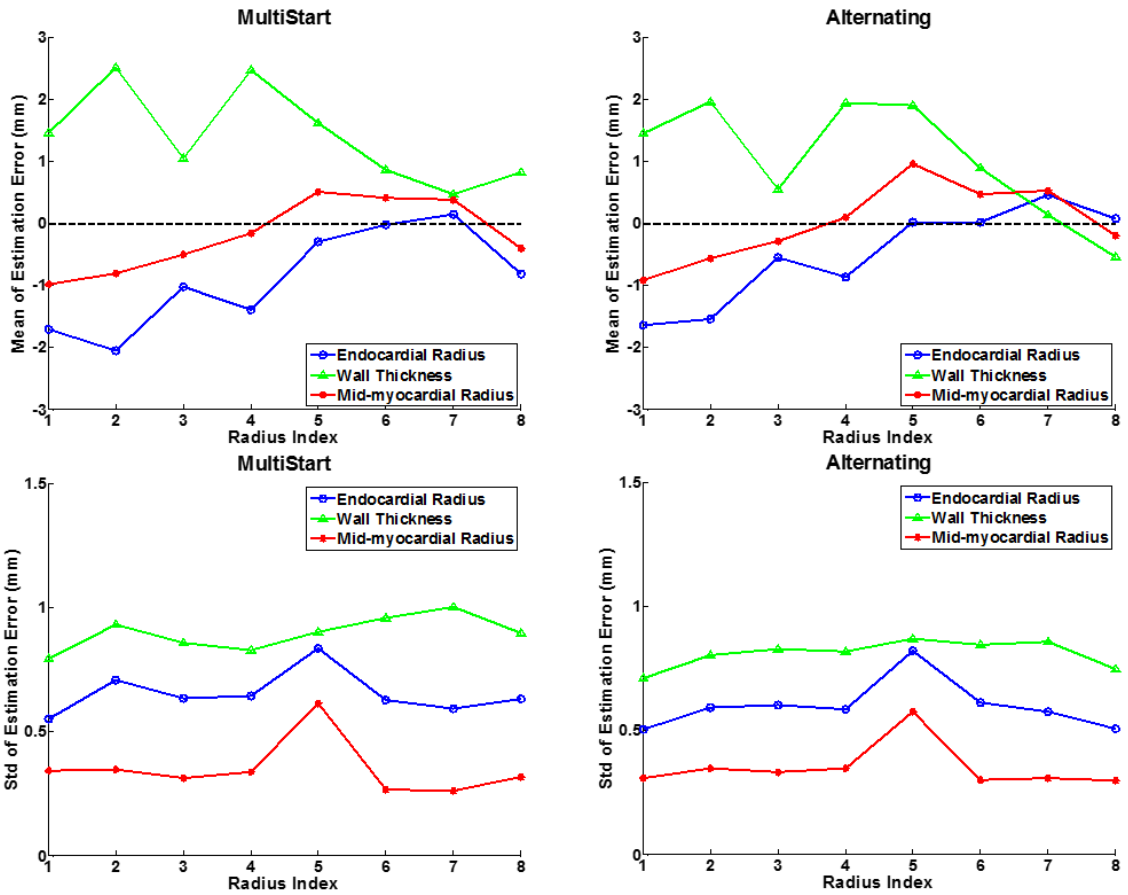


Figure 5-6. The means and standard deviations of the estimated endocardial radius, wall thickness and mid-myocardial radius parameters plotted versus the radial position along around the myocardium. These were calculated from 50 FBP reconstructed noise realizations at the standard noise level. The left and right columns correspond to the MultiStart and alternating methods, respectively.

The results using the two optimization methods were comparable for the standard noise data. The endocardial radius tended to be underestimated while the wall thickness tended to be overestimated. These opposite biases tended to be canceled out for the estimated mid-myocardial radius. The mean of estimation errors averaged over the eight radii were -0.51mm for the endocardial radius, 1.03mm for the wall thickness, and 0.01mm for the mid-myocardial radius using the alternating method. The standard deviations of the estimation errors averaged over the radii were 0.60mm for the endocardial radius, 0.81mm for the wall thickness and 0.35mm for the

mid-myocardial radius. The estimation accuracy and precision of the mid-myocardial radius was significantly improved compared to the other two parameters. This implies that the position of the mid-myocardial surface can be more reliably estimated than positions of the endo- and epi-cardial surfaces. Therefore, it is better to use the mid-myocardial surface to assess wall motion rather than the other two surfaces.

Note that the estimates of the endocardial and mid-myocardial radii exhibited larger variations at the abnormally perfused segment, but the larger variations were not apparent in the estimates of the wall thickness. The larger errors in the former could have resulted from the lower counts, and thus higher noise, in the abnormal segment; the latter might be attributed to the uniform-thickness prior.

It was shown that the initial wall thickness had a strong influence on the optimized thickness obtained using the proposed alternating scheme. It is interesting to investigate whether the optimized mid-myocardial radius is sensitive to the initial thickness. Figure 5-8 shows the estimates of the mid-myocardial radius for the group-wise alternating optimization with three different initial wall thicknesses.

The differences in the initial thicknesses used in the alternating method did not obviously affect the precision of the estimates of the mid-myocardial radius. However, consistent deviations were introduced in the estimated mean values. A 2.0mm increase in the initial wall thickness roughly yielded a 0.2mm decrease in the estimated value of the mid-myocardial radius. The change of the latter was significantly smaller than that of the former, implying that the estimation of the mid-myocardial surface was insensitive to the initial wall thickness. Therefore, it is reasonable to select only one value of the wall thickness from a reasonable range to initialize the alternating optimization when the task is estimating the mid-myocardial surface.

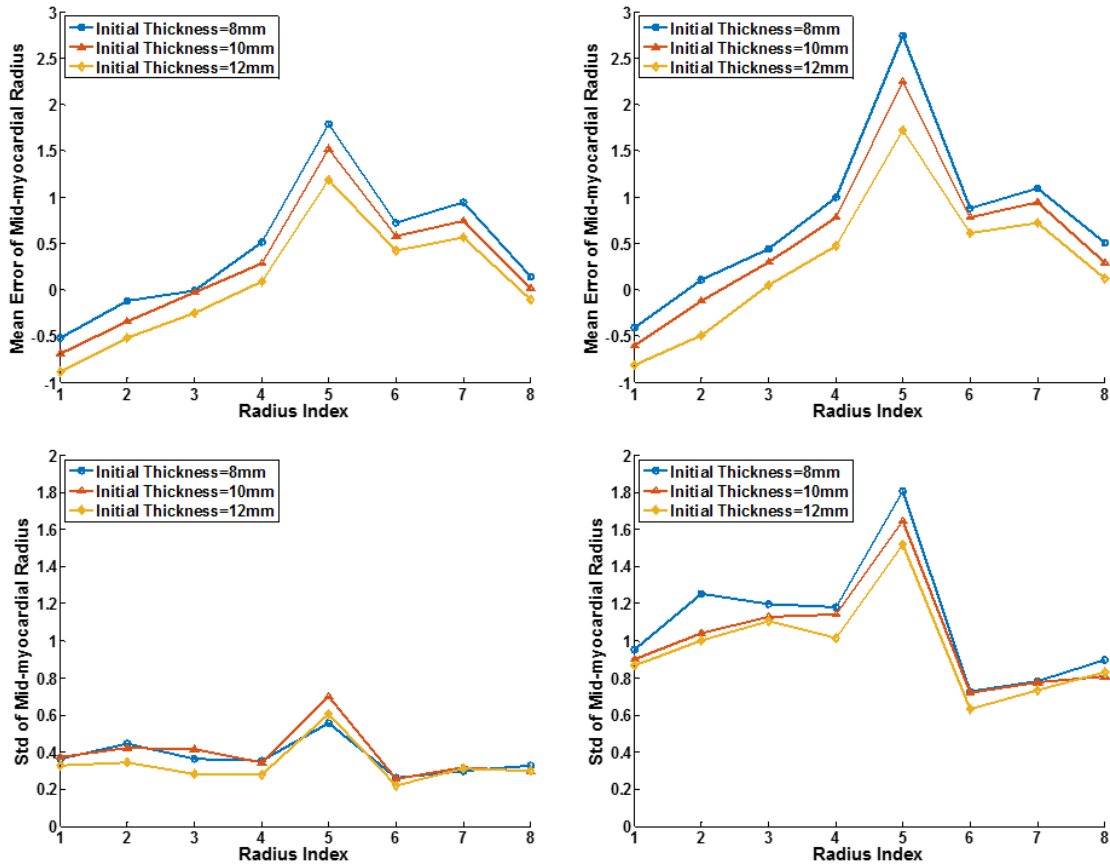


Figure 5-7. Means (top row) and standard deviations (bottom row) of the mid-myocardial radius estimates as a function of the radial position. The estimates were obtained using the proposed alternating optimization scheme with different initial thicknesses. The left and right columns correspond to the standard and high noise data, respectively.

Figure 5-9 compares the estimates of the mid-myocardial radius from the FBP reconstructed short-axis images using the proposed method with the alternating optimization scheme and the other three methods (*RadialCOM*, *MaxIntensity*, and *RadialFitting*), which are described in Section 3.6.5 in Chapter 3. The RMSEs averaged over the radii are given in Table 5-3.

RadialCOM assumed that the center of mass (COM) of the radial profile was at the mid-myocardial point. However, this assumption was compromised by a number of factors. First, the higher activity concentration in the blood pool than the background would tend to shift the COM

toward the center of the LV, which would result in underestimation of the mid-myocardial radii. However, this does not explain the overestimation for the smaller radii (the left part of Figure 5-9a). A second factor likely to impact the estimates for the smaller radii is that PVEs in the circumferential direction could potentially change the COM in the radial direction, especially given the elliptical shape of the short-axis LV. Consequently, the spillover of counts from the myocardium increased the counts in the blood pool more than in the background for these radial profiles from larger radii, leading to underestimation of the mid-myocardial radius; the effect was opposite for the radial profiles with smaller radii and thus resulted in the overestimated mid-myocardial radii.

The MaxIntensity method assumed that the pixel with the maximum intensity along the radial profile is the location of the mid-myocardial point. If we only consider PVE in the radial direction and the spill-out from the myocardium, this method makes sense since the mid-myocardium is the least affected by PVEs and thus corresponds to the highest intensity. However, this underlying hypothesis is affected by a number of factors, such as the presence of noise, and PVE in the circumferential direction along with the elliptical shape of the LV. In addition, the higher activity concentration in the blood pool would produce more spill-in of counts into the myocardium than the background, which might also alter the position of the maximum intensity point.

The RadialFitting modeled the differences in the activity concentration in the blood pool and the background in 1D. In addition, it compensated for PVE along the radial profile by modeling the 1D system PSF. As expected, *RadialFitting* was more accurate than the aforementioned two methods in estimating the mid-myocardial radius. However, it is unlikely that 1D resolution modeling can completely account for the effects of 2D blurring in the simulated short-axis image, especially when the myocardium is not rotationally invariant.

The proposed method improved upon the RadialFitting method by including 2D resolution modeling. In addition to the resulting improved accuracy, the model-based method was more robust to images noise and perfusion defects, as indicated by the significantly smaller error bars. The robustness mainly stemmed from the fitting based on the entire image and the thickness prior. By contrast, the RadialCOM and RadialFitting methods used each radial profile independently to estimate the mid-myocardial radius; the *MaxIntensity* method relied on the values of individual pixels along each profile independently, although a geometric constraint was introduced to encourage smaller variations between neighboring radii.

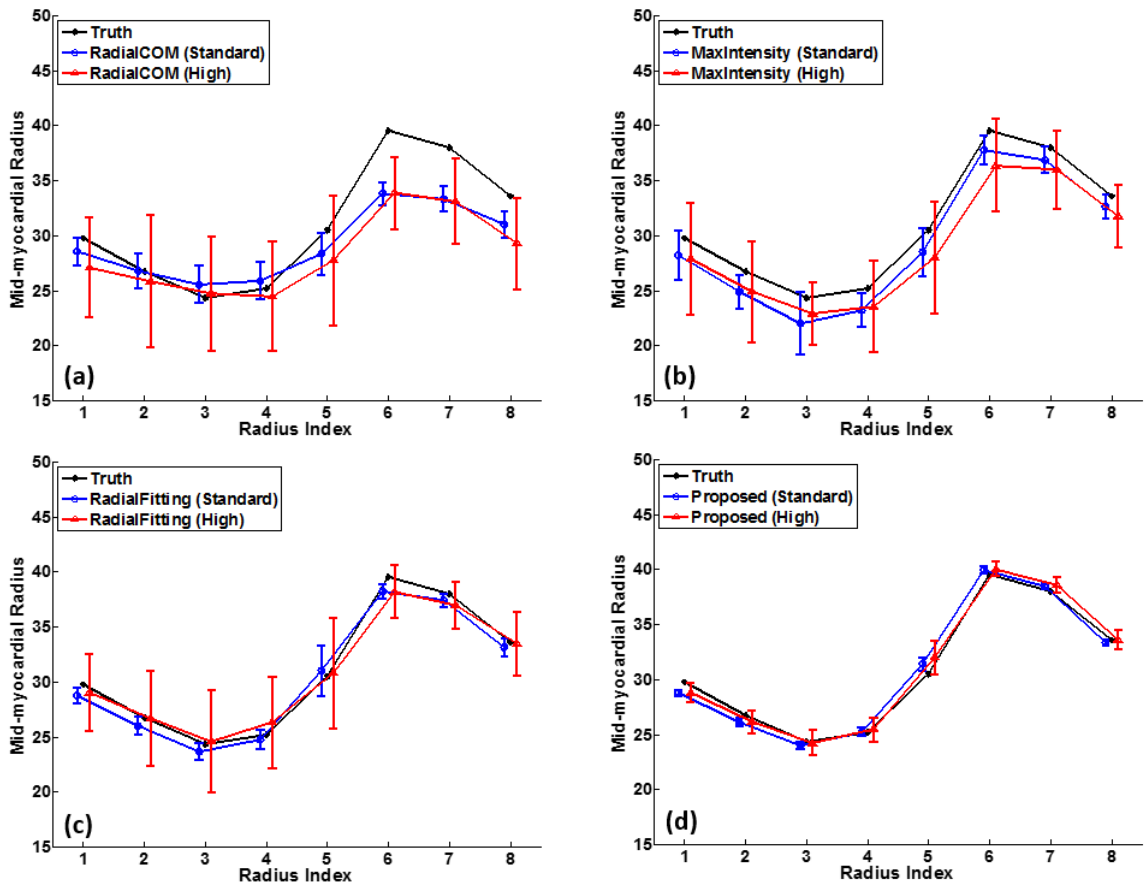


Figure 5-8. Estimation of the mid-myocardial radius based on 50 FBP reconstructed noise realizations at the standard noise and high noise levels.

Figure 5-10 displays similar results estimated from OS-EM reconstructed images, which included resolution compensation in the reconstruction. The regularization parameter $\beta=0.002$ and the initial wall thickness =10.0mm were used for the proposed method. The errors are compared in Table 5-2. *RadialCOM* yielded smaller estimation errors for OS-EM than for FBP. This mainly resulted from the improved spatial resolution with OS-EM. *RadialFitting* and the proposed model-based method both resulted in larger estimation errors for OS-EM than for FBP. This can be attributed to the less accurate modeling of resolution and noise in the image formation process, as revealed in Chapter 4. For either reconstruction method, the proposed method produced the smallest errors in the estimation of the mid-myocardial radii.

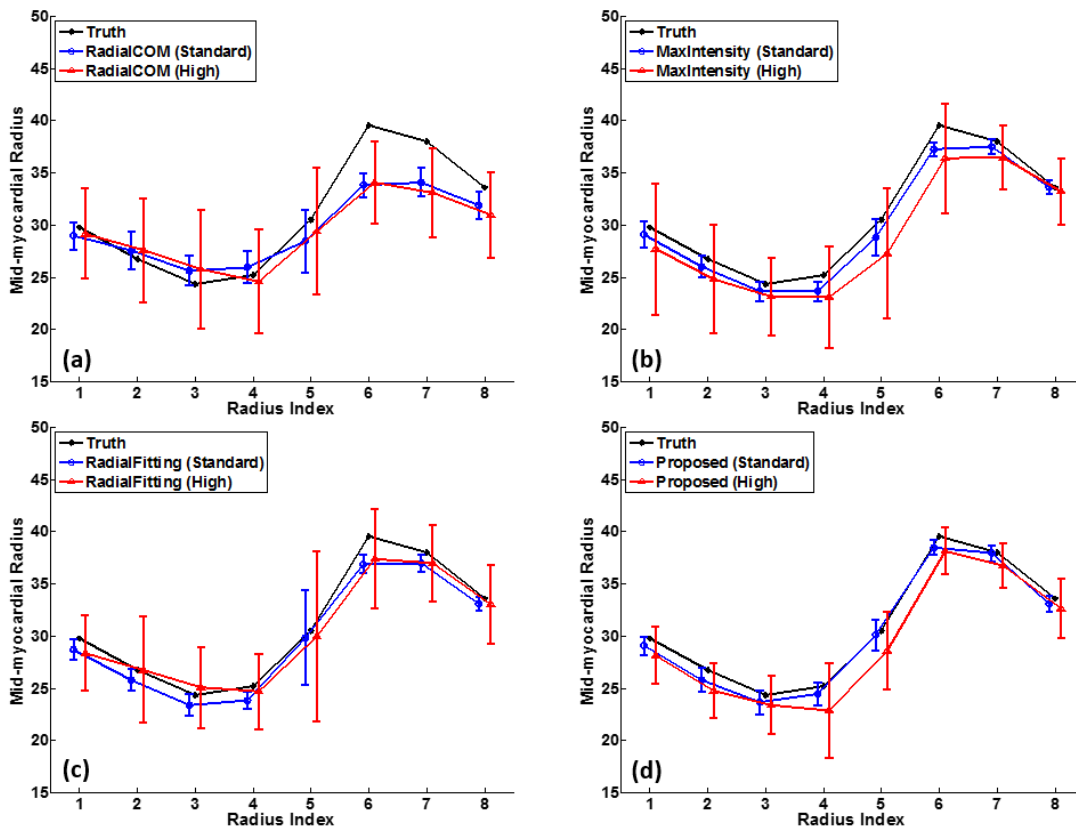


Figure 5-9. Estimation of the mid-myocardial radius based on 50 OS-EM reconstructed noise realizations at the standard and high noise levels.

Table 5-3. The averaged root mean square error ($\mu RMSE$) of estimated mid-myocardial radius parameters with reference to the phantom fitting truth.

		RadialCOM	MaxIntensity	RadialFitting	Proposed
FBP	Standard Noise	2.94	1.93	1.24	0.64
	High Noise	5.82	4.16	3.70	1.18
OS-EM	Standard Noise	2.86	1.50	1.91	1.21
	High Noise	5.53	5.10	4.65	3.33

5.5 Efficacy of Partial Volume Compensation

Figure 5-11 shows the restored myocardial segmental activities and corresponding images using the proposed model-based reconstruction method with the group-wise alternating optimization scheme. Also shown are images from the deconvolution-based and ROI-based PVC methods, which are described in Section 3.6.6. The segmental activities were computed as the mean of the resulting images within the true segment ROIs.

The deconvolution-based PVC method significantly improved the absolute quantification of myocardial activities in comparison with the original FBP reconstructed images, resulting in an approximate 50% reduction of the mean square error ($\mu RMSE$). The model-based method further reduced $\mu RMSE$ nearly by half while maintaining comparable estimation precision. Note that neither of the methods required ROIs defined from coregistered contrast-enhanced anatomical images.

The ROI-based PVC method using the true ROIs yielded the smallest estimation errors among these methods. This method was also applied using the estimated ROIs from the proposed method. The resulting estimation errors were slightly smaller than with the model-based method. The ROI-based PVC method treated the entire myocardium as one ROI and thus did not compensate for PVEs within the region, as revealed by the overestimated activity concentration in the abnormal segment; the model-based method divided the myocardium into eight segments and

estimated the segmental activity concentrations, and thus had the possibility of reducing PVEs within the myocardium, at least to the extent that defect boundaries are aligned with the segmental boundaries..

The model-based method estimated regional mean activities and generated piece-wise uniform images. The perfusion defect can be easily distinguished in the resulting model images. The ROI-based and deconvolution-based PVC methods estimated individual pixel values and thus preserved more detailed activity distribution.

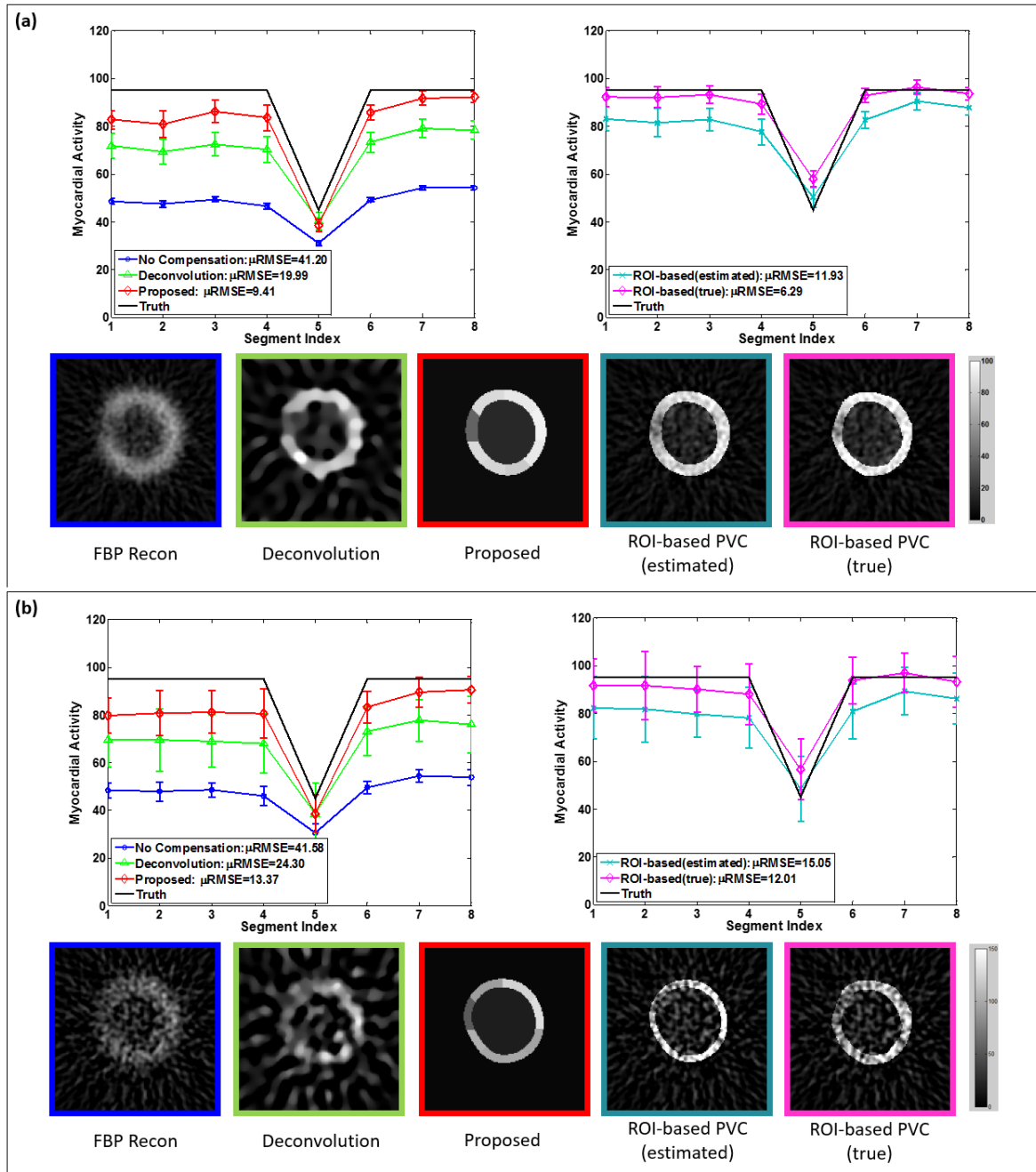


Figure 5-10. Graphs and images comparing the efficacy of PVC using the proposed method and deconvolution-based and ROI-based PVC methods. The results were based on FBP reconstruction of the (a) standard and (b) high noise data. In each of these two sub-figures, the top row shows the segmental mean activities of PVE-compensated images using the true segmented ROIs, where the error bars represent the standard deviations over 50 noise realizations; the bottom row shows the images from the 50th noise realization using different methods, as indicated by the same color of the error bars and the square enclosing the image.

5.6 Discussion

The proposed method greatly improved the accuracy of LV segmentation compared to the simple intensity thresholding but suffered high variability between noise realizations. Functional assessment of myocardial perfusion images usually depends on segmentation of multiple gated images. For example, the cavity volumes at end-systole and end-diastole are subtracted to estimate the ejection fraction. Consistent biases could cancel out, but the variability might significantly increase. Therefore, it might be necessary to trade estimation accuracy for improved stability and consistency between different cardiac phases. One previously-proposed method assumed a uniform 10mm myocardial wall in the end-diastole frame and scaled the predefined thickness to estimate the thicknesses of other frames based on the wall thickening percentage, which was calculated using the first harmonic of the Fourier analysis of the time-activity curves throughout the cardiac cycle (Cooke, Garcia et al. 1994; Faber, Cooke et al. 1999). Another method assumed a 12mm wall thickness for the gating interval that had the median of the maximal count along radial profiles (Liu, Sinusas et al. 2005). The predefined thickness was scaled for other gating intervals based on the ratio of the maximal counts. Similar techniques might be incorporated into the proposed model-based method.

The proposed method was compared to the deconvolution-based PVC method in terms of accuracy of the myocardial activity concentration estimates. Neither of the two methods requires predefined ROIs, but there is a major difference between them. The deconvolution-based PVC method makes no assumption about the shape of the myocardium and uses only pixel values and the resolution and noise statistics of the images. The proposed method incorporates detailed information about the LV shape and uses a much smaller number of parameters. For instance, the deconvolution-based method suppressed noise amplification using an image-based regularization term that penalizes large total variations in voxel values in the resulting image, while the proposed method implicitly controlled noise using a physiologically realistic LV activity distribution model

that produces piece-wise uniform images. Furthermore, the proposed method modeled the LV anatomical structure in the geometry model as and incorporated a thickness prior. The difference might have resulted in the superior performance of the proposed method. On the other hand, the proposed method was also compared to an ROI-based PVC method using true ROIs. The model-based method was modestly inferior, likely due to the lack of exact anatomical information. However, the comparison did not consider that the registration and segmentation errors likely to be present in practice when estimating ROIs from anatomical images. The results of the comparison would be fairer, and thus more definitive if these errors were taken into account.

It was efficient to assess the feasibility and effectiveness of the proposed model-based method using simulated short-axis images. However, some important issues absent in the 2D comparison should be investigated before deciding on whether to investigate the method clinically. For instance, it is more complicated to model the LV geometry and activity distribution in 3D myocardial perfusion images. Furthermore, the greatly increased number of model parameters will make the optimization more vulnerable to local minima and substantially increase the computational intensity requirements. In the next chapter, we will show some preliminary results based on simulated 3D myocardial perfusion SPECT images.

6. Results and Discussion (3D)

In this chapter, we first quantified the accuracy of the proposed 3D geometry model in representing the LV structure of the XCAT phantom. After that, the simulated noisy 3D myocardial perfusion SPECT image was first fitted slice-by-slice using the method described in the previous chapters. The estimated parameters were then used to initialize fully 3D fitting of the image; in other words, the geometry and activity distribution models described the entire LV instead of a short-axis slice, and the resolution model described the 3D blurring effects in MPI. The results were compared and analyzed subsequently.

6.1 Geometry Model Evaluation

The idea of this section is to quantify the disagreement in the true LV shape of the XCAT phantom and the shape estimated by the geometry model. The LV shape of the phantom was represented by the binary VOI mask image of the myocardium, which described whether a voxel was in the myocardium or not. Short-axis slices not containing any myocardium were excluded from the mask image to identify the LV extent along the axis. A few of the most basal slices were also excluded for simplicity because they did not exhibit the donut-like shape of the geometry model. The LS difference between the phantom-based mask image and the mask image generated from the 3D geometry model was minimized by seeking for the optimal model parameters.

Figure 6-2 shows three short-axis myocardial mask images obtained from fitting the geometry model to the phantom truth; three horizontal long-axis mask images are also displayed in Figure 6-3. The proposed geometry model qualitatively modeled the shape of XCAT-based LV structure, except that the resulting endo- and epi-cardial surfaces had increased smoothness than the phantom truth. On the other hand, the overall DSC of the fitted 3D myocardium mask was approximately 0.95, implying that the proposed geometry model is able to model the shape of the

myocardium very well. The orientation and the involved interpolation resulted in the less smooth surfaces in the phantom mask; otherwise, the overall DSC might be larger than 0.95.

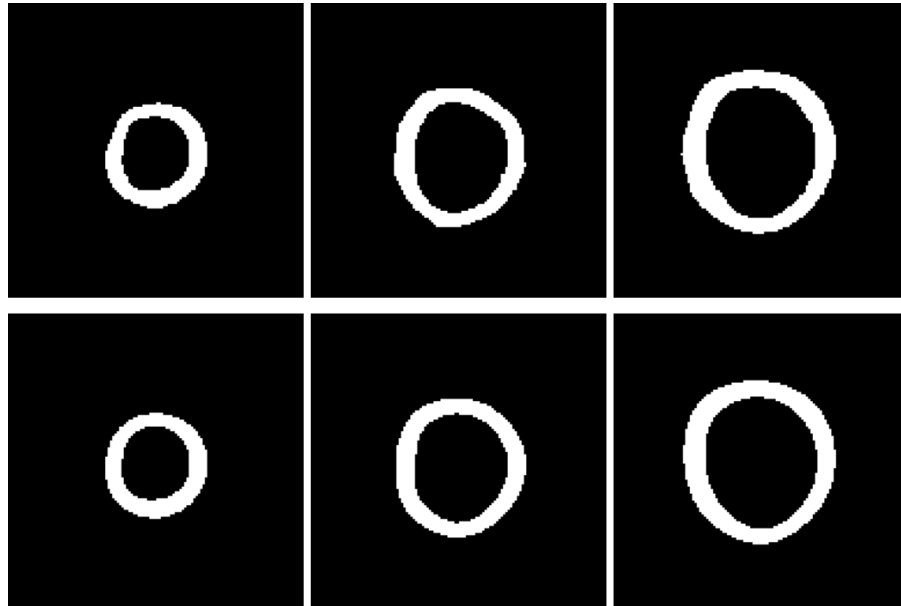


Figure 6-1. Short axis myocardial mask images obtained from fitting the geometry model to the phantom. The top and bottom rows are the phantom truth and the fitting results, respectively.

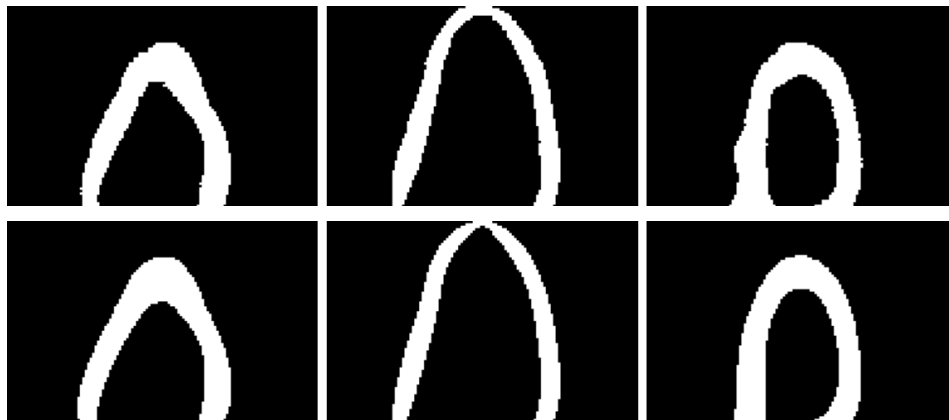


Figure 6-2. Horizontal long axis myocardial mask images obtained from fitting the geometry model to the phantom. The top and bottom rows are the phantom truth and the fitting results, respectively.

6.2 Slice-by-Slice Fitting

The FBP reconstructed 3D myocardial perfusion image was reoriented and truncated in the same way as in the previous section. The resulting noisy image was fitted slice-by-slice using the method described in the previous chapters: for a fixed initial estimate of the wall thickness, the remaining parameters were estimated from each short-axis slice using the method described in Section 3.5.3 of Chapter 3. Then the entire set of initial parameters of each slice was optimized separately using the group-wise alternating scheme. The slice-by-slice fitting results were used to generate a 3D initial estimate. The process was repeated for multiple initial wall thicknesses to determine the one resulting in the smallest value of the objective function after fully 3D fitting.

The most apical slices without the blood pool were processed differently in the slice-by-slice fitting. First, the geometry model was modified to use only eight radius parameters defining the epicardial contour, and the activity distribution model was modified to use only two parameters defining activity concentrations in the myocardium, which was assumed to have a uniform activity concentration, and the background. In addition, the uniform-thickness prior was replaced by a prior that penalized variance of the epicardial radii. The method for obtaining initial estimates was also different for these apical slices: we looked for the epicardial radius that maximized the mean activity in a circular myocardium ROI. The initial activity parameters of the myocardium and the background for each slice were estimated as the mean activities in the resulting ROI. The alternating optimization scheme divided the model parameters into the geometry group and the activity group and optimized the epicardial radii first. Note that those apical slices without the blood pool were manually identified in advance based on the reoriented phantom image, as were other apical slices and the basal and mid-cavity slices. Also, note that only one empirically chosen value of the regularization parameter ($\beta=0.1$) was used for simplicity for all the short-axis slices.

The standard deviation of the Gaussian resolution kernel was estimated for each short-axis slice by minimizing the LS difference between the slice from the noise-free FBP reconstruction

and the corresponding Gaussian-blurred phantom slice. The 3D Gaussian kernel was similarly obtained based on the noise-free reconstruction in the VOI used in the previous sections. Figure 6-6 displays the FWHMs of the 2D kernels and the 3D kernel.

The FWHM differences between the 2D and 3D kernels were small for the mid-cavity slices but gradually increased toward the apex and base. In particular, the slice-based FWHMs were significantly larger than the 3D FWHM for the apical and apex slices. The resolution blurring occurred not only within short-axis slices but also between slices in the 3D myocardial perfusion SPECT simulation. The spill-in and spill-out of activities were comparable for the mid-cavity slices due to their similarity in geometry and activity distribution, resulting in essentially 2D blurring and thus the similarity of the 2D and 3D FWHMs. However, this is not the case in the apical region as the size of the LV was changing, resulting in different spill-in and spill-out effects. Consequently, the FWHMs of slice-based kernels were significantly overestimated to compensate for the inter-slice blurring effect. In the slice-by-slice fitting, all the slices used the same 2D Gaussian resolution kernel with the FWHM equal to that of the 3D kernel.

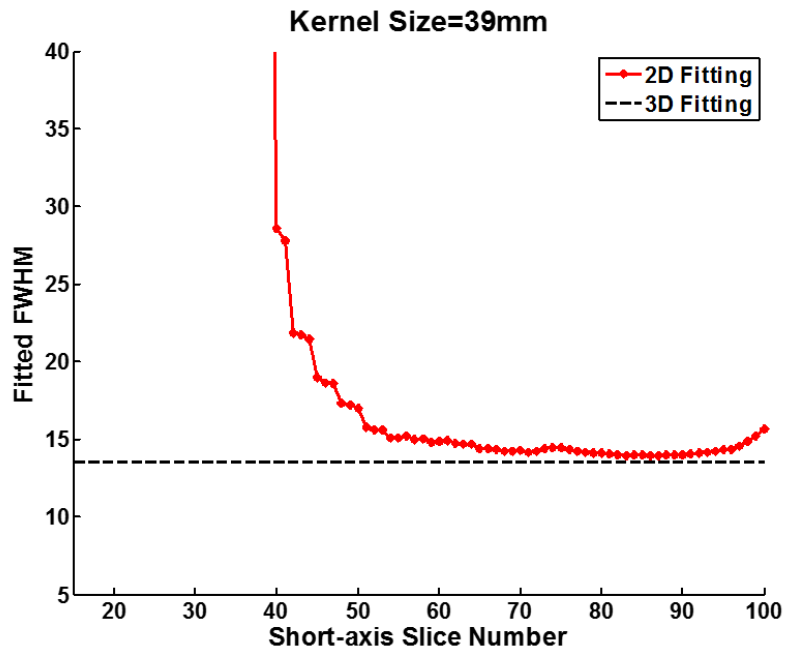


Figure 6-3. Standard deviations of the fitted Gaussian resolution kernels based on short-axis slices and the entire image volume. The smallest slice index corresponds to the first apex slice.

As revealed later, some shortcomings are associated with the slice-by-slice fitting method. The fully 3D fitting presented in the next section has the potential to overcome some of the shortcomings due to its use of more accurate resolution and geometry models.

6.3 Fully 3D Fitting

The fully 3D fitting method used 3D geometry and activity distribution models to depict the tracer uptake in the entire LV region instead of one short-axis slice. A reoriented 3D myocardial perfusion image was generated from each set of model parameters. In addition, the method modeled the resolution blurring effects in 3D instead of in each short-axis slice.

One important concern about the fully 3D fitting is the large amount of computational resources required. Although the resolution modeling was approximated with a spatially invariant 3D Gaussian kernel, the convolution between the myocardial model image and the kernel is still time-consuming, which was implemented in the spatial domain with MATLAB function *smooth3*. By contrast, the convolution time was insignificant in the 2D implementation. Because of the significant computational effort required for the 3D implementation, we investigated the trade-off between kernel size and computation time. Reducing the size of the Gaussian kernel can reduce computation time, but also decreases modeling accuracy; the kernel size was chosen to strike a good balance between accuracy and efficiency in the 3D implementation. Figure 6-10 (a) and (b) plot the time for one convolution and the MSE of the two blurred phantom images using the true and approximated resolution modeling a function of the kernel size, respectively. The MSE decreased at first and then remained relatively constant after the kernel size reached 27mm, but the convolution time grew rapidly with increased kernel size. In the fully 3D fitting, the kernel size was chosen to be 27mm in all three directions and the corresponding FWHM of the kernel was 14.19mm. As a result, the RMSE was 0.78 for voxels in the VOI for model fitting, smaller than the RMSE of 0.99 seen in the 2D implementation in Chapter 4. Thus, because resolution modeling is more accurate in 3D, the parameter estimates may be less biased with fully 3D fitting.

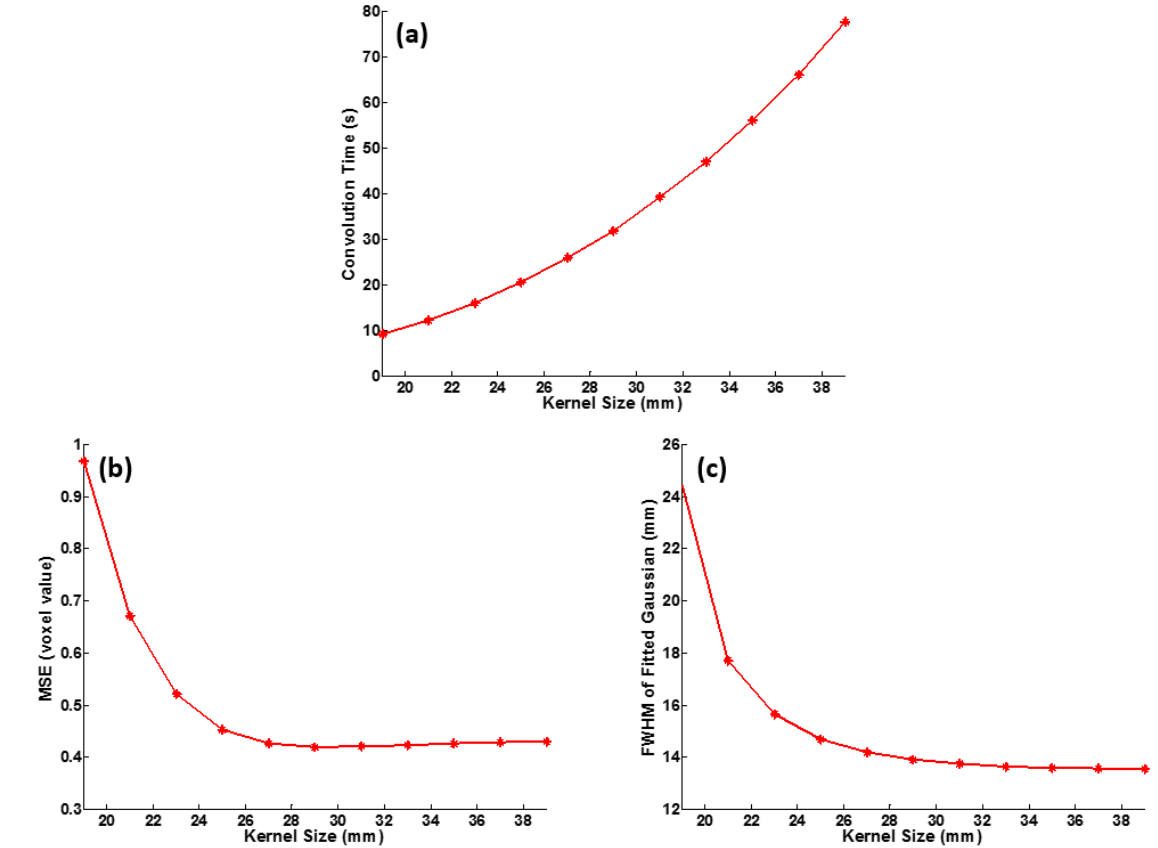


Figure 6-4. (a) The computation time for one convolution, (b) the MSE with the noise-free reconstruction, and (c) the FWHM of the fitted Gaussian function as a function of the Gaussian kernel size.

The regularization parameter was set to be 0.01 based on empirical observation. The fully 3D fitting method requires optimization of eleven sets of initial model parameters synthesized from the slice-by-slice fitting results based on the eleven thickness candidates, which ranged from 7.5mm to 12.5mm in 0.5mm increments. For each initial thickness, the 3D initial estimate obtained from the corresponding slice-by-slice fitting results was optimized using the group-wise alternating scheme. Figure 6-10 plots the resulting value of the objective function, the DSC of the segmented myocardium, and the mean value of optimized wall thicknesses as a function of the initial thicknesses. The objective function reached a minimum for an initial thickness of 9.5mm. The

corresponding optimized model parameters were regarded as the best parameter estimates for the fully 3D fitting procedure. The maximum DSC was obtained at the 9.0mm rather than the 9.5mm initial thickness, but the DSC difference was very small. In addition, the optimized thickness heavily depended on the initial thickness with an approximately linear relationship, just as was observed in Chapter 5.

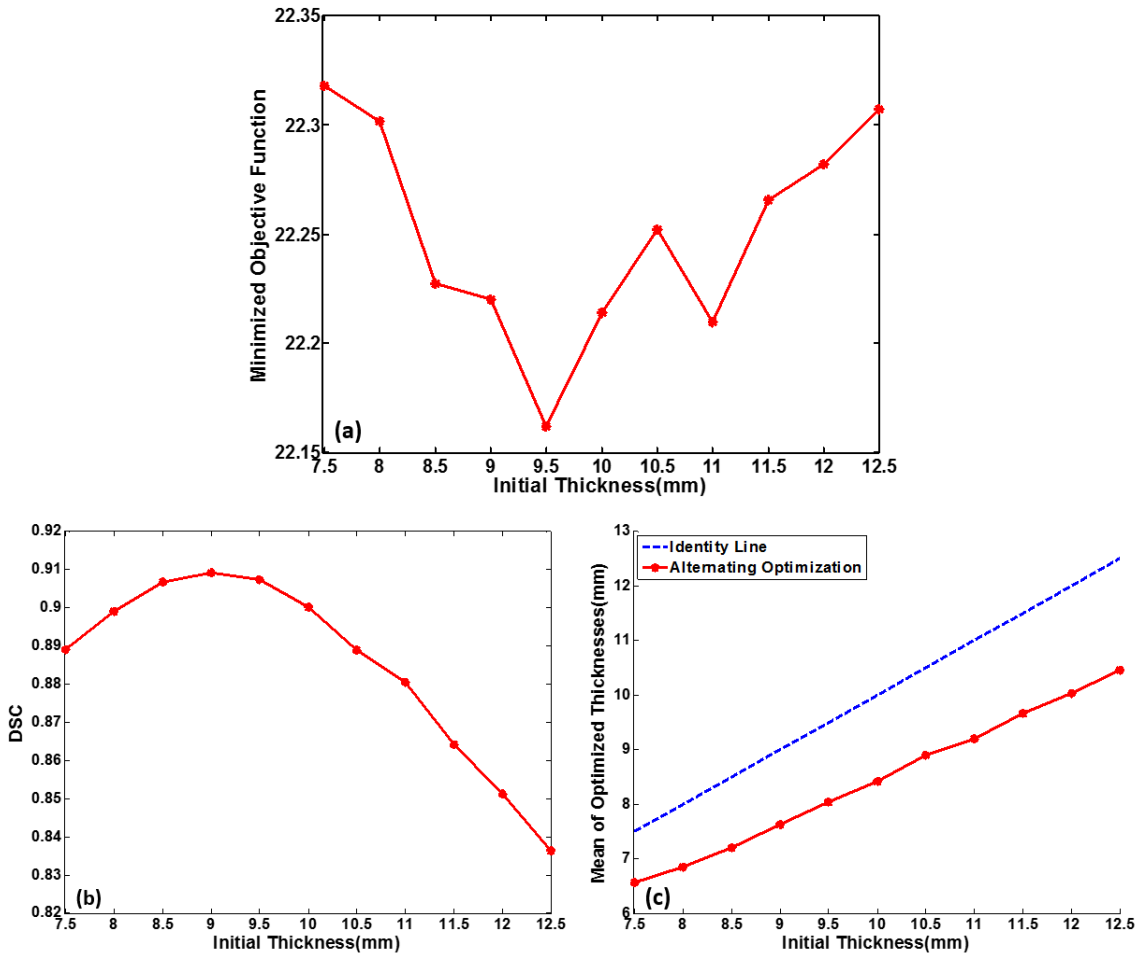


Figure 6-5. Initial Thickness refers to the thickness of the myocardial wall used to generate a 3D initial estimate in all cases. The subfigures are (a) the value of the objective function after the group-wise alternating optimization that was initialized with parameters estimated from slice-by-slice fitting using the indicated wall thickness, (b) the DSC of myocardium segmentation, and (c) the mean of optimized wall thickness parameters as a function of the initial thickness.

6.4 Myocardial Perfusion Images

Figure 6-6 shows example short-axis, vertical long-axis and horizontal long-axis slices of the myocardial perfusion images using different methods. The images corresponding to the initial wall thickness of 9.5mm were selected for the slice-by-slice fitting and the fully 3D fitting methods. *Phantom Fitting* refers to fit the geometry and activity distribution models to the phantom image by seeking for the optimal model parameters that minimize the LS difference between the phantom image and the myocardial model image generated from the parameters. The optimized model parameters were used as the reference for the slice-by-slice fitting and fully 3D fitting of the FBP reconstructed myocardial perfusion image. The FBP reconstructed image was also processed using the deconvolution-based PVC method described in Chapter 3.

Visual analysis of the long-axis images reveals two important limitations in the slice-by-slice fitting. First, the activity concentrations in the blood pool were increasingly overestimated for the apical slices toward the apex and the LV sizes were overestimated for these slices. The problems in the apical region likely originate from the use of 2D resolution modeling in short-axis slices. The spill-in of activity from the neighboring slices was so large that the activity distribution in the original slice was significantly distorted and the blood pool was not visible. The blood pool and the background region in the proximity of the LV had a comparable or even higher intensities than the myocardium, resulting in the overestimation of the LV size and the activity concentration in the blood pool. The distorted activity distribution poses a critical challenge to the proposed model-based reconstruction method that assumes a higher uptake in the myocardium. Second, the resulting endo- and epi-cardial surfaces were not smooth between short-axis slices; also, the activity concentrations in the blood pool and background did not continuously vary across slices. This is expected since the fitting was separately performed for each short-axis slice without constraints to encourage the smoothness and continuity in the axial direction. The fully 3D fitting refined the

slice-by-slice fitting results and resolved the problems in the apical region and the unsmoothness across slices.

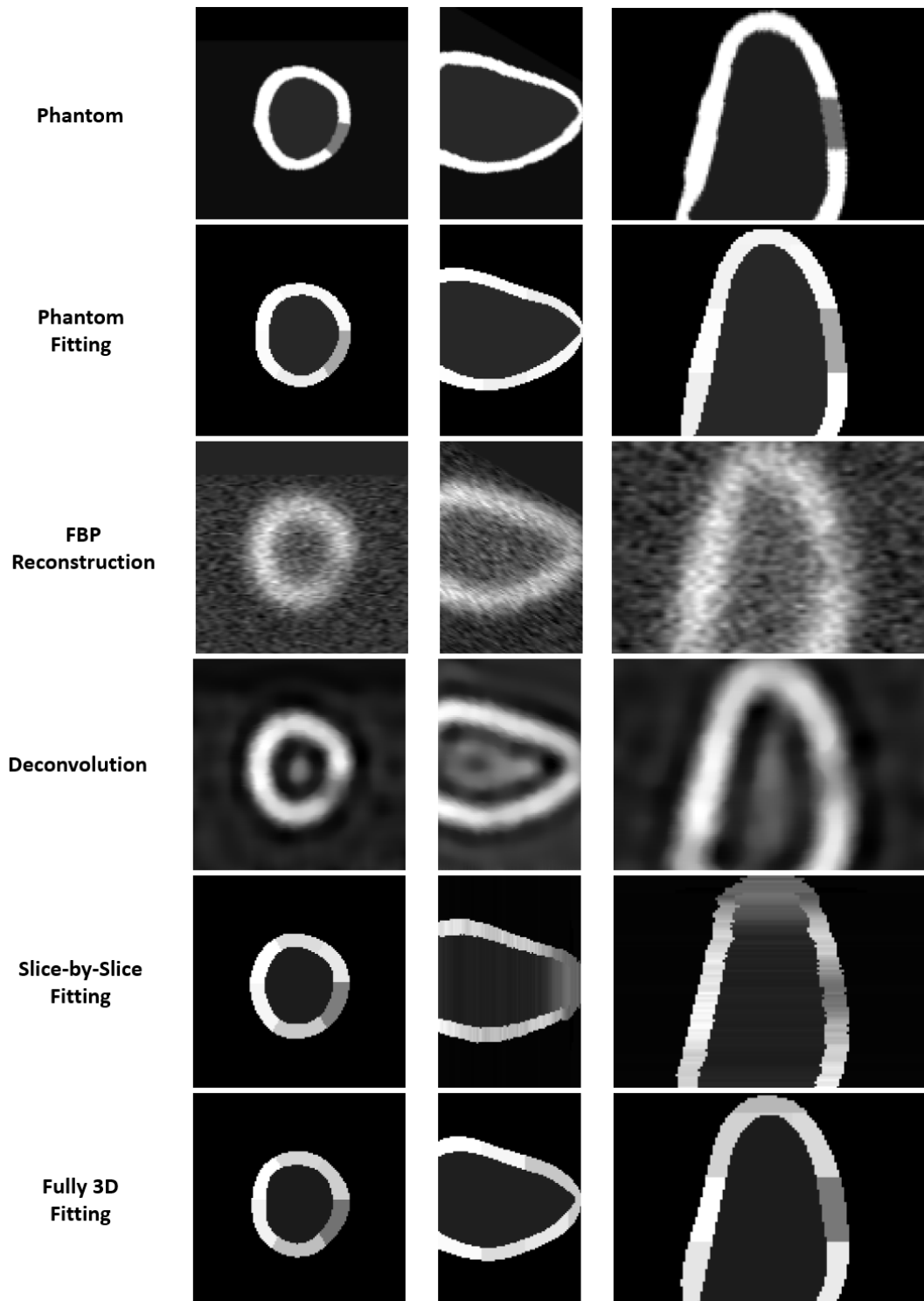


Figure 6-6. Example slices from short-axis, vertical long-axis and horizontal long-axis views using different methods.

6.5 Efficacy of LV Segmentation

Figure 6-7 shows the DSCs of segmented myocardium for each short-axis slice and each horizontal long-axis slice using different methods. The original FBP reconstructed image was also segmented using the thresholding method described in Chapter 3, which optimized the pre-filtering and the threshold to maximize the DSC. Note that the slice-based DSCs were smaller for the starting and ending slices. This mainly resulted from the relatively small myocardium in these slices that a small model mismatch could make a big difference in the DSCs.

For the slice-by-slice fitting, the DSCs of short-axis slices confirm the problems in the apical region, as observed in the long-axis slices in Figure 6-6. The overlap of myocardial voxels with the phantom truth was smaller for these slices. In particular, the DSCs were reduced to almost zero for two slices. We analyzed one of them in Figure 6-8. The model image was visually similar to the phantom image and the perfusion image with a hot region in the center. Nevertheless, the profiles reveal that the hot region corresponded to the blood pool rather than the myocardium; the myocardial activity concentration was significantly underestimated, even smaller than the activity of the background. It is difficult for the proposed method to resolve the blood pool in this case.

For the fully 3D fitting, the myocardium was accurately delineated with an overall DSC of about 0.91, larger than 0.84 from the slice-by-slice fitting. As revealed by the DSCs of short-axis slices in Figure 6-6a, the fully 3D fitting resulted in larger DSCs primarily in the apical region, implying that the fully 3D fitting resolved the problems resulting from 2D resolution modeling in the slice-by-slice fitting. However, some mid-cavity slices were more accurately segmented with the slice-by-slice fitting. The slice-by-slice geometry model, which used 82 short-axis slices to cover the LV, had a superior ability to describe regional geometry variations because it more finely sampled the LV structure. In addition, the DSC of the fully 3D fitting was considerably larger than the DSC (0.77) of the thresholding method and close to the DSC (0.94) of the phantom fitting, which represented the best performance achievable with the fully 3D fitting.

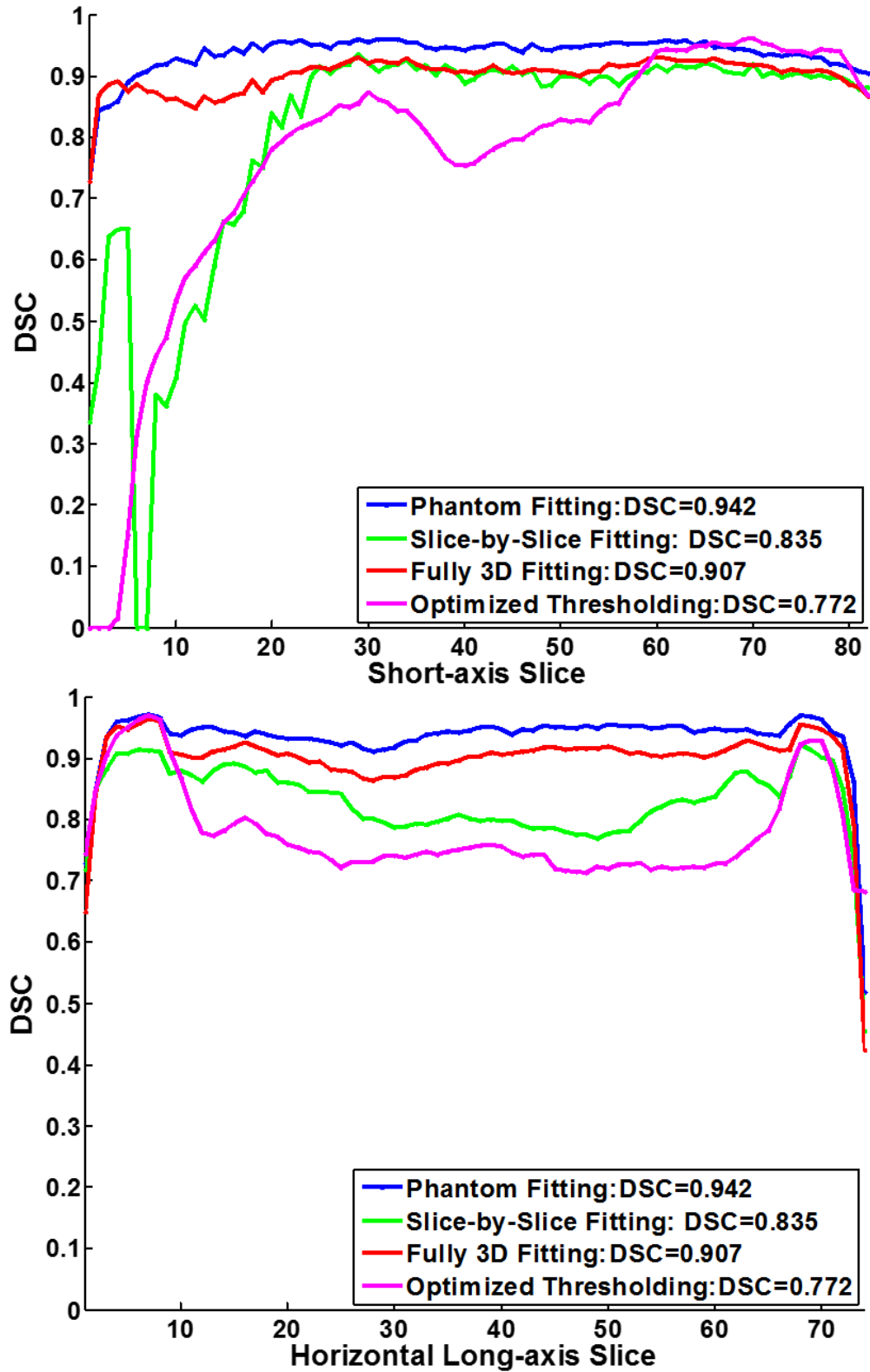


Figure 6-7. Comparison the DSCs of the segmented myocardium for various segmentation methods as a function of the short-axis slice number (top) and horizontal long-axis slice number (bottom).

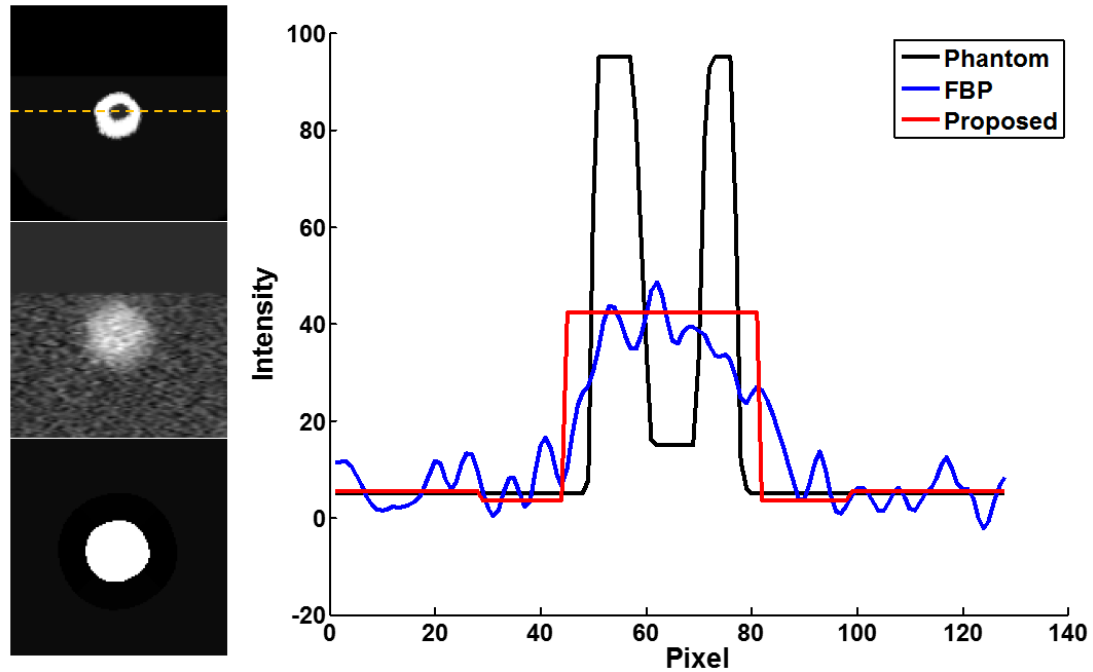


Figure 6-8. Comparison of the resulting model image to the phantom and FBP reconstruction of an apical slice.

6.6 Efficacy of PVC

Figure 6-9 shows the polar maps and the associated 17 myocardial segmental activity concentrations using different methods.

For the phantom fitting method, the perfusion defect could be easily identified in the polar map. Quantitative comparison of segmental activity concentrations reveals that the concentration was underestimated by 6.78% on average for the normal segments and overestimated by 37.01% for the abnormal segment. One possible source of this disagreement is blurring of the phantom image due to interpolation during the reorientation of the transaxial phantom image, which reduced the values of myocardial voxels at the boundaries. The overestimation in the defect likely resulted from the fact that the defect's extent was smaller than the corresponding segment of the activity distribution model. Consequently, a small fraction of the normal myocardium was included in the abnormal segment during the model fitting. In addition, the errors of activity estimation could also

be related to the mismatch between the geometry model and the phantom geometry. This mismatch would result in biased activity estimates.

As shown in the polar map for the slice-by-slice fitting method, the apex seems to be abnormally perfused due to PVEs at the thinner apex. However, the severity of the reduction in activity concentration visually appears greater than in the polar map of the original FBP reconstructed image. The slice-by-slice fitting method failed to recover the myocardial activity in the apical slices but effectively compensated for PVEs in the mid-cavity and basal slices. The different PVC performance resulted in the larger intensity contrast between the center and periphery of the polar map. The above explanation is validated by the quantitative comparison of segmental activity concentrations shown in Figure 6-9g.

The fully 3D fitting method improved the estimation of myocardial segmental activities compared to the slice-by-slice fitting method. In particular, the PVEs in the apical slices were compensated for to some extent, resulting in the reduced intensity differences compared to nearby normal segments. In addition, the activity estimates for the model-based method proposed here were more accurate than those for the deconvolution method, as shown in Figure 6-9g.

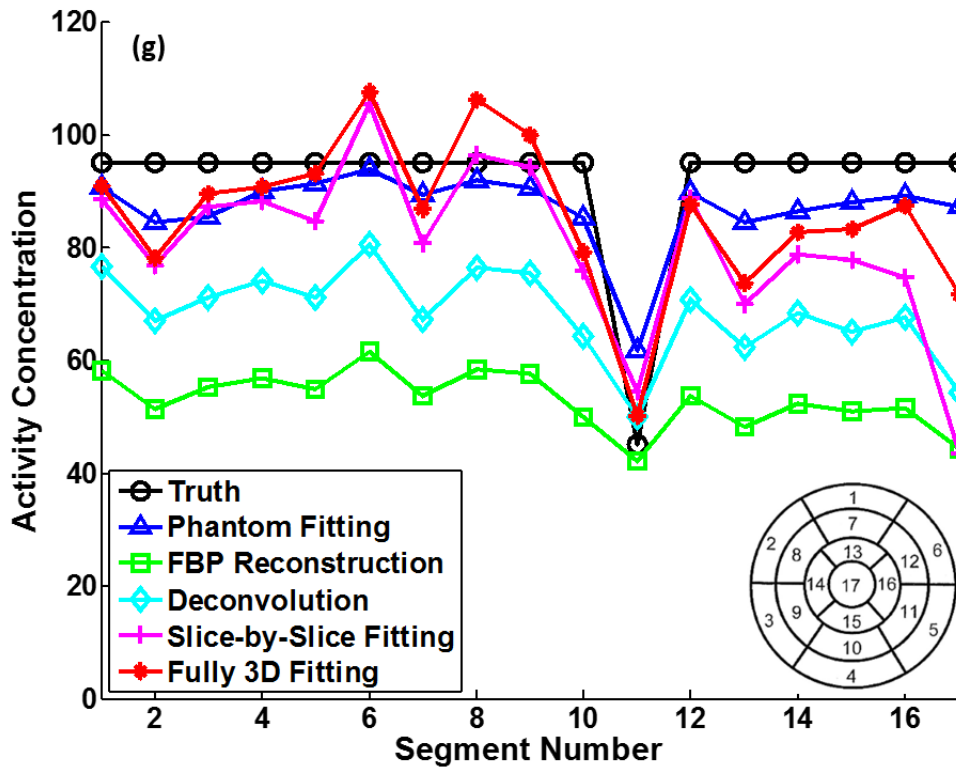
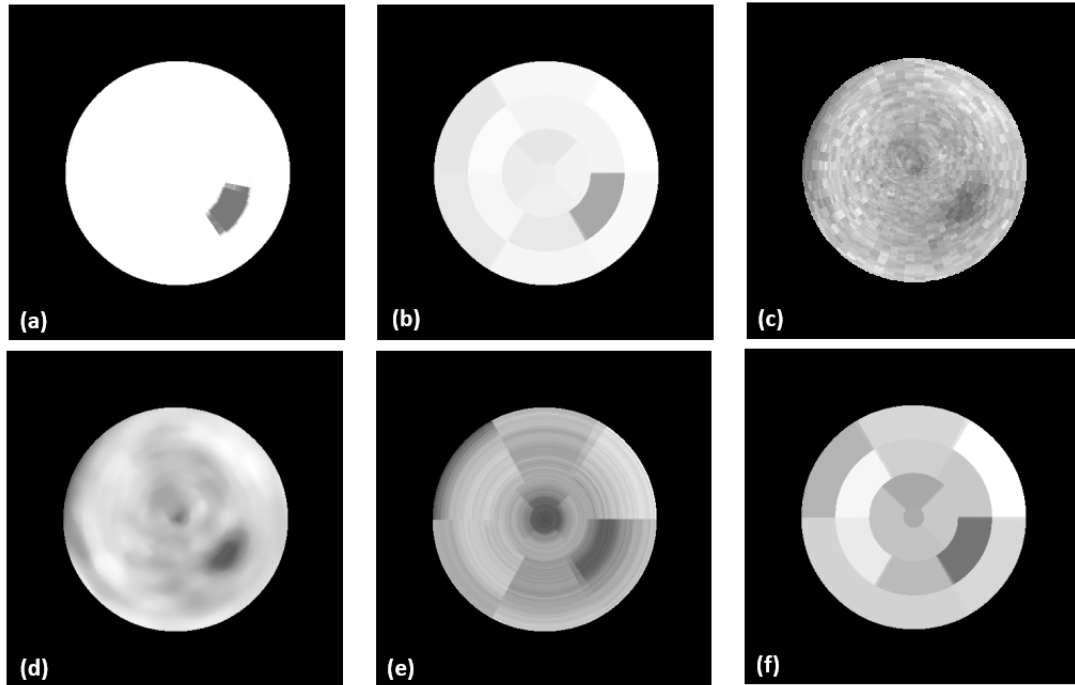


Figure 6-9 . Qualitative and quantitative comparison of the polar maps obtained using different methods: (a) Phantom; (b) Phantom fitting; (c) FBP reconstruction; (d) Deconvolution-based PVC; (e) Slice-by-slice fitting; (f) Fully 3D fitting; (g). The segmental activity concentrations are the means over these segmental ROIs in the polar maps for the methods in (c), (d) and (e).

6.7 Discussion

The above results demonstrated the feasibility and efficacy of the fully 3D implementation of the proposed method in segmenting the LV and estimating the segmental activity concentrations for myocardial perfusion images. One critical factor limiting the applicability of the proposed method is its high computational intensity. The fully 3D fitting took about four days from one initial estimate on a single core of an i7-2600 CPU running at 3.40 GHz and having a memory of 8.00GB. The efficiency might be enhanced from the following improvements.

The large matrix size of the model image ($128 \times 128 \times 128$) played an essential role in increasing computational requirements of the fully 3D fitting method. The voxel size used in the optimization was 1.0mm, comparable to that of high-resolution CT images but about four times smaller than that of realistic SPECT images. The main reason for using a small voxel size was to reduce the impact of errors in the voxelization of the object model. However, the resulting large matrix size dramatically increases to create the voxelized representation of the model, model the resolution, and perform the fitting, particularly as these steps are repeated for each trial set of model parameters during optimization. The choice of a suitable voxel size for these calculations is essential in reducing the computation requirements. It is possible that the computation time can be greatly reduced without evidently sacrificing the estimation accuracy.

The resolution modeling was the most computationally intensive operation in the evaluation of the objective function. The resolution modeling was implemented as the convolution of the model image and the Gaussian resolution kernel. The kernel size was optimized to save time without compromising the modeling accuracy. However, it is not necessary to convolve the whole image with the kernel for each trial set of parameters. For instance, only voxels in the myocardial ROI are subject to change when optimizing the group of segmental activity parameters. The resolution modeling of voxels in other regions could be computed once in advance by convolving the corresponding regional images with the kernel. Using the linearity of convolution, these

precalculated results could be added to the blurred version of each updated regional image of the myocardium to model the resolution blurring effect on the entire model image. In addition, since the myocardium is piece-wise uniform in the model image, the update of the myocardial region could be conducted on the basis of segments. On the other hand, the convolution can be implemented in the frequency domain using fast Fourier Transform techniques. These techniques might help shorten the time of resolution modeling.

In addition, the model fitting can be performed in a multiresolution manner to accelerate the convergence. In this approach, the myocardial model could be coarsely voxelized at first, and the parameters adjusted to fit the observed data. This would be faster because of the reduced computational requirements for convolution and voxelization of the model, and could be terminated under less strict criterion with regards to change in the objective function value. The parameters from the coarse fitting would then be used to initialize the fitting performed with smaller voxels. This process would be repeated for a predefined sequence of increasingly smaller voxel sizes.

Finally, the optimization method used in this work was not optimized. The model parameters were optimized by using a function *fmincon* in MATLAB with the interior-point algorithm, a general constrained optimization algorithm for nonlinear functions. The parameters that control the algorithm, such as the step size, the stopping criteria, and the ranges of parameters, were currently empirically chosen and not rigorously investigated. Closer attention to these might result in faster convergence and thus reduced computation time.

7. Summary and Future Work

7.1 Summary

This study developed and evaluated a model-based reconstruction method for myocardial perfusion SPECT and PET images that was designed to improve the accuracy of activity quantification and functional analysis without the use of high-resolution anatomical images.

The proposed method integrates prior information about the imaged object and the image formation process into a rigorous estimation framework that provides simultaneous left ventricle (LV) segmentation and partial volume compensation (PVC). Specifically, the myocardial perfusion image is characterized using an LV geometry model and an activity distribution model. The geometry model parameterizes the endocardial and epicardial surfaces with a set of sampling rays originating from the long axis of the LV. The intersection points of the rays and each surface are interpolated using cubic spline functions to generate continuous and smooth endo- and epi-cardial surfaces. The geometry model provides the flexibility to describe various levels of detail in the LV structure depending on the number of sampling rays. The proposed sampling scheme provides an accurate description of the LV geometry of the XCAT phantom, an anthropomorphic phantom based on b-spline surfaces defined from human images, using a relatively small number of sampling rays. The activity distribution model divides the myocardium into anatomically meaningful regions based on standardized segmental analysis and assumes homogeneous activity distributions in each segment as well as the blood pool and background regions. In addition, the proposed method models the resolution and noise properties of the image resulting from the imaging and reconstruction processes. Using the maximum likelihood criterion, the geometry and activity distribution models are fit to the observed data based on approximations to the noise statistics and image resolution described below. In the method, the model parameters are estimated directly from the images or projection data instead of estimating voxel membership in a volume-of-interest (VOI) or the true activity in a voxel, as in conventional segmentation and PVC methods. This significantly

reduces the number of unknowns to be estimated. When the model parameters are estimated directly from the projection data, noise approximations are not needed and voxel values are not estimated at all. The geometry parameters can be directly used to generate LV VOI masks such as those provided by conventional segmentation methods; the activity distribution parameters are PV compensated representations of the true activities due to the modeling of spatial resolution and constraints on homogeneous activity distributions in the myocardial segments. The activity parameters can be directly used to create polar maps for use in visual interpretation or in the automatic or semi-automatic scoring of defect severity and extent (Germano, Kavanagh et al. 2000; Sharir, Germano et al. 2000).

In implementing the method some approximations were employed in the modeling of resolution and noise statistics in the reconstructed image to improve computational efficiency. The position-dependent resolution in SPECT and PET was approximated using a spatially invariant Gaussian kernel, which allows modeling the resolution using convolution, thus greatly reducing computational costs. The voxels values from FBP reconstructions were assumed to follow identical uncorrelated normal distributions, which allowed simplification of the ML-based objective function to a least-squares objective function. For OS-EM reconstruction, the voxels were also assumed to follow uncorrelated normal distributions, but the voxel variances were assumed to be proportional to the voxel means, resulting in a WLS objective function. In addition, the mean image was approximated using the conventional voxel OS-EM reconstructed image.

The proposed model-based method also incorporated a global geometry constraint into the objective function. The constraint encouraged uniform myocardial wall thicknesses and was implemented by adding the variance of thickness model parameters as a penalty term to the LS or WLS objective function. Compared to a previous PVC method based on model-fitting (Dumouchel, Thorn et al. 2012), the introduction of the constraint not only increased the stability of the ill-posed

reconstruction problem, but also effectively improved the robustness to perfusion defects and image noise.

The nonlinear and nonconvex objective function was minimized using two optimization methods. The MultiStart method initialized the optimization with a variety of initial estimates of the parameters, and ultimately selected the set of converged parameters that had the smallest value of the objective function, assuming that one or more points were located in the “basin of attraction” of the global minimum. However, this method was time-consuming and not clinically practical. Therefore, a group-wise alternating optimization method was proposed to improve the computational efficiency by using fewer initial points while maintaining comparable effectiveness in terms of finding the global minimum. This method divided the model parameters into three groups and alternated the optimization of parameters in each group while fixing the parameter values in the other groups. The perturbation study in Chapter 5 revealed that the alternating scheme was not sensitive to initial model parameters except for the initial wall thickness. Consequently, multiple initial thicknesses were used to span the normal variations of myocardium wall thicknesses. We first implemented the method in 2D, both to explore its properties and provide a means of obtaining initial estimates for a fully 3D implementation. In the 2D implementation, the initial values of the parameters were estimated from the short-axis slice for each initial thickness. In the 3D implementation, the initial estimate was synthesized from the results of fitting the reoriented perfusion image slice-by-slice for each initial thickness. The initial estimate resulting in the smallest value of the objective function was regarded as the global optimum and was taken to provide the optimal values of the model parameters for the particular set of observed data.

The proposed method was evaluated using 2D and 3D myocardial perfusion SPECT simulations. The majority of the evaluation studies were performed on the simulated short-axis images for the sake of efficiency. The approximations in resolution and noise modeling were justified by directly examining them as well as by assessing the effects of the approximations on

the estimated model parameters. It was shown that these approximations were more accurate for FBP than for OS-EM. The means of the parameters estimated from multiple noise realizations remained relatively close to their respective true values, but suffered considerable variability, especially for high noise data such as that obtained from gated myocardial SPECT. A simplified 1D model was thus used to gain insight into the properties of the proposed model-fitting method, excluding the effects of the approximated resolution and noise modeling and avoiding the difficulty of finding the global optimum for the full set of 3D parameters. The results of the 1D study implied that the variability was inherent in the fitting of myocardium perfusion images due to the similar size of the myocardial wall thickness and the FWHM of the resolutions of PET and SPECT systems. The results of the 1D study also suggested that modeling of resolution and noise statistics in the reconstructed image would improve the accuracy and precision of the delineation of myocardial boundaries compared to a conventional gradient-based method, which assumed that the maximum magnitude of the image gradient corresponded to the object boundaries.

The proposed model-based method was also evaluated in both 2D and 3D in terms of its suitability for a number of its potential applications. First, the LV segmentation derived from the geometry parameters was compared to that obtained using a thresholding method with an optimized prefilter and an optimized threshold. The model-based method not only eliminated the jagged boundaries and disconnectedness at the perfusion defect obtained with the thresholding method, but also significantly improved the accuracy of the segmentation, with the DSC increasing from 0.77 to 0.90 for data with a clinically realistic noise level. Second, the mid-myocardial surface could also be directly computed from the geometry model parameters. This surface is useful for functional analysis of cardiac motion. Using the proposed method, the mid-myocardial surface was more accurately and precisely estimated than the endocardial and epicardial surfaces. In comparison with three other previously-proposed methods, the model-based method clearly provided more accurate and precise estimates of the mid-myocardial surface. Third, the model-

based method was compared to a deconvolution-based PVC method for the task of estimating the myocardial activity concentrations. The model-based reduced the mean estimation errors relative to the deconvolution method by about 50%; neither of these methods required VOIs defined from anatomical images, in contrast to conventional

The results in this dissertation demonstrated the feasibility and effectiveness of the proposed model-based reconstruction method. While there is still significant future work required to demonstrate clinical applicability, the results here at least in part justify spending the effort needed to move to that stage. The following section discusses some of the future work that is needed to bring this method closer to clinical use.

7.2 Future Work

7.2.1 Evaluation with More Data

In this study, the proposed method was evaluated based on the XCAT phantom, a realistic previously-developed anthropomorphic phantom, and realistic myocardial perfusion SPECT simulations. However, the simulation did not represent the variability in patient anatomy and uptake that is seen in real patient populations. A number of factors absent in the simulated data are likely to affect the performance of the proposed method and should be investigated in future studies.

First, the perfusion defect in the phantom had an extent of approximately 10% and severity of 50%. However, the myocardial blood flow might be significantly reduced in multiple coronary arteries. Consequently, severe perfusion defects spanning the majority of the myocardium are possible. This would result in the low contrast between the myocardium and background or blood pool. The proposed model-based method might encounter problems in this case when very limited structural information is available in the perfusion image. It is important to quantify the sensitivity and robustness of the proposed method to various types of perfusion defects.

Second, the simulated images were from a single anatomy, and thus the method was not tested in the case of anatomical variations (e.g. LV size, wall thickness). It is possible that the proposed parameterization is not general enough to handle the variety of anatomical variations in the myocardium present in real patient populations. This would require adjustments to the model or its parameters. For instance, the sampling scheme of the geometry model may lack the ability to accurately describe the shape of some LV structures, such as the papillary muscle, and the use of a larger number of sampling rays might be required. Also, the range of initial wall thicknesses for the alternating optimization scheme may need to be updated to cover the variations of normal myocardium thicknesses.

Third, the simulated images assumed homogeneous activities in the extra-cardiac regions. In real patients, this is not true in general, and for some patients, even regions close to the heart may have very inhomogeneous activities. For example, some other tissues in close proximity to the LV may have relatively high tracer uptakes in myocardial perfusion images, such as the right ventricle, atrium, liver, intestines, and lungs. Some of organs far enough from the LV could be masked out and ignored before applying the proposed method; however, the influence of organs with high uptake close to the LV cannot be completely eliminated due to partial volume effects (PVEs). This could pose a challenge to the method and require the use of more complicated geometry and activity distribution models that might include other organs, or a combined voxel- and model-based method..

In addition to more comprehensive simulation studies, it is essential that the proposed method ultimately is assessed on patient data to gain insights into its applicability and limitations.

7.2.2 Implementation in the Projection Domain

The model-based reconstruction method in the projection domain was proposed in Chapter 3. In this implementation, the geometry and activity model parameters can be directly obtained from the

acquired projection data. In addition, the modeling of noise statistics is more straightforward and accurate due to that noise in projection bins is uncorrelated. In future investigations, the projection-domain implementation will be compared to the image-domain implementation studied as in previous chapters, which could provide a good initial estimates of the parameters for the projection-domain implementation.

A number of issues are anticipated in the projection-domain implementation. First, for each trial set of the model parameters during the optimization, a time-consuming forward projection is required in order to allow comparison with the measured data. The high computational burden of this forward projection makes the method impractical at present. Second, the projection data are typically acquired for transverse slices of the body. The axis of the body is not aligned with the long axis of the LV. However, the geometry model in the image domain implementation did not parameterize the location and orientation of the LV, which must be taken into account in the projection domain implementation. The location and orientation of the LV can be estimated from, for example, an FBP reconstruction included in and estimated as part of the geometry model. Third, the activity distribution model assumes a homogenous background, but tissues in the extra-cardiac regions may have high tracer uptake. It is not as straightforward to reduce the influence of activity outside the LV in the projection as in the image domain since the projection of the entire 3D image contributes to the projection. One approach is to model activities in these regions using voxel values obtained, for example, from conventional reconstructions. For example, the acquired projection data could first be reconstructed using OS-EM. The image in the volume outside the cardiac VOI could then be delineated in the reconstructed image. The activity in the extra-cardiac volume could then be projected and this projection added to the projection of the VOI during each iteration..

7.2.3 Regularization Term

In this study, the regularization term only imposed constraints on the myocardial wall thicknesses. Prior information about the global LV shape might be incorporated by penalizing the endocardial radius parameters. This could even be done in terms of probability distributions of the endocardial radius and thickness based on clinical data. Alternatively, the LV shape constraints have been used to guide the LV segmentation and could be used in the regularization term. For instance, the endo- and epi-cardial contours in the central long-axis slice could be modeled as two elliptic curves connecting tangentially on the axis at the apex (Nuyts, Suetens et al. 1991). Another method would be to create a reference heart shape based on a set of segmented training images and model shape variability using an affine transformation (Ecabert, Peters et al. 2008).

For gated images where noise levels are high, constraints could be developed to improve the consistency of the myocardial shape between cardiac phases. For example, the values of the corresponding geometry and activity distribution parameters should not have large changes between adjacent gating intervals. In addition, the average wall thickness at end-systole should be larger than that at end-diastole. Also, the total radioactivity in the perfusion image is approximately the same for different gating frames. Such constraints could be expressed mathematically and included in the regularization term, and might be helpful in reducing the variability of the parameter estimates observed with the proposed model-based method in the case of gated imaging.

7.2.4 Process Automation

There are a number of steps in the current method that are done manually. It would be advantageous to automate the entire process from the observed data to the final diagnostic parameters to improve efficiency and reproducibility. Automating some or all of the many steps would be desirable in future implementations both for practical reasons and to reduce bias and variability in the estimates.

The first manual step is identifying and roughly segmenting the LV from the reconstructed image. This rough segmentation serves two purposes: one is to make the data consistent with the assumption that the background activity distribution is homogeneous by removing potentially hot structures such as the liver and intestines; the other is to improve efficiency by restricting image fitting to a smaller VOI. Some methods in the literature might be adapted. Based on prior knowledge about LV location and size, one method iteratively thresholded the image into clusters, determined the cluster corresponding to the myocardium, and then refined the segmentation using dilation (Germano, Kavanagh et al. 1995). Another method first thresholded the myocardial perfusion image and then applied an iterative K-mean clustering algorithm to divide the resulting mask image into the LV region and the extra-cardiac region (Liu, Sinusas et al. 2005).

The second step that is a candidate for automation is to identify the long axis of the LV reorientation of the transaxial images. The reorientation in Chapter 6 was accomplished using a manual method using software developed in our lab. The user was required to specify the range of the LV and manually draw the axis from different views. This is tedious and subject to operator variability. In the future, the LV reorientation will be included in the geometry model and obtained during model fitting. A fully automatic reorientation method has been developed by fitting the extracted maximal-count myocardial surface to a quadratic surface and then determining the long-axis (Germano, Kavanagh et al. 1995). Such a method could be used to provide an initial estimate of these reorientation parameters.

The third step is to determine the axial LV extent, i.e., the valve plane and position of the apex. The upper and lower bounds of the LV along the axis play a significant role in the proposed method because the parameterization of the geometry and activity distribution models depends on them. It is challenging to automatically estimate the locations of the apex and valve plane, especially when perfusion defects are present in these regions. One previously-proposed method estimated the valve plane as the first slice basal to the mid-ventricular slice that contained no pixels

greater than a threshold equal to a percentage of the maximum value within the VOI, and similarly estimated the first apex slice (Faber, Cooke et al. 1999). However, it is not clear whether the threshold percentage is applicable to all images and patients. More robust and accurate methods would likely be needed.

BIBLIOGRAPHY

- Abidov, A., G. Germano, et al. (2013). "Gated SPECT in assessment of regional and global left ventricular function: an update." Journal of Nuclear Cardiology **20**(6): 1118-1143.
- Aston, J. A., V. J. Cunningham, et al. (2002). "Positron Emission Tomography Partial Volume Correction: Estimation and Algorithms." Journal of Cerebral Blood Flow & Metabolism **22**(8): 1019-1034.
- Barrett, H. H., D. W. Wilson, et al. (1994). "Noise properties of the EM algorithm: I. Theory." Physics in medicine and biology **39**(5): 833-846.
- Bateman, T. M., G. V. Heller, et al. (2006). "Diagnostic accuracy of rest/stress ECG-gated Rb-82 myocardial perfusion PET: comparison with ECG-gated Tc-99m sestamibi SPECT." Journal of Nuclear Cardiology **13**(1): 24-33.
- Berman, D. S., H. Kiat, et al. (1991). "Technetium 99m Sestamibi in the Assessment of Chronic Coronary-Artery Disease." Seminars in Nuclear Medicine **21**(3): 190-212.
- Boeing, G., P. H. Pretorius, et al. (2006). "Study of relative quantification of Tc-99 m with partial volume effect and spillover correction for SPECT oncology imaging." IEEE transactions on nuclear science **53**(3): 1205-1212.
- Byrd, R. H., J. C. Gilbert, et al. (2000). "A trust region method based on interior point techniques for nonlinear programming." Mathematical Programming **89**(1): 149-185.
- Cauvin, J. C., J. Y. Boire, et al. (1993). "3D modeling in myocardial 201 TL SPECT." Computerized medical imaging and graphics **17**(4): 345-350.
- Cerqueira, M. D., N. J. Weissman, et al. (2002). "Standardized myocardial segmentation and nomenclature for tomographic imaging of the heart - A statement for healthcare professionals from the Cardiac Imaging Committee of the Council on Clinical Cardiology of the American Heart Association." Circulation **105**(4): 539-542.
- Cooke, C. D., E. V. Garcia, et al. (1994). "Determining the accuracy of calculating systolic wall thickening using a fast Fourier transform approximation: a simulation study based on canine and patient data." Journal of nuclear medicine : official publication, Society of Nuclear Medicine **35**(7): 1185-1192.
- DePasquale, E. E., A. C. Nody, et al. (1988). "Quantitative rotational thallium-201 tomography for identifying and localizing coronary artery disease." Circulation **77**(2): 316-327.
- Di Carli, M. F. and R. Hachamovitch (2006). "Should PET replace SPECT for evaluating CAD? The end of the beginning." Journal of Nuclear Cardiology **13**(1): 2-7.
- Dilsizian, V. and J. Narula (2013). Atlas of nuclear cardiology, Springer Science & Business Media.
- Du, Y., I. Madar, et al. (2013). "Compensation for spill-in and spill-out partial volume effects in cardiac PET imaging." Journal of Nuclear Cardiology **20**(1): 84-98.
- Dumouchel, T. and R. A. deKemp (2011). "Analytical-Based Partial Volume Recovery in Mouse Heart Imaging." IEEE Transactions on Nuclear Science **58**(1): 110-120.
- Dumouchel, T., S. Thorn, et al. (2012). "A three-dimensional model-based partial volume correction strategy for gated cardiac mouse PET imaging." Physics in medicine and biology **57**(13): 4309-4334.
- Ecabert, O., J. Peters, et al. (2008). "Automatic model-based segmentation of the heart in CT images." Ieee Transactions on Medical Imaging **27**(9): 1189-1201.
- Erlandsson, K., I. Buvat, et al. (2012). "A review of partial volume correction techniques for emission tomography and their applications in neurology, cardiology and oncology." Physics in Medicine and Biology **57**(21): R119-R159.
- Everaert, H., P. R. Franken, et al. (1996). "Left ventricular ejection fraction from gated SPET myocardial perfusion studies: a method based on the radial distribution of count rate

- density across the myocardial wall." European Journal of Nuclear Medicine **23**(12): 1628-1633.
- Faber, T. L., M. S. Akers, et al. (1991). "Three-dimensional motion and perfusion quantification in gated single-photon emission computed tomograms." Journal of nuclear medicine : official publication, Society of Nuclear Medicine **32**(12): 2311-2317.
- Faber, T. L., C. D. Cooke, et al. (1999). "Left ventricular function and perfusion from gated SPECT perfusion images: an integrated method." Journal of Nuclear Medicine **40**(4): 650-659.
- Faber, T. L., E. M. Stokely, et al. (1991). "A model-based four-dimensional left ventricular surface detector." Medical Imaging, IEEE Transactions on **10**(3): 321-329.
- Ficaro, E. P., B. C. Lee, et al. (2007). "Corridor4DM: the Michigan method for quantitative nuclear cardiology." Journal of Nuclear Cardiology **14**(4): 455-465.
- Freiberg, J., J. D. Hove, et al. (2004). "Absolute quantitation of left ventricular wall and cavity parameters using ECG-gated PET." Journal of Nuclear Cardiology **11**(1): 38-46.
- Frey, E., Z.-W. Ju, et al. (1993). "A fast projector-backprojector pair modeling the asymmetric, spatially varying scatter response function for scatter compensation in SPECT imaging." IEEE transactions on nuclear science **40**(4): 1192-1197.
- Frey, E. and B. Tsui (2006). Collimator-detector response compensation in SPECT. Quantitative analysis in nuclear medicine imaging, Springer: 141-166.
- Galt, J. R., V. Garcia, et al. (1990). "Effects of myocardial wall thickness on SPECT quantification." Medical Imaging, IEEE Transactions on **9**(2): 144-150.
- Gambhir, S. (1990). Quantitation of the physical factors affecting the tracer kinetic modeling of cardiac positron emission tomography data, UCLA.
- Garcia, E. V., T. L. Faber, et al. (2007). "The increasing role of quantification in clinical nuclear cardiology: the Emory approach." Journal of Nuclear Cardiology **14**(4): 420-432.
- Geman, S. and D. Geman (1984). "Stochastic relaxation, Gibbs distributions, and the Bayesian restoration of images." Pattern Analysis and Machine Intelligence, IEEE Transactions on(6): 721-741.
- Germano, G., J. Erel, et al. (1997). "Automatic quantitation of regional myocardial wall motion and thickening from gated technetium-99m sestamibi myocardial perfusion single-photon emission computed tomography." Journal of the American College of Cardiology **30**(5): 1360-1367.
- Germano, G., P. B. Kavanagh, et al. (2007). "Quantitation in gated perfusion SPECT imaging: the Cedars-Sinai approach." Journal of Nuclear Cardiology **14**(4): 433-454.
- Germano, G., P. B. Kavanagh, et al. (1995). "Automatic reorientation of three-dimensional, transaxial myocardial perfusion SPECT images." Journal of Nuclear Medicine **36**(6): 1107-1114.
- Germano, G., P. B. Kavanagh, et al. (2000). "A new algorithm for the quantitation of myocardial perfusion SPECT. I: technical principles and reproducibility." Journal of nuclear medicine : official publication, Society of Nuclear Medicine **41**(4): 712-719.
- Germano, G., H. Kiat, et al. (1995). "Automatic quantification of ejection fraction from gated myocardial perfusion SPECT." Journal of nuclear medicine : official publication, Society of Nuclear Medicine **36**(11): 2138-2147.
- Germano, G., H. Kiat, et al. (1995). "Automatic Quantification of Ejection Fraction from Gated Myocardial Perfusion Spect." Journal of Nuclear Medicine **36**(11): 2138-2147.
- Goris, M., C. Thompson, et al. (1994). "Modelling the integration of myocardial regional perfusion and function." Nuclear Medicine Communications **15**(1): 9-20.
- Hadamard, J. (2003). Lectures on Cauchy's Problem in Linear Partial Differential Equations, Courier Corporation.
- Hajjiri, M. M., M. B. Leavitt, et al. (2009). "Comparison of positron emission tomography measurement of adenosine-stimulated absolute myocardial blood flow versus relative

- myocardial tracer content for physiological assessment of coronary artery stenosis severity and location." JACC: Cardiovascular Imaging **2**(6): 751-758.
- Hansen, C. L., R. A. Goldstein, et al. (2006). "Myocardial perfusion and function single photon emission computed tomography." Journal of nuclear cardiology : official publication of the American Society of Nuclear Cardiology **13**(6): e97-120.
- Hoffman, E. J., S.-C. Huang, et al. (1979). "Quantitation in positron emission computed tomography: 1. Effect of object size." Journal of computer assisted tomography **3**(3): 299-308.
- Hudson, H. M. and R. S. Larkin (1994). "Accelerated image reconstruction using ordered subsets of projection data." IEEE transactions on medical imaging **13**(4): 601-609.
- Hutton, B. F., I. Buvat, et al. (2011). "Review and current status of SPECT scatter correction." Physics in medicine and biology **56**(14): R85.
- Jaszczak, R. J., R. E. Coleman, et al. (1981). "Physical factors affecting quantitative measurements using camera-based single photon emission computed tomography (SPECT)." IEEE Transactions on Nuclear Science **28**(1): 69-80.
- Khorsand, A., S. Graf, et al. (2003). "Model-based analysis of electrocardiography-gated cardiac 18F-FDG PET images to assess left ventricular geometry and contractile function." Journal of Nuclear Medicine **44**(11): 1741-1746.
- Lalush, D. S. and M. N. Wernick (2004). "Iterative image reconstruction." Emission tomography: the fundamentals of PET and SPECT: 443-472.
- Lipke, C. S., H. P. Kuhl, et al. (2004). "Validation of 4D-MSPECT and QGS for quantification of left ventricular volumes and ejection fraction from gated 99mTc-MIBI SPET: comparison with cardiac magnetic resonance imaging." European Journal of Nuclear Medicine and Molecular Imaging **31**(4): 482-490.
- Liu, Y.-H. (2007). "Quantification of nuclear cardiac images: The Yale approach." Journal of Nuclear Cardiology **14**(4): 483-491.
- Liu, Y.-H., A. J. Sinusas, et al. (2005). "New hybrid count-and geometry-based method for quantification of left ventricular volumes and ejection fraction from ECG-gated SPECT: methodology and validation." Journal of Nuclear Cardiology **12**(1): 55-65.
- Lum, D. P. and M. N. Coel (2003). "Comparison of automatic quantification software for the measurement of ventricular volume and ejection fraction in gated myocardial perfusion SPECT." Nuclear Medicine Communications **24**(3): 259-266.
- Mannting, F. and M. Morgan-Mannting (1993). "Gated SPECT with technetium-99m-sestamibi for assessment of myocardial perfusion abnormalities." Journal of nuclear medicine: official publication, Society of Nuclear Medicine **34**(4): 601-608.
- Marwick, T., R. Go, et al. (1991). "Myocardial perfusion imaging with positron emission tomography and single photon emission computed tomography: frequency and causes of disparate results." European heart journal **12**(10): 1064-1069.
- Mc Ardle, B. A., T. F. Dowsley, et al. (2012). "Does rubidium-82 PET have superior accuracy to SPECT perfusion imaging for the diagnosis of obstructive coronary disease?: A systematic review and meta-analysis." Journal of the American College of Cardiology **60**(18): 1828-1837.
- Montalescot, G., U. Sechtem, et al. (2013). "2013 ESC guidelines on the management of stable coronary artery disease." European heart journal **34**(38): 2949-3003.
- Nuyts, H., A. Maes, et al. (1996). "Three-dimensional correction for spillover and recovery of myocardial PET images." Journal of nuclear medicine : official publication, Society of Nuclear Medicine **37**(5): 767-774.
- Nuyts, J., P. Suetens, et al. (1991). "Delineation of ECT images using global constraints and dynamic programming." Medical Imaging, IEEE Transactions on **10**(4): 489-498.
- Papoulis, A. and S. U. Pillai (2002). Probability, random variables, and stochastic processes, Tata McGraw-Hill Education.

- Parkash, R., T. Ruddy, et al. (2004). "Potential utility of rubidium 82 PET quantification in patients with 3-vessel coronary artery disease." Journal of Nuclear Cardiology **11**(4): 440-449.
- Patel, M. R., E. D. Peterson, et al. (2010). "Low diagnostic yield of elective coronary angiography." New England Journal of Medicine **362**(10): 886-895.
- Paul, A. K. and H. A. Nabi (2004). "Gated myocardial perfusion SPECT: basic principles, technical aspects, and clinical applications." J Nucl Med Technol **32**(4): 179-187; quiz 188-179.
- Porenta, G., W. Kuhle, et al. (1995). "Parameter estimation of cardiac geometry by ECG-gated PET imaging: validation using magnetic resonance imaging and echocardiography." Journal of nuclear medicine : official publication, Society of Nuclear Medicine **36**(6): 1123-1129.
- Pretorius, P. H. and M. A. King (2009). "Diminishing the impact of the partial volume effect in cardiac SPECT perfusion imaging." Medical physics **36**(1): 105-115.
- Puetter, R., T. Gosnell, et al. (2005). "Digital image reconstruction: Deblurring and denoising." Astronomy and Astrophysics **43**(1): 139.
- Quarantelli, M., K. Berkouk, et al. (2004). "Integrated software for the analysis of brain PET/SPECT studies with partial-volume-effect correction." Journal of Nuclear Medicine **45**(2): 192-201.
- Rahmim, A. and H. Zaidi (2008). "PET versus SPECT: strengths, limitations and challenges." Nuclear Medicine Communications **29**(3): 193-207.
- Reader, A. J., P. J. Julyan, et al. (2003). "EM algorithm system modeling by image-space techniques for PET reconstruction." IEEE Transactions on Nuclear Science **50**(5): 1392-1397.
- Rousset, O., A. Rahmim, et al. (2007). "Partial volume correction strategies in PET." PET clinics **2**(2): 235-249.
- Rousset, O. G., Y. Ma, et al. (1998). "Correction for partial volume effects in PET: principle and validation." The Journal of Nuclear Medicine **39**(5): 904.
- Rudin, L. I., S. Osher, et al. (1992). "Nonlinear total variation based noise removal algorithms." Physica D: Nonlinear Phenomena **60**(1): 259-268.
- Schaefer, W. M., C. S. Lipke, et al. (2005). "Quantification of left ventricular volumes and ejection fraction from gated 99mTc-MIBI SPECT: MRI validation and comparison of the Emory Cardiac Tool Box with QGS and 4D-MSPECT." Journal of nuclear medicine : official publication, Society of Nuclear Medicine **46**(8): 1256-1263.
- Sharir, T., G. Germano, et al. (2000). "A new algorithm for the quantitation of myocardial perfusion SPECT. II: validation and diagnostic yield." Journal of nuclear medicine : official publication, Society of Nuclear Medicine **41**(4): 720-727.
- Soneson, H., J. F. A. Ubachs, et al. (2009). "An Improved Method for Automatic Segmentation of the Left Ventricle in Myocardial Perfusion SPECT." Journal of Nuclear Medicine **50**(2): 205-213.
- Soret, M., S. L. Bacharach, et al. (2007). "Partial-volume effect in PET tumor imaging." Journal of nuclear medicine : official publication, Society of Nuclear Medicine **48**(6): 932-945.
- Teo, B.-K., Y. Seo, et al. (2007). "Partial-volume correction in PET: validation of an iterative postreconstruction method with phantom and patient data." Journal of Nuclear Medicine **48**(5): 802-810.
- Tohka, J. and A. Reilhac (2008). "Deconvolution-based partial volume correction in Raclopride-PET and Monte Carlo comparison to MR-based method." Neuroimage **39**(4): 1570-1584.
- Tsui, B., E. Frey, et al. (1994). "The importance and implementation of accurate 3D compensation methods for quantitative SPECT." Physics in medicine and biology **39**(3): 509.
- Wells, R. G. (2016). "Instrumentation in molecular imaging." Journal of Nuclear Cardiology: 1-5.

- Williams, K. A. (2005). "A historical perspective on measurement of ventricular function with scintigraphic techniques: Part II-Ventricular function with gated techniques for blood pool and perfusion imaging." Journal of Nuclear Cardiology **12**(2): 208-215.
- Wilson, D. W. (1994). "Noise and Resolution Properties of FB and ML-EM Reconstructed SPECT Images."
- Wilson, D. W., B. M. Tsui, et al. (1994). "Noise properties of the EM algorithm: II. Monte Carlo simulations." Physics in medicine and biology **39**(5): 847-871.
- Wilson, D. W. and B. M. W. Tsui (1993). "Noise Properties of Filtered-Backprojection and ML-EM Reconstructed Emission Tomographic-Images." Ieee Transactions on Nuclear Science **40**(4): 1198-1203.
- Withey, D. J. and Z. J. Koles (2007). "Medical image segmentation: Methods and software." 2007 Joint Meeting of the 6th International Symposium on Noninvasive Functional Source Imaging of the Brain and Heart and the International Conference on Functional Biomedical Imaging: 143-146.
- Wu, C. J. (1983). "On the convergence properties of the EM algorithm." The Annals of statistics: 95-103.
- Yoshida, H. (1989). "Effect of Spatial Resolution on SPECT Quantification Values." Journal of Nuclear Medicine **30**: 508-514.
- Yoshinaga, K., C. Katoh, et al. (2011). "Incremental diagnostic value of regional myocardial blood flow quantification over relative perfusion imaging with generator-produced rubidium-82 PET." Circulation Journal **75**(11): 2628-2634.
- Zaidi, H. and K. F. Koral (2004). "Scatter modelling and compensation in emission tomography." European Journal of Nuclear Medicine and Molecular Imaging **31**(5): 761-782.
- Zaidi, H., T. Ruest, et al. (2006). "Comparative assessment of statistical brain MR image segmentation algorithms and their impact on partial volume correction in PET." NeuroImage **32**(4): 1591-1607.
- Zou, K. H., S. K. Warfield, et al. (2004). "Statistical validation of image segmentation quality based on a spatial overlap index - Scientific reports." Academic Radiology **11**(2): 178-189.

CURRICULUM VITAE

Yinfeng Dong was born on October 20, 1988 in Yancheng, Jiangsu Province, People's Republic of China. He received his Bachelor of Science in Electronic Engineering and Information Science from University of Science and Technology of China at Hefei, Anhui, People's Republic of China in 2011. He has been a Ph.D. student in the Department of Electrical and Computer Engineering at The Johns Hopkins University since August 2011. He has also been a graduate research assistant in the Division of Medical Image Physics, Department of Radiology and Radiological Science, School of Medicine at the Johns Hopkins University. He received his Master of Science in Electrical and Computer Engineering from The Johns Hopkins University in 2014. His research interest includes myocardial perfusion SPECT and PET, image reconstruction, image segmentation and registration.